Review Article

Mohamed Ibrahim Ahmed Abdel Maksoud*, Mohamed Mohamady Ghobashy, Ahmad S. Kodous, Ramy Amer Fahim, Ahmed I. Osman*, Ala'a H. Al-Muhtaseb, David W. Rooney, Mohamed A. Mamdouh, Norhan Nady*, and Ahmed H. Ashour

Insights on magnetic spinel ferrites for targeted drug delivery and hyperthermia applications

https://doi.org/10.1515/ntrev-2022-0027
received October 26, 2021; accepted December 6, 2021

Abstract: Magnetic spinel ferrite nanoparticles (SFNPs) attract high scientific attention from researchers due to their broad area for biomedicine applications, comprising cancer magnetic hyperthermia and targeted drug delivery. Uniquely, its excellent performance, namely, tuning size and surface morphology, excellent magnetism, extraordinary magnetically heat induction, promising biocompatibility, and specific targeting capacity, is essential for their effective utilization in clinical diagnosis and therapeutics of diseases. This review emphasizes the anticancer properties of nanoparticles of spinel ferrites with extra focus on the most recent literature. A critical review is provided on the latest applications of SFNPs in cancer therapy. Based on the results obtained from this review, SFNPs have the indefinite ability in cancer therapy through two mechanisms: (1) hyperthermia, where SFNPs, used as a hyperthermia mediator, elevated the tumor cells heat post-exposure to an external magnetic field and radiosensitizer during cancer radiotherapy; and (2) targeted drug delivery of cytotoxic drugs in tumor treatment. SFNPs induced apoptosis and cell death of cancer cells and prevented cancer cell proliferation.

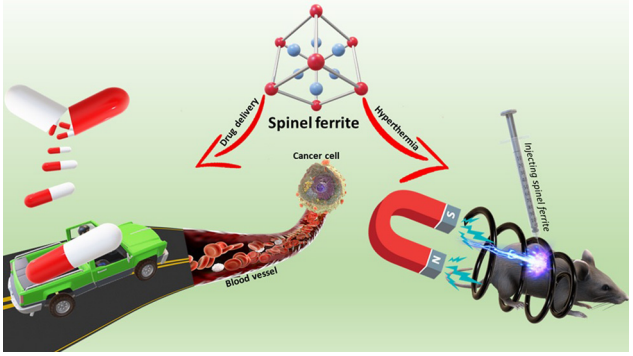

Graphical abstract

Keywords: magnetic properties, anticancer, hyperthermia, targeted drug delivery, biomedical applications

* **Corresponding author: Mohamed Ibrahim Ahmed Abdel Maksoud,** Radiation Physics Department, Materials Science Lab., National Center for Radiation Research and Technology (NCRRT), Egyptian Atomic Energy Authority (EAEA), Cairo, Egypt, e-mail: muhamadmqsod@gmail.com
* **Corresponding author: Ahmed I. Osman,** School of Chemistry and Chemical Engineering, Queen's University Belfast, David Keir Building, Stranmillis Road, Belfast, BT9 5AG, Northern Ireland, e-mail: aosmanahmed01@qub.ac.uk
* **Corresponding author: Norhan Nady,** Polymeric Materials Research Department, City of Scientific Research and Technological Applications (SRTA-City), Borg El-Arab City, Alexandria 21934, Egypt, e-mail: norhan.nady77@yahoo.com
Mohamed Mohamady Ghobashy: Radiation Research of Polymer Department, Nanotechnology Laboratory, National Center for Radiation Research and Technology (NCRRT), Egyptian Atomic Energy Authority (EAEA), Cairo, Egypt
Ahmad S. Kodous: Radiation Biology Department, National Centre for Radiation Research and Technology (NCRRT), Egyptian Atomic Energy Authority (EAEA), Cairo, Egypt
Ramy Amer Fahim: Radiation Protection and Dosimetry Department, National Center for Radiation Research and Technology (NCRRT), Egyptian Atomic Energy Authority, (EAEA), Cairo, Egypt
Ala'a H. Al-Muhtaseb: Department of Petroleum and Chemical Engineering, College of Engineering, Sultan Qaboos University, Muscat, Oman
David W. Rooney: School of Chemistry and Chemical Engineering, Queen's University Belfast, David Keir Building, Stranmillis Road, Belfast, BT9 5AG, Northern Ireland
Mohamed A. Mamdouh: Department of Pharmaceutics and Industrial Pharmacy, Faculty of Pharmacy, October 6 University, 6th of October City, Giza, 12585, Egypt
Ahmed H. Ashour: Radiation Physics Department, Materials Science Laboratory, National Center for Radiation Research and Technology (NCRRT), Egyptian Atomic Energy Authority (EAEA), Cairo, Egypt

Abbreviations

CPT	camptothecin drug
DNA	deoxyribonucleic acid
DOX	doxorubicin
FESEM	field emission scanning electron microscope
MRI	magnetic resonance imaging
MTT	(3-(4,5-dimethylthiazol-2-yl)-2,5-diphenyltetrazolium bromide) tetrazolium assay

MWCNT	multi-walled carbon nanotubes
NPs	nanoparticles
RNA	ribonucleic acid
SEM	scanning electron microscope
SAR	specific absorption rate
SF	spinel ferrite
SPM	superparamagnetic
SPMNP	superparamagnetic nanoparticle
TEM	transmission electron microscope
TUNEL	terminal deoxynucleotidyl transferase biotin-dUTP nick end labeling

1 Introduction

Cancer is considered one of the most frightening diseases that globally kill millions of people [1]. The universal encumbrance of cancer *via* the GLOBOCAN 2018 assessments for the cancer incidence and mortality has been given *via* the International Agency for Research on Cancer, including a geographic variability in 20 world regions (Figure 1) [2]. It was reported that 18.1 million new cancer cases and the cancer mortality were 9.6 million in 2018. These cases are projected to increase to about 24 million by 2035 [3]. Many of the investigations on drug delivery procedures have been carried out in cancer treatment. This investigation has focused on overcoming the principal holdback on cancer treatment *via* chemotherapy, or, in other words, the damage of healthy (normal) tissue *via* therapeutic use. To limit the outcome of this issue (the death of the case or the dismissal of the cancerous tumor), delivery procedures that are of a specific size possessing a suit distribution of anticancer agents and a mechanism to make the therapeutic agents release (that causes the agents to assemble at the tumor sites) should be advanced [4,5]. The utilization of nanoparticles (NPs) has grown from the normal function of drug delivery to multifunctional purposes [6]. These merits are diverse such as labeling transports the drug and gene, pathogens and proteins revelation, probes of ribonucleic acid (RNA) and deoxyribonucleic acid (DNA), optical imaging reinforce, design of tissues, biomolecules, and segregation of cells and as a chemotherapeutic agent [3]. Between various types of functional NPs, magnetic spinel ferrite nanoparticles (SFNPs) have a significant focus for their possible utilization such as an opposite to agent enhancer in magnetic resonance imaging (MRI) and an energetic agent in drug delivery [7,8]. SFNPs have several essential biomedical applications [9]. They are used in hyperthermia in cancer therapy, radiosensitizer, drug delivery and release [10–13], enhancing MRI contrast [14–16], and for biomagnetic separation purposes [17]. NPs are of small size, <100 nm, in a minimum of one dimension. As the size diameter decreased to ≤20 nm, the paramagnetic characteristics were lost by SFNPs. In contrast, they were changed to superparamagnetic (SPM) when subjected to an externally applied magnetic field due to thermal effects [18]. The biomedical applications of SFNPs were highly dependent on the synthesis method, shape, size, and types. It is revealed that the ratio of the surface area to volume of NPs was increased as the particle size decreased [19]. Herein, this critical review conducts and evaluates the latest knowledge and exhaustive information about the anticancer activity, hyperthermia, and drug delivery of SFNPs.

Ferrites can be categorized into three categories, *viz*., spinel, garnet, and hexa-ferrites, depending upon their crystal structures. In this review, we will focus on spinel ferrite (SF) materials. SFs are marked *via* the nominal formula RFe_2O_4, where R represents the divalent cations with an ionic radius ranging from 0.6 to 1 Å; such as copper, magnesium, cobalt, nickel, zinc, *etc*. elements. The ferric ions (Fe^{3+}) can be substituted with different trivalent cations or rare earth elements. The spinel structure is inferred from the mineral magnesium aluminate ($MgAl_2O_4$), which possesses a cubic structure and every cubic cell comprises eight units, as exhibited in Figure 2 [21]. This crystal structure was initially settled *via* Bragg and *via* Nishikawa [22].

Magnetic ferrite NPs have been reported as biomedically significant agents, especially drug delivery vehicles, MRI, and hyperthermia mediators. SFs are favored over other materials due to their broader range of applications, low cost, high sensitivity, where high sensing is required, and selectivity for certain gases. Ferrites find uses in many applications in the areas such as sensors [23], transformer cores [24], chip inductor [25], electromagnetic wave absorber [26], data storage [27], heavy metals removal [28], antibacterial and antibiofilm agents [29], and water remediation [30,31]. Also, ferrites have received huge attention because of their extensive applications, such as power applications [32]. Many continuous efforts are made to control the size, shape, magnetic, and morphological properties of ferrites by different types of synthesis methods.

2 Synthesis methods of SF NPs

The synthesis techniques and conditions exercised through the synthesis route are the prime agents that manage and verify the feature nature for SF NPs [33]. Nanostructured ferrites can be fabricated *via* several synthesis procedures such as sol–gel [30,34–39], co-precipitation [40–44], hydrothermal [45–47], thermal decomposition [48–50], Polyol

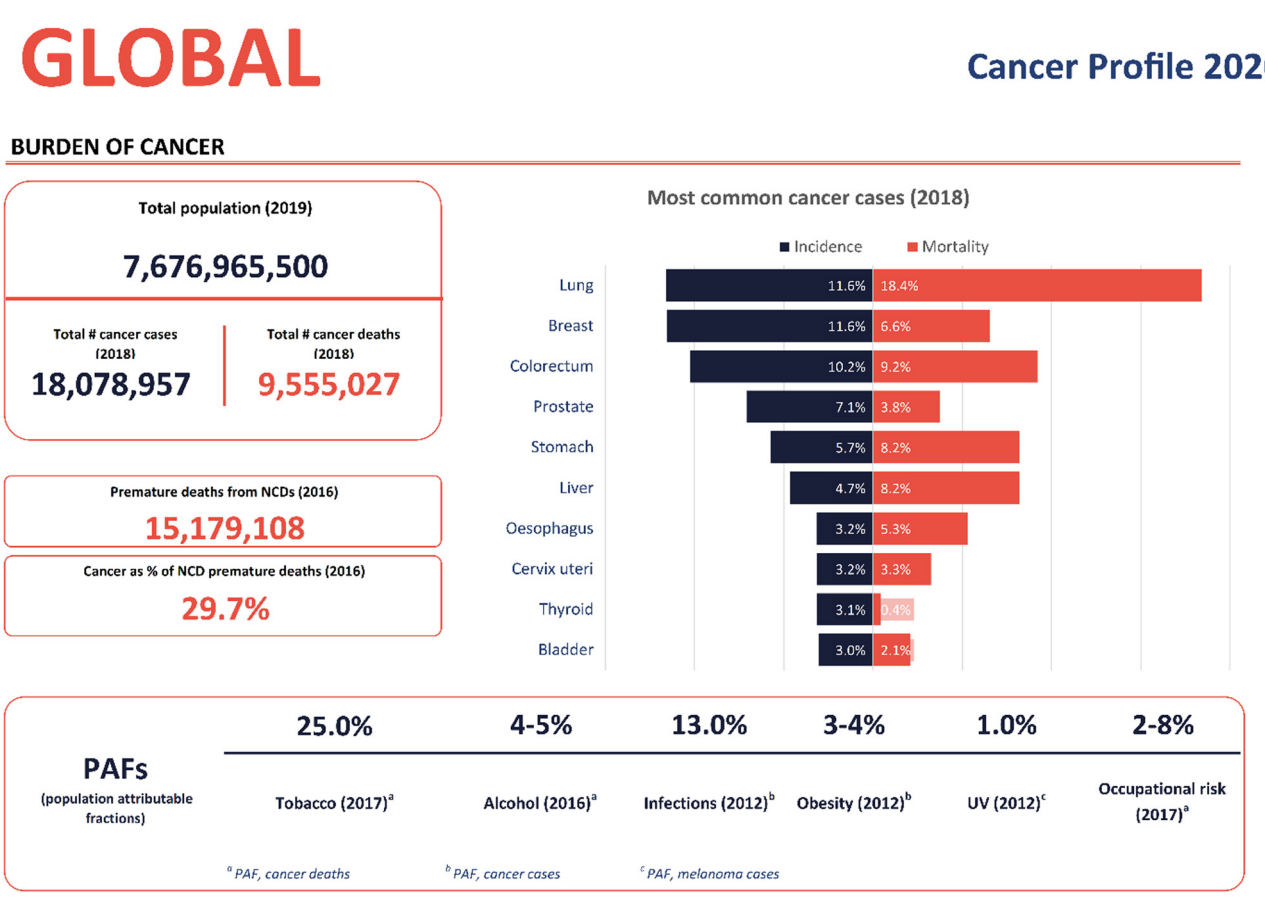

Figure 1: Global cancer statistics of prevalence and death worldwide [2,20].

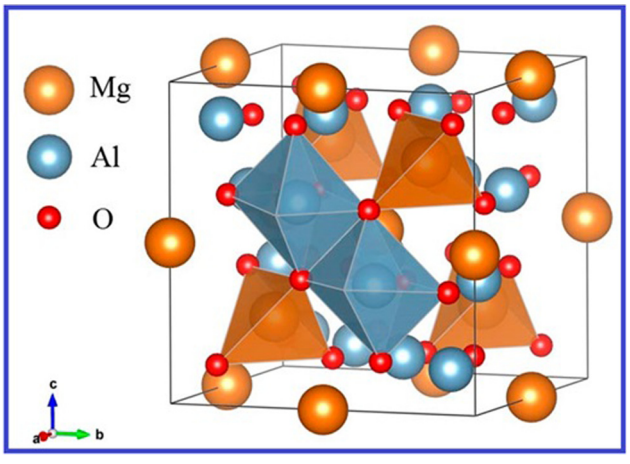

Figure 2: Crystallographic representation of magnesium aluminate ($MgAl_2O_4$). Adapted from ref. [21] with permission from Elsevier™.

[51,52], solvothermal [53–55], spray pyrolysis deposition technique [56] and sonochemical techniques [57,58] (see Table 1). The magnetic properties are marked with interdependence on the surface morphology of magnetic NPs and the fabrication processes. These procedures provide excellent control of the crystal's size, size diffusion, and lattice deficiencies [45].

2.1 Sol–gel method

Metal alkoxide solutions are used as preliminary precursors in the sol–gel fabrication technique, which undergo hydrolysis and condensation polymerization followed by the gel formation stage [59,60]. Besides, more heat strategies are required to exclude any volatile in the obtained gel to get the final crystalline phase [34,61]. The sol–gel technique has some merits such as cost-effectiveness and does not require particular tools; additionally, it can be performed at a moderate temperature. Furthermore, in the sol–gel method, the temperature of the reaction ranges from room temperature up to 199.85°C. This state is suitable to manufacture SF NPs with fine size distribution and manageable form and shape [34,61]. Besides the simplicity in terms of the fabrication methods of SFNPs, these merits make the sol–gel technique so unique [30,34,36–39]. Furthermore, it is one of the adopted

Table 1: Synthesis methods of SFs SFNPs

Synthesis methods	SF	Ref.
Sol–gel	$Co_{0.5}Mg_{0.25}Cd_{0.25}Fe_{2-x}Ce_xO_4$	[59]
	$Co_{0.8-x}Mn_{0.2}Zn_xFe_2O_4$	[60]
	$CoFe_2O_4$	[61]
	$NiGd_xFe_{2-x}O_4$	[62]
	$Ni_{0.8}Zn_{0.2}Ce_xFe_{2-x}O_4$	[63]
	$Mn_{0.85}Zn_{0.15}Ni_xFe_2O_4$	[64]
Co-precipitation	$NiGd_xFe_{2-x}O_4$	[65]
	$Ni_{0.5}Mg_xZn_{0.5-x}Fe_2O_4$	[66]
	$Mn_xZn_{1-x}Fe_2O_4$	[67]
	$Zr_xMg_{0.2-x}Co_{0.8-x}Fe_2O_4$	[68]
	$Co_xSn_{1-x}Fe_2O_4$	[69]
	$ZnFe_2O_4$	[70]
Hydrothermal	$MnFe_2O_4$	[71]
	MFe_2O_4 (M = Co, Ni)	[72]
	$(Mg,Ni)(Fe,Al)_2O_4$	[73]
	$CuFe_2O_4$	[74]
	$Mn_{0.8}Zn_{0.2}Fe_2O_4$	[75]
Thermal decomposition	$CoFe_2O_4$	[76]
	$MnFe_2O_4$	[77]
	$NiFe_2O_4$	[78]
	$MnFe_2O_4$	[79]
Polyol	$CoFe_2O_4$	[80]
	$Sr_{0.3}Mg_{0.7}Fe_2O_4$	[10]
	MFe_2O_4 (M = Mn, Fe, Co, Ni)	[81]
	$CoFe_2O_4$	[82]
	$La_{0.7}Ca_{0.3-x}Ba_xMnO_3$	[83]
Solvothermal	$CoFe_2O_4$	[84]
	$Mn_{0.8}Zn_{0.2}Fe_2O_4$	[85]
	$ZnFe_2O_4$	[86]
	MFe_2O_4, M = Fe, Co, Ni, Mn, Cu, Zn	[87]
	$CoFe_2O_4$	[88]
Spray pyrolysis	$Li_{0.5-x/2}Mg_xFe_{2.5-x/2}O_4$	[89]
	$Ni_{1-x}Cd_xFe_2O_4$	[90]
	$Cu_{0.1}Ni_{0.3}Zn_{0.6}Fe_2O_4$	[91]
	$Ni_{1-x}Cu_xFe_2O_4$	[92]
	$NiFe_{2-x}Al_xO_4$	[93]
Sonochemical	$Zn_{1-x}Co_{0.5x}Mg_{0.5x}Fe_2O_4$	[94]
	$Ni_{0.4}Cu_{0.2}Zn_{0.4}Fe_{2-x}Eu_xO_4$	[95]
	$Co_{0.3}Ni_{0.5}Mn_{0.2}Eu_xFe_{2-x}O_4$	[58]
	$CoFe_{2-x}Gd_xO_4$	[96]
	$Mn_{1-x}Cu_xFe_{1.85}La_{0.15}O_4$	[97]

fabrication techniques to manage structure, morphology structure, pureness, and form of SFNPs *via* altering several factors, such as the sol concentration, the rate of stirring, and cancellation temperature [61–64].

Abdel Maksoud *et al.* [30] have used the sol–gel method to synthesize $Mn_{0.5}Zn_{0.5-x}Mg_xFe_2O_4$ NPs, which were synthesized in the presence of citric acid ($C_6H_8O_7$) solution that was added as a fuel and ethylene glycol ($C_2H_6O_2$) drop by drop to produce the final gel composition. The resulting $Mn_{0.5}Zn_{0.5-x}Mg_xFe_2O_4$ solution was dried at 120°C and then the obtained powders were sintered (899.85°) at 1,173 K, as illustrated in Figure 3. They used $Mn_{0.5}Zn_{0.5-x}Mg_xFe_2O_4$ NPs as a magnetic recyclable catalyst for outstanding photocatalytic and antimicrobial potentials.

2.2 Co-precipitation

Co-precipitation is among the commonly proficient procedures utilized to fabricate NPs with uniform distribution [65–68]. In this process related to SFNPs, aqueous solutions comprise the mix up of divalent transition cations and ferric (v/v = 1/2) [69,70]. The synthesis technique demands accurate calibration and checks of pH to obtain SFNPs with excellent features. The pH of the solution is generally maintained *using* NH_4OH solution or NaOH solution [43,71,72]. Then, an energetic stirring of the solution will be used with or without the drying process. Numerous research investigations, which used the co-precipitation approach to fabricate the NPs, have been performed [40–44]. Recently, Gul *et al.* [73] have reported the fabrication of $Al_xZnFe_{2-x}O_4$, NPs *via* the co-precipitation technique, where the solutions of the starting chemicals were dissolved in deionized water and stirred at a stoichiometric ratio. The pH of all the solutions was kept at pH = 10 *via* the dropwise addition of the NH_4OH solution. Then, the solution's color changed from orange to deep brown with coffee-colored precipitates at the ground of the beaker. The precipitates after being dried are crushed and annealed at 600°C for 8 h, as exhibited in Figure 4. The analysis of magnetic properties assumed that the prepared NPs possess excellent magnetic characteristics. Also, the optical investigations of the NPs showed that these SFs additionally possess photocatalytic applications. The photocatalytic degradation of methylene blue *via* spinel samples has been discussed. The ferrite particles could be separated from contaminated water easily through a magnetic field. Hence, ferrite NPs can be utilized and recycled easily for photocatalytic applications.

2.3 Hydrothermal reactions

The hydrothermal technique uses an aqueous solution as a reaction system in a particular closed reaction vessel to produce a high-temperature, high-pressure reaction *via* heating the reaction system and pressurizing it [47,74]. In this technique, water serves as a reactant that produces a reaction hydrolysis speedup with improved solubility of related materials in the precursor. This procedure gives

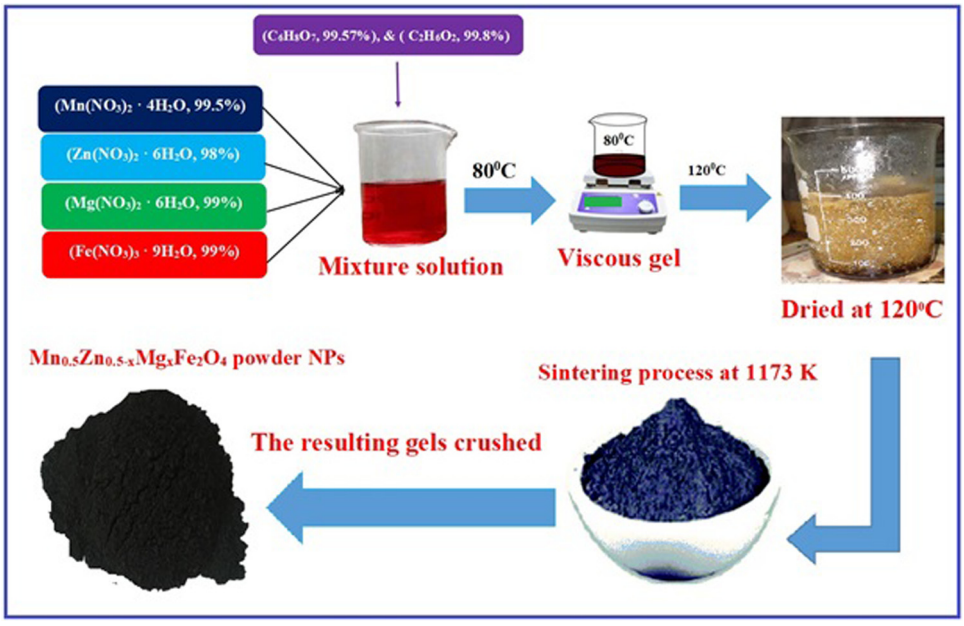

Figure 3: Schematic diagram of the sol–gel method for the synthesis of $Mn_{0.5}Zn_{0.5-x}Mg_xFe_2O_4$ NPs. Adapted with permission from ref. [30], Copyright, 2020, Elsevier.

more significant mobility due to the lower viscosity of water and further leads to an enhancement in the crystal structure, and accelerated the ability of the NP product [47]. The hydrothermal technique is one of the popular suitable fabrication techniques for the large-scale generation of SFs. The SF synthesized has excellent features with restricted size, and excellent size distribution can be gained by choosing the proper mix of solvents and changing parameters such as temperature, pressure, and reaction time [45]. Ding *et al.* [75] have synthesized cobalt ferrite through an ethanol-assisted hydrothermal technique. The scanning electron microscopic (SEM) images

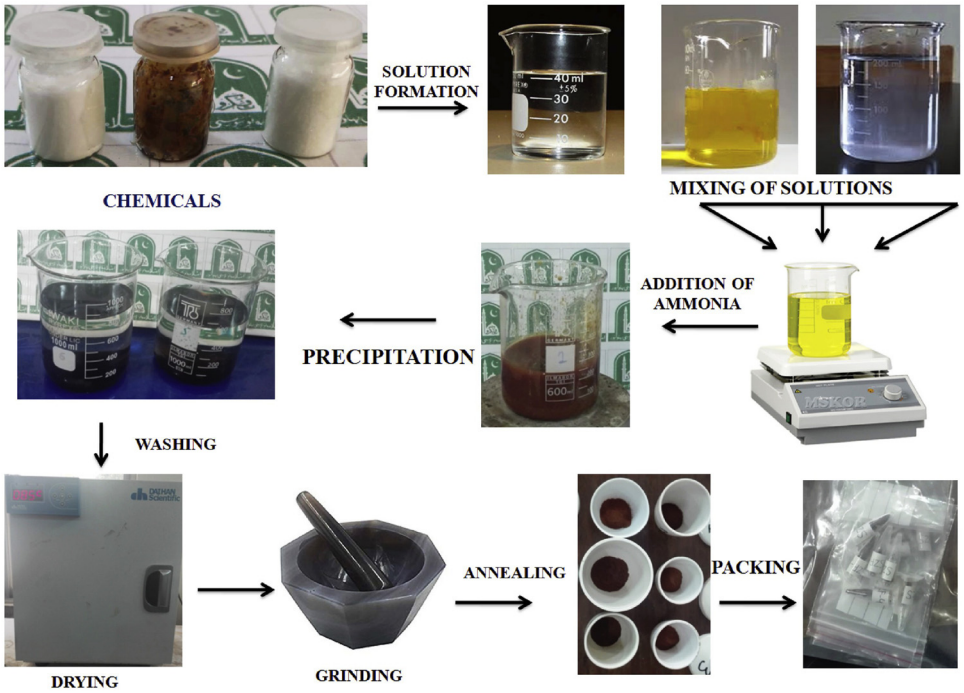

Figure 4: Schematic illustration of the co-precipitation method of $Al_xZnFe_{2-x}O_4$ NPs. Adapted from ref. [73] with permission from Elsevier™.

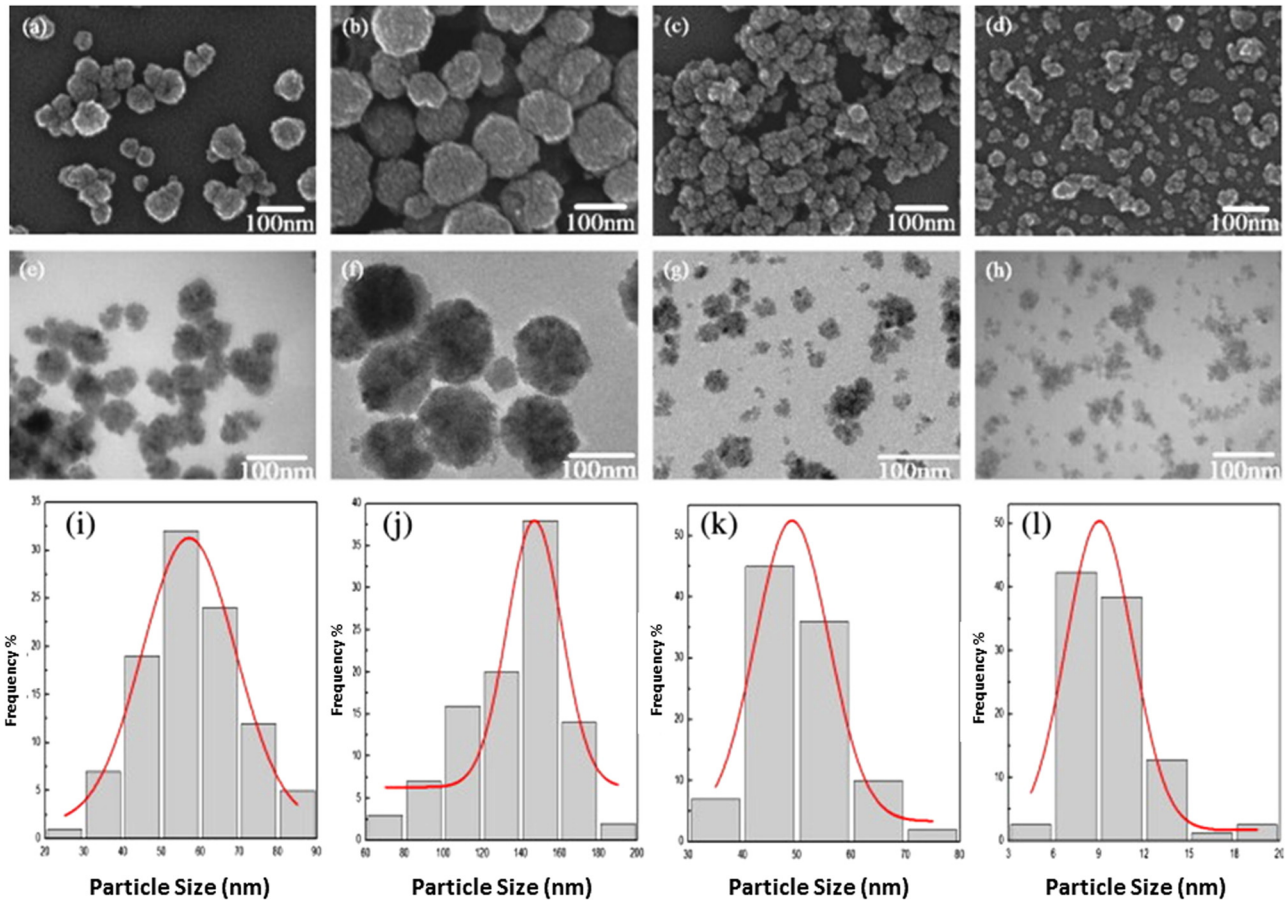

Figure 5: SEM and TEM images and the corresponding particle size distribution obtained from SEM images of samples 1, 2, 3, and 4 represented as (a, e, i), (b, f, j), (c, g, k) and (d, h, l), respectively. Adapted from ref. [75] with permission from Elsevier™.

revealed that the samples possessed a narrow size distribution (Figure 5). The water/ethanol volume ratio was chosen as 0, 5/2, 3/4, and 1/6, and the samples were labeled as sample1, sample2, sample3, and sample4, respectively. A constant increase of the ethanol ratio will appear in the particle extension restraint, and the decrease of particle size is ascribed to the surface passivation effect. It was approved *via* SEM and transmission electron microscopic (TEM) images of sample3 and sample4, where a speedy reduction in the particle size and crash of agglomerates can be established. It is worth remarking that, with increasing ethanol content in the ethanol–water mixed solution, apparent SPM performance of NPs was seen. The adsorption capability of ferrite NPs for Congo Red (CR) was tested. Improvement of adsorption capability for CR was shown by combining ethanol. Also, the adsorption mechanism was discussed. This examination shows that the composition of ethanol/water mixed solution possesses excellent impacts on the microstructure and magnetic properties and adsorption capacity of the CR dye of $CoFe_2O_4$ samples.

2.4 Thermal decomposition

The thermal decomposition approach is among the most simplistic routes for fabricating SFs, including the thermal decomposition of organometallic sources, *viz.*, metal acetylacetonate complexes of carbonyls. Besides, there are suitable solvents for organic and surfactants for the fabrication of SFs [61]. The size and form of SFs have been restrained *via* altering the temperature, the rate of heat, or the metal source concentration, and it is feasible to achieve SFs having extremely mono dispersion, consistent morphology, and close particle size distribution. Yang *et al.* [76] have synthesized a nonstoichiometric zinc ferrite ($Zn_xFe_{3-x}dO_4$) NPs with Zn substituent content x = 0–0.5 by the thermal decomposition route *via* utilizing oleic acid as a surfactant. Alterations in the morphology of the as-synthesized samples could be examined from the SEM images. When the content of the zinc source is about 0.004 mol or smaller, octahedral particles are produced. By increasing the content of the zinc source to 0.006 and 0.008 mol, well-faceted polyhedral crystallites are formed. Meanwhile,

using 0.01 mol of zinc source leads to nonuniform particles with huge cubes and some smaller ones. oleic acid acts as both a reducing agent and stabilizer in the fabrication method and the source of the zinc/surfactant ratio is essential for the morphology. Besides, an increase of the zinc precursor will give rise to insufficiency in the surfactant, which it is then challenging to stabilize all nuclei to a uniform shape. This reason for the samples appears unestablished and nonuniform. Size-dependent utilization (radar absorption and hyperthermia) was observed more. Both applications required magnetic NPs with magnetization with extraordinary saturation. In hyperthermia, Zn ferrite NPs (26 nm) coated *via* the P-mPEG polymer revealed higher biocompatibility and heating efficiency, indicating the possible use in *in vivo* cancer therapy.

Also, Sharifi *et al.* [77] have studied the effect of the quantity of solvent on the formation of Fe-substituted $ZnFe_2O_4$ NPs through thermal decomposition. $Fe_{0.6}Zn_{0.4}Fe_2O_4$ NPs have been synthesized *via* a thermal decomposition technique by utilizing metal acetylacetonate in a high-temperature boiling point solvent and oleic acid. Figure 6 displays FESEM images of the magnetic NPs. As can be noticed, the sample has approximately homogeneous spherical particles besides possessing narrow size distribution. The particle size was reduced from 39 to 14 nm.

2.5 The polyol method

The polyol approach has been lately considered more in the fabrication of SFs. In this process, diethylene glycol acts as both the solvent and reducing agent, *viz.*, $CoFe_2O_4$ [78], $Co_{0.50}Zn_{0.50}Fe_2O_4$ [79], *etc.*, were recently published. Gaudisson *et al.* [80] have fabricated a group of nanostructured and compact spinel $CoFe_2O_4$ *via* the polyol method by utilizing three different solvents of polyol category, *viz.*, diethylenglycol, 1,2-dihydroxyethane, and 1,2-propanediol, including different aggregate phases. The obtained $CoFe_2O_4$ particles display distinct aggregate states. On utilizing diethylenglycol as a solvent, the $CoFe_2O_4$ particles exhibited uniform size (5 nm), were completely nonaggregated, and were in nearly isotropic form (Figure 7a). In the case of utilizing 1,2-propanediol (Figure 7d) and 1,2-ethanediol (Figure 7g) as solvents, the Co-ferrite comprises 10 and 100 nm clusters, respectively. They exhibit well-marked fringes belonging to the crystallographic planes of Co's spinel lattice, as indicated by the indexation from the corresponding Fourier transform images. Obvious irreversibility is systematically obtained between the zero-field cooling (ZFC) and field-cooling (FC) susceptibility. The ZFC plots exhibit a distinct peak at a critical temperature defined as the blocking temperature, T_B, and decrease quickly to zero when the temperature drops below T_B, while FC slightly increases. T_B displays the threshold temperature above which the magnetic anisotropy barrier was solely defeated through the thermal activation energy, causing NPs to relax from the ferrimagnetic state to the SPM state. These drifts in ZFC and FC were characteristic of superparamagnetism in single magnetic domains.

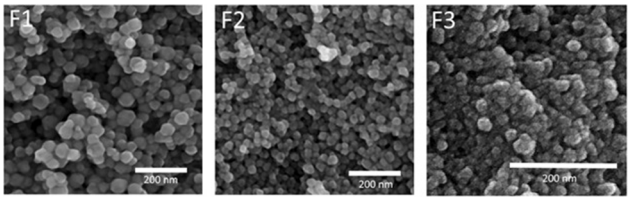

Figure 6: FESEM micrograph of Fe-substituted $ZnFe_2O_4$ NPs with different sizes and three batches including 10 mL (F1), 20 mL (F2,) and 30 mL (F3) of benzyl ether. Adapted from ref. [77] with permission from Elsevier™.

2.6 Solvothermal

In the solvothermal fabrication approach, aqueous or nonaqueous solvents can be utilized to fabricate NPs with accurate restrictions covering the size distribution, form, and phases of the crystals. These physical features have been adjusted *via* altering specific test factors, *viz.*, the reaction temperature, contact time, type of the solvent, type of used surfactant, and purity of precursors. Numerous SFs and their related composites have been fabricated by utilizing the solvothermal fabrication approach [10,61]. Aparna *et al.* [81] have synthesized different SFs with nominal composition MFe_2O_4 (M = Fe, Co, Ni, Mn, Cu, Zn) *via* the solvothermal method using ethylene glycol as a solvent and polyethylene glycol (PEG) 600 as a co-solvent. The prepared SFs exhibit approximately spherical morphology. The average particle sizes of Fe_3O_4 (36.1 nm), $CoFe_2O_4$ (51.3 nm), $NiFe_2O_4$ (41.9 nm), $MnFe_2O_4$ (37.6 nm), $CuFe_2O_4$ (135.1 nm), and $ZnFe_2O_4$ (81.1 nm) are illustrated in Figure 8. The cluster configuration had larger particles produced *via* the accumulation of tinier particles. The results showed that the change in the solvent during the synthesis generates particles with varying morphologies, and supercapacitive performances were observed. The specific capacitances of Fe_3O_4, $CoFe_2O_4$, $NiFe_2O_4$, $MnFe_2O_4$, $CuFe_2O_4$, and $ZnFe_2O_4$ were estimated to be 101, 444.8, 109.26, 190, 250, and 138.95 F/g, respectively. The highest specific capacitance is observed for $CoFe_2O_4$ as compared to

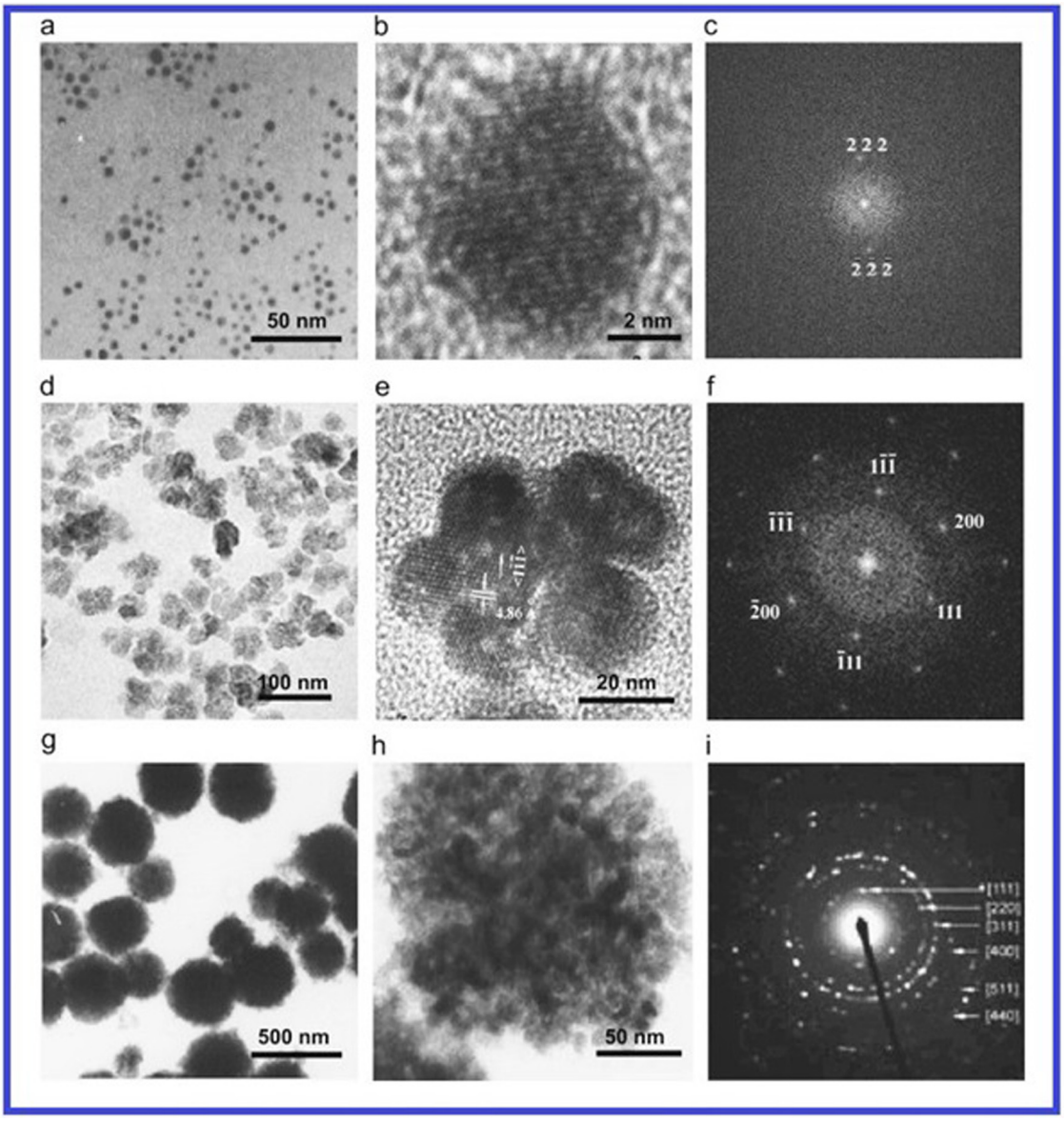

Figure 7: TEM images of Co-ferrite obtained with separate polyols: diethylenglycol, 1,2 propanediol, and 1,2 ethanediol (as (a and b), (d and e) and (g and h)). Fourier transform images are presented in every condition ((c), (f), and (i)). Adapted from ref. [80] with permission from Elsevier™.

other metal ferrites. The capacitive behavior of $CoFe_2O_4$ was also found to vary with morphology.

2.7 Sonochemical technique

Through ultrasonic radiation, bubbles are generated in the solvent medium and can efficiently compile the diffuse energy of ultrasound; upon breakdown, extraordinary heating energy was discharged to the bubble's heating treatment [82,83]. This produces a vacating localized hot spot with sufficient temperature inside the bubbles of around 5×10^3 K and 10^3 bar, respectively. These dominant conditions give rise to various chemical reactions, which are almost always not attainable [84]. Recently, Almessiere *et al.* [85] have investigated the effect of substitution of terbium ions on the microstructure, dielectric, and microwave properties of Ni–Cu–Zn ferrite synthesized *via* the sonochemical technique. The terbium-doped Ni–Cu–$ZnFe_2O_4$ possesses an average particle size of 21 nm. The distribution is close, which suggests a tight particle size ranging between 5 and 40 nm. The sample with the Tb content (x = 0.06) is in contrast to other samples in the appearance of bimodal size distribution performance, which is seen in Figure 9a–f. The average

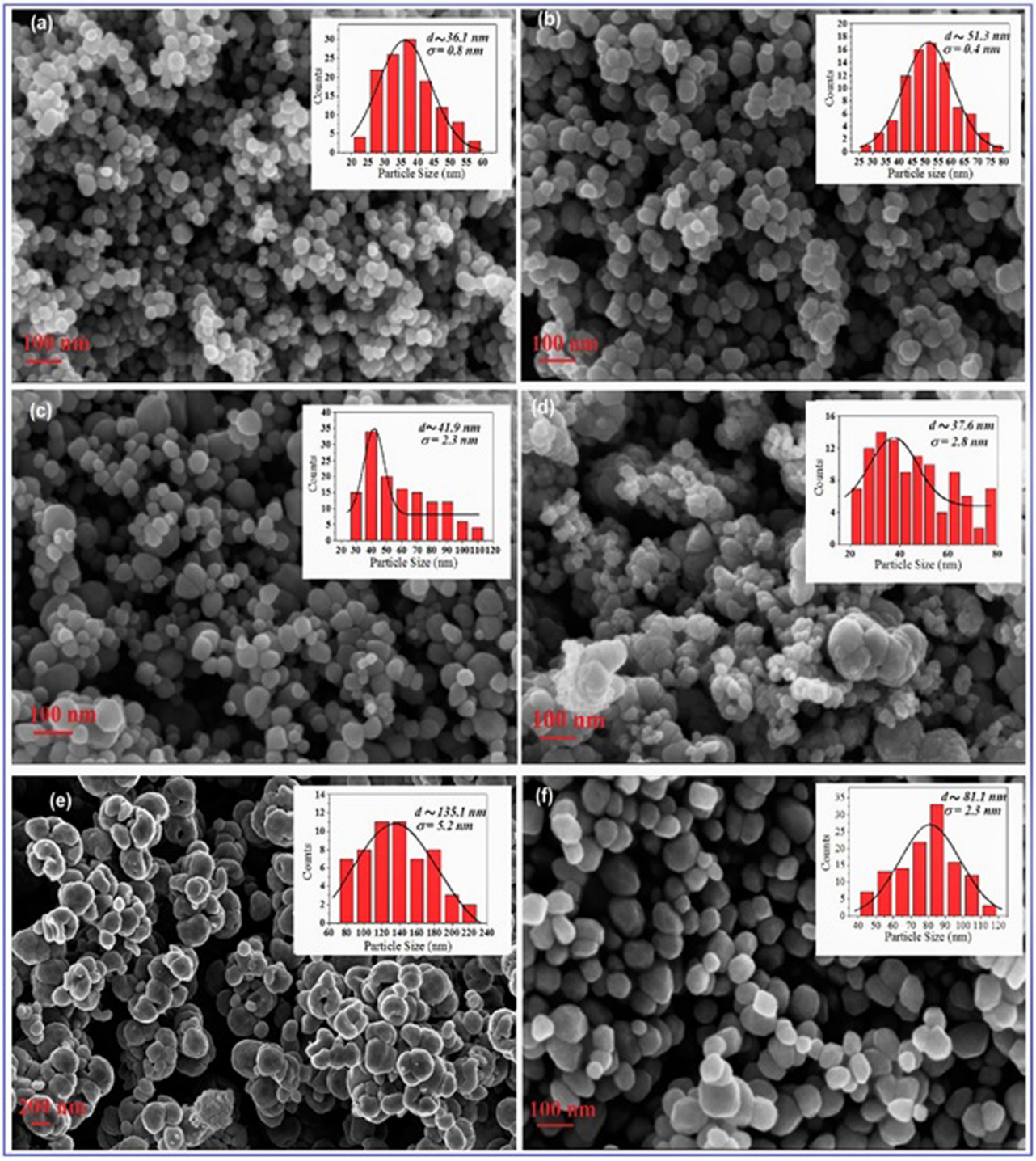

Figure 8: FESEM images of (a) magnetite, (b) $CoFe_2O_4$, (c) $NiFe_2O_4$, (d) $MnFe_2O_4$, (e) $CuFe_2O_4$, and (f) $ZnFe_2O_4$. Adapted from ref. [81] with permission from Elsevier™.

particle size of the $Ni_{0.4}Cu_{0.2}Zn_{0.4}Fe_{1.94}Tb_{0.06}O_4$ sample reached 57 nm. The substitution ratio revealed a substantial impact on the dielectric characteristics, while the Tb ion replacement had a small but distinguished effect on the AC/DC conductivity variation. The reflection losses as a function of frequency dependences were calculated from *S*-parameter data in the range of 1–4.5 GHz. The electromagnetic absorption in the frequency interval of 1.85–3.79 GHz was observed. The nonlinear performance of the amplitude-frequency characteristics was

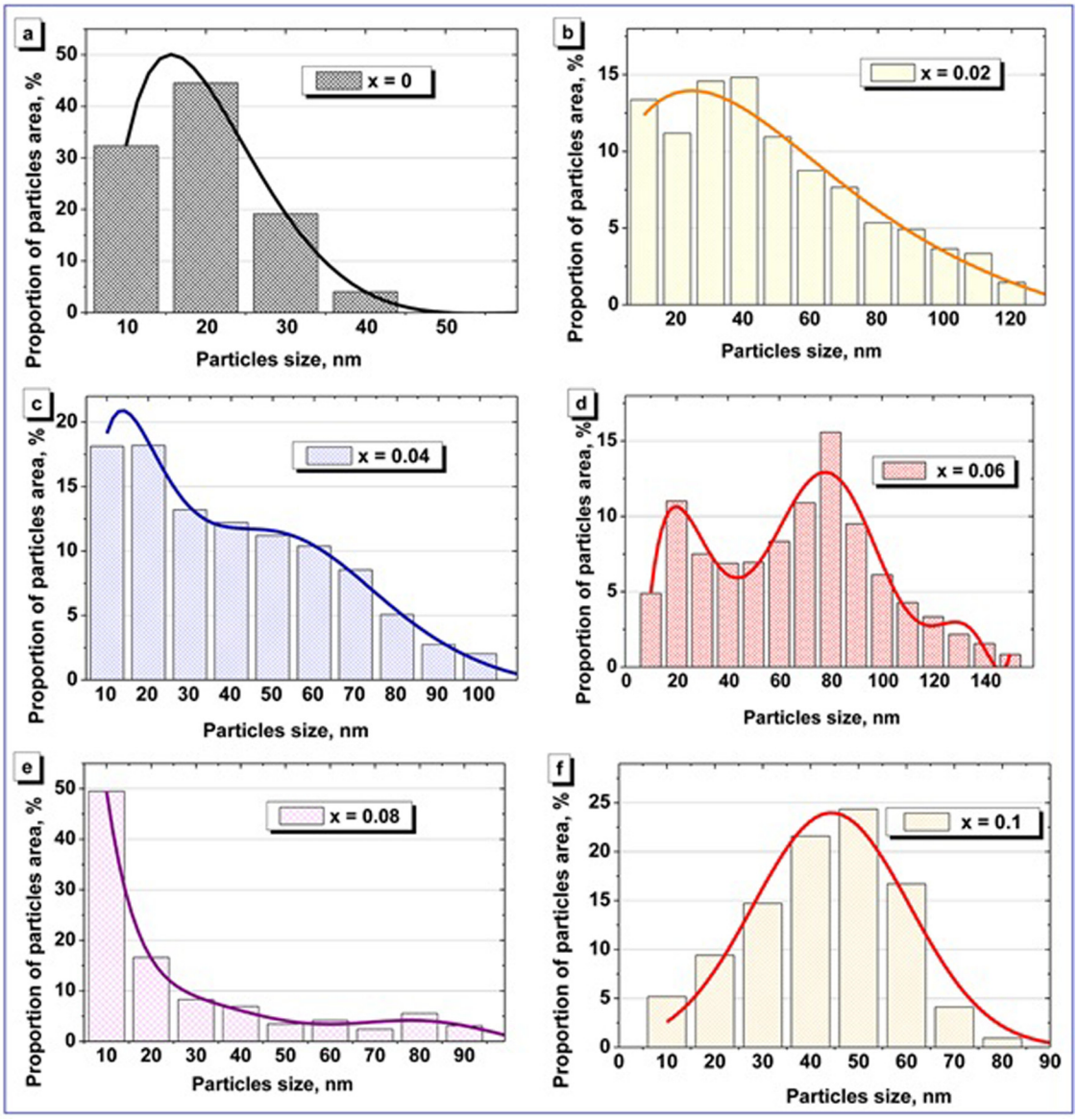

Figure 9: Particle size distribution of the Tb-doped Ni–Cu–Zn/Fe_2O_4 ($x \leq 0.1$). Adapted from ref. [85] with permission from Elsevier™.

changed with Tb ions. It was observed that the microstructural parameters correlate well with the principal absorption characteristics. The decrease of the reflected electromagnetic radiation was explained along with domain-boundary resonance, which well correlates with the microstructure data. The low-dimensional magnetic oxides possessing the domain-boundary resonance have a role in the nature of absorption.

2.8 Synthesis of ferrite thin films

The significant problems the researchers face are fabricating ferrite films utilizing easy technology with low-temperature heat treatment and low vacuum. The ferrite films have been fabricated earlier using various methods, *viz*., RF sputtering, plasma laser deposition, *etc*. These methods regularly include elaborate and costly apparatus and complicated processes. Besides, the high deposition temperature limits the option of the substrate material as well as restricts various applications of ferrite thin films [56]. It should be remarked that agglomeration could be solved utilizing the synthesis techniques in which the formation and separation of particles occur. These techniques involve spray pyrolysis techniques in which liquid solutions of reagents were sprayed, and the drops of the solution were supplied to a heated reactor or flame. Heat treatment causes the evaporation of the solvent and the formation of a solid phase in the structure of

nanocrystalline particles in the absence of aggregation [86]. Pratibha Rao *et al.* have deposited (Co, Cu, Ni, Zn) ferrite thin films onto the Si (100) and alumina substrates *via* the spray pyrolysis deposition technique. SEM images of $CoFe_2O_4$ and $ZnFe_2O_4$ thin films deposited on Si (100) show spherical morphology. The Ni-ferrite thin film reveals a petal-like structure while $CuFe_2O_4$ has a cubic morphology with spherical particles inserted in it (Figure 10) [56].

3 Structure and properties of SFs

3.1 Structure of SFs

The SF MFe_2O_4 possesses a cubic unit cell and comprises eight cubic cells involving 56 ions. These ions were distributed as follows: 32 oxygen (O^{2-}) anions, 8 M^{2+} cations, and 16 ferric cations. The oxygen ions possess a large radius and settled an almost packed face-centered cubic structure amidst more petite metal cations filling the subsites states belonging to space group *Fd3m* [87]. As two separate valence cations are possible, two classes of crystallographic sites are in the spinel structure, namely, A sites enclosed *via* four oxygen ions (tetrahedral) and B sites circled by six oxygen ions (octahedral) [88,89]. Maksoud *et al.* [90] have investigated the influence of zinc ion substitution on cobalt ferrite NPs prepared using a sol–gel technique. The Rietveld refinements at room temperature for XRD patterns of $Co_{1-x}Zn_xFe_2O_4$ NPs are illustrated in Figure 11. The detected reflection peaks correspond to the characteristic *Fd3m* space group SFs (JCPDS card no. 74-2082) [91,92]. All detected peaks are allowed Bragg 2θ positions according to the space group *Fd3m* and are noticeable as vertical lines. The obtained data revealed successful synthesis of the cubic structure $Co_{1-x}Zn_xFe_2O_4$ without any secondary phases [93,94].

Generally, there are two vibrational bands characteristic for SFs, namely υ_1 and υ_2 originating from the stretching vibration of A-site groups (tetrahedral) and B-site groups (octahedral), respectively [95]. Massoudi *et al.* [96] have prepared $Ni_{0.6}Zn_{0.4}Fe_{1.5}Al_{0.5}O_4$ *via* the sol–gel technique following the annealing process at different temperatures. The Fourier transform infrared spectroscopy spectrum of $Ni_{0.6}Zn_{0.4}Fe_{1.5}Al_{0.5}O_4$ was acquired at room temperature in the range from 400 to 4,000 cm^{-1}. According to Waldron, the prominent peaks at 557–581 cm^{-1} and 403–410 cm^{-1} are ascribed to the cation-anion bond stretching vibration in A and B sites, respectively (Figure 12a–b). Consequently, the appearance of these two bands υ_1 and υ_2 confirmed the formation of the $Ni_{0.6}Zn_{0.4}Fe_{1.5}Al_{0.5}O_4$ SF structure.

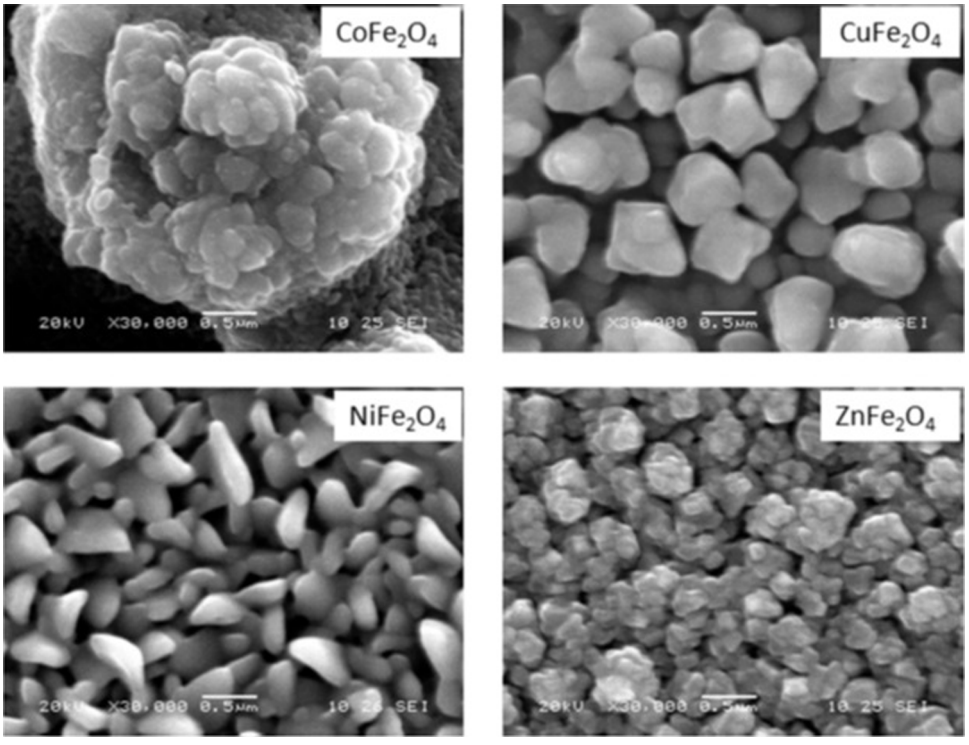

Figure 10: SEM images of spray deposited and air-annealed (Co, Cu, Ni, Zn) ferrite thin films. Adapted from ref. [56].

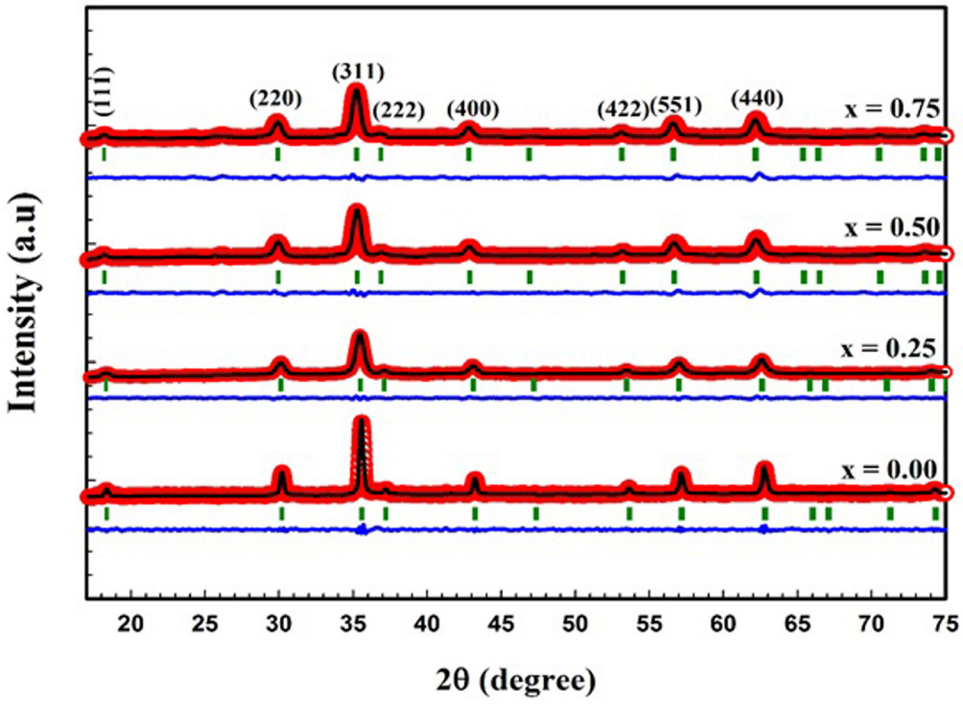

Figure 11: Rietveld refined XRD patterns of $Co_{1-x}Zn_xFe_2O_4$ representing the Zn content (x). Adapted from ref. [90] with permission from Elsevier™.

Mössbauer spectroscopy is exceptionally sensitive to tiny alterations in electron density at Fe's nucleus, ascribed to diverse electronic and structural situations. Isomer shift occurs due to the electrostatic interaction within the distribution of nuclear charge and S-electron density, leading to shifting the levels of nuclear energy. The isomer shift relies on the overall nuclear charge and the nuclear radius. Besides, it depends on the densities of the S-electron for both absorber and source. The isomer shift has been utilized to estimate the valence state of iron atoms. The isomer shift values are in the range of 0.1–0.5 mm/s for ferric ions and exceed 0.5 mm/s in the case of ferrous ions [97]. Poudel *et al.* [98] have studied the Mössbauer spectra of gadolinium-substituted nickel ferrite $NiGd_xFe_{2-x}O_4$. The absorption results from Fe^{3+} (A Site) adapted a single hyperfine pattern. Hence, the substitution of the Fe^{3+} ion with a Gd^{3+} at the B site was not a considerable sufficient change in the whole superexchange interaction to initiate a remarkable diversity in the hyperfine field at the A site. Besides, every iron ion at the B site possessed only six A-site nearest neighbors. Therefore, for each change in the Fe^{3+} ion at the tetrahedral site *via* a significant ratio, an altering in the superexchange interaction is observed (Figure 13).

Also, the energy-dispersive X-ray spectroscopy mapping and scanning electron microscopy (SEM) are conducted to affirm the homogeneous distribution of spinel and their elemental mapping photographs. As presented in Figure 14, the homogeneous distribution and elemental mapping photographs of Zn, Cu, and Mn substituted $CoFe_2O_4$ are introduced [35].

3.2 Magnetic properties of SFNPs

Magnetic NPs have exceptional magnetic and structural features in these materials and hence have wide utilization in many applications like MRI, high-density magnetic recording media, magnetically guided drug delivery, and hyperthermia [9]. Moreover, when an SF with magnetic features is exposed to a magnetic field, its magnetization (M) progresses immediately, as shown in Figure 15 [99]. As the magnetic field (H) magnitude improves, the magnetization approaches its highest value, denoted saturation magnetization (M_s). When the magnetic field is canceled, the magnetization variations exhibit distinctive performance, in which low magnetization has remained in the SF, denoted residual magnetization (M_r). By reducing the magnetic field intensity to negative states, the affected magnetization in SF continuously declines until the field intensity approaches a negative value. The

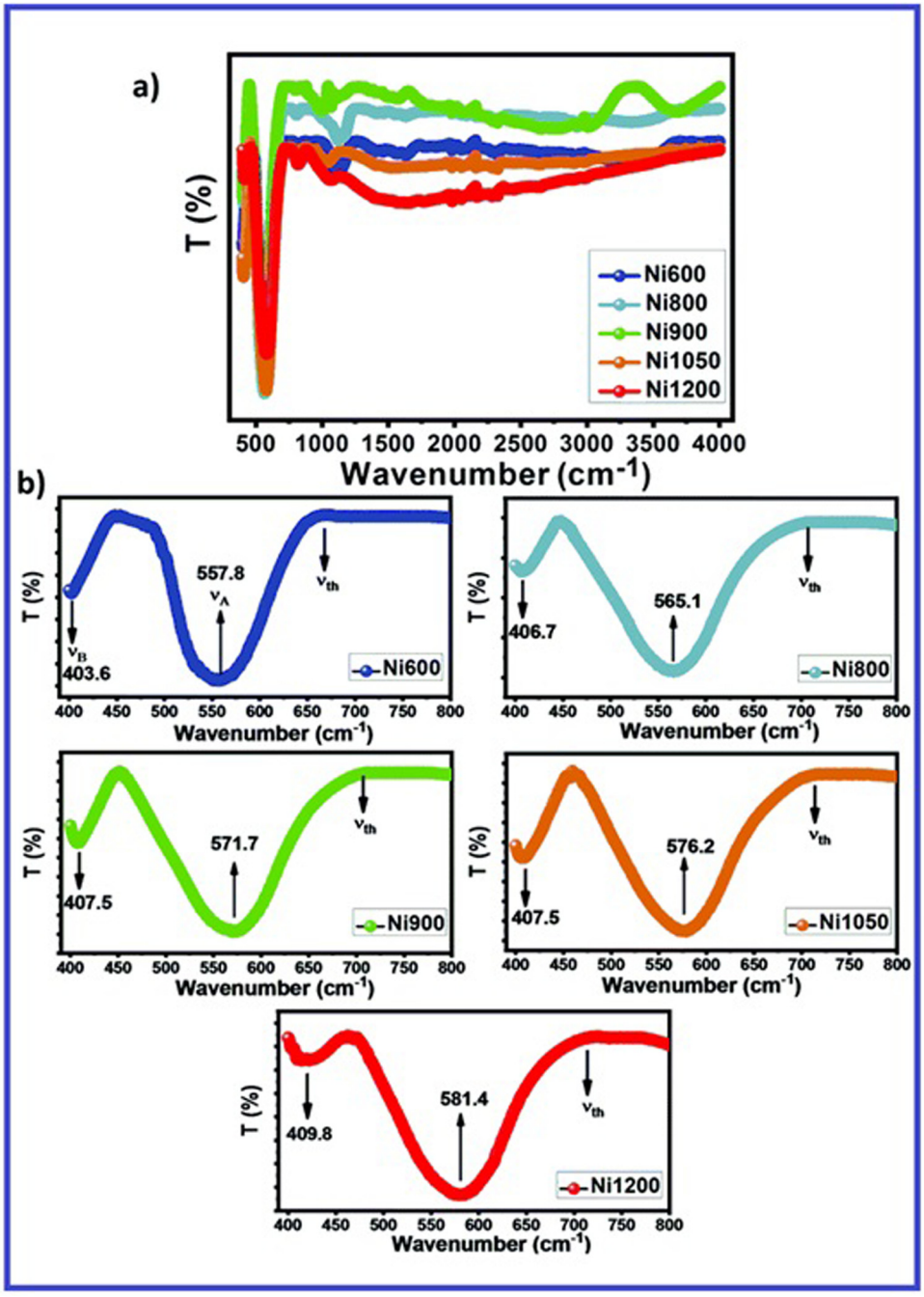

Figure 12: FTIR spectra of $Ni_{0.6}Zn_{0.4}Fe_{1.5}Al_{0.5}O_4$ at different annealing temperatures. Adapted from ref. [96] with permission from Elsevier™.

material magnetization fully diminished, which is termed coercivity (H_c) [100].

4 SFNPs for anticancer applications

Hyperthermia treatment for different types of cancer depends on the increase of the heat from 42 to 46°C in cancer cells by SFNPs [101,102]. It is classified into the whole body, regional, and local hyperthermia upon the position of cancer cells [103,104]. Hyperthermia is considered a targeted differential therapy because cancer cells are more sensitive than normal cells to hyperthermic effects [105]. The supermagnetic SFNPs absorb energy by the alternated external magnetic field and release it as heat by magnetic relaxation mechanism or hysteresis [11]. Hyperthermia therapy is a form of medical treatment that involves raising the temperature of tissues to kill

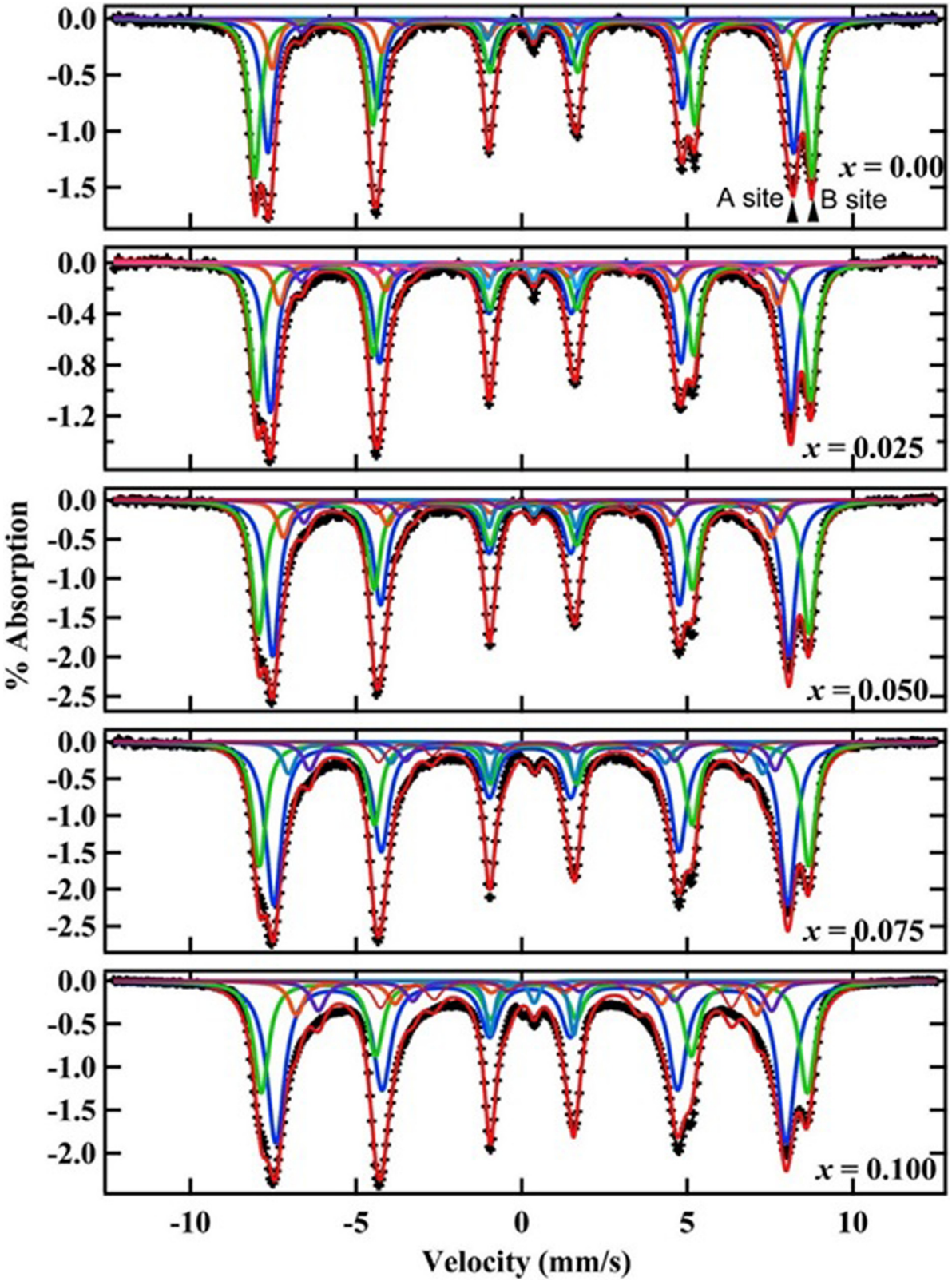

Figure 13: Room temperature fitted Mössbauer spectra of $NiGd_xFe_{2-x}O_4$. Adapted from ref. [98] with permission from Elsevier™.

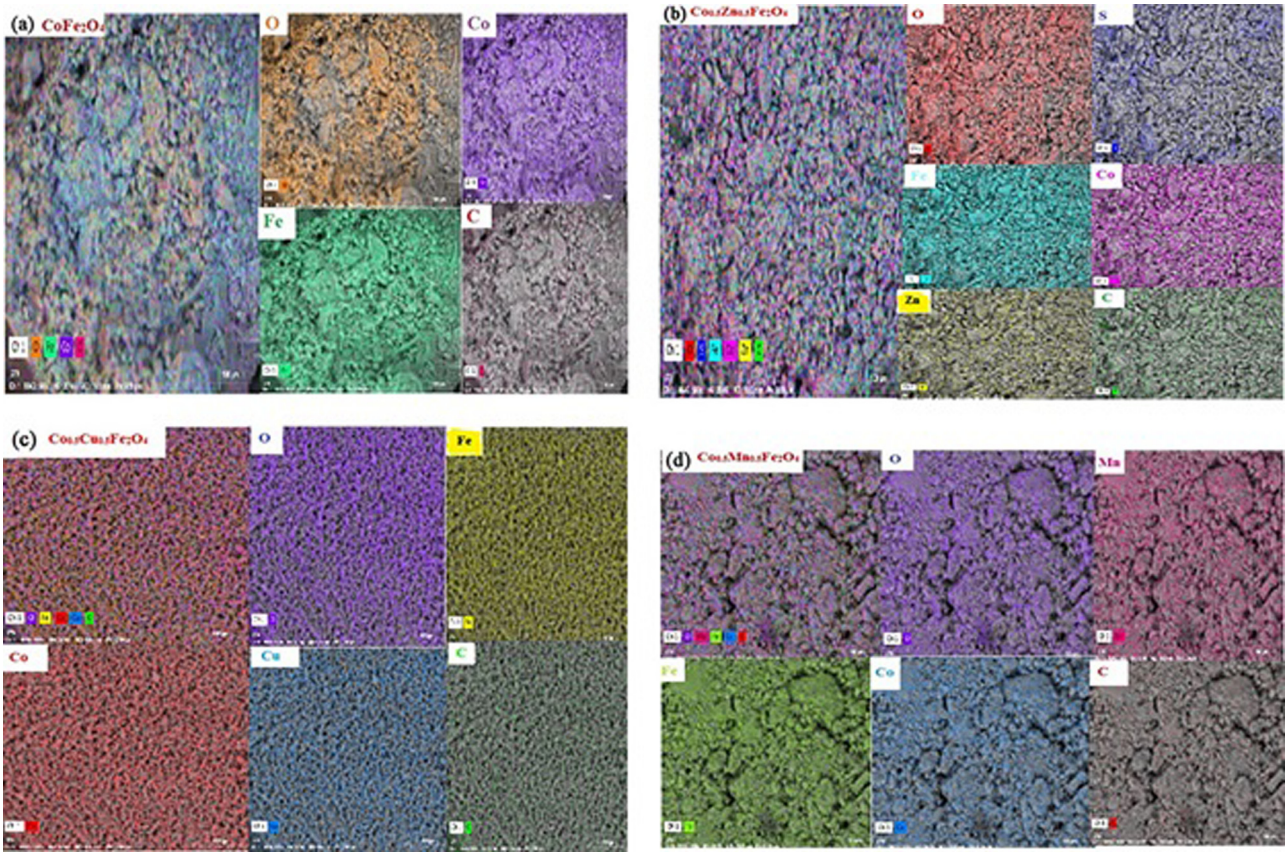

Figure 14: Elemental mapping images of (a) $CoFe_2O_4$, (b) Zn–Co/Fe_2O_4, (c) Cu–$CoFe_2O_4$, and (d) Mn–Co/Fe_2O_4. Adapted from ref. [35] with permission from Elsevier™.

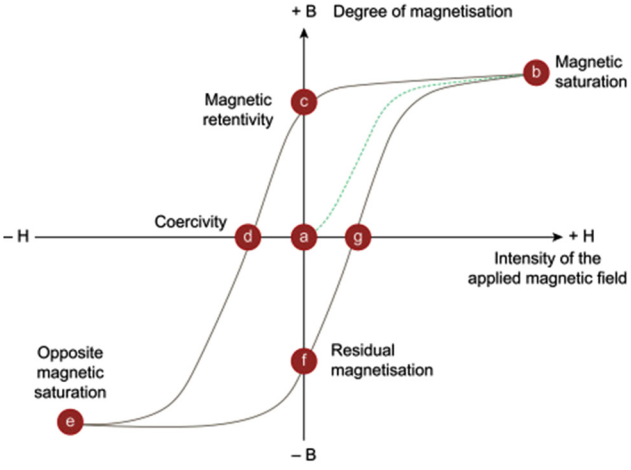

Figure 15: *M-H* plot of SF. Adapted from ref. [99] with permission from Elsevier™.

cancer cells or become dysfunctional [106]. Localized temperature increase allows the therapy to be limited to the diseased regions, which is very significant in anticancer therapies. Conventional cancer treatments are frequently linked to the harm they cause to healthy tissues and can result in long-term adverse effects. As a result, one of the primary advances in magnetic hyperthermia treatment is local cell heating. These promising techniques arise from a combination of magnetic oxides with an external oscillating magnetic field, and commonly SF has been used. The unique physiochemical characteristics of SF like low toxicity and high biocompatibility candidate them to various biomedical applications including drug delivery and magnetic hyperthermia treatment [9]. The significant advantages of SFNPs are their high surface-area-to-volume ratios, which make attaching a large number of therapeutic molecules simple, and their magnetic characteristics, which aid in MRI imaging of drug delivery.

The hyperthermia method to treat cancer tumors involved the injection of SF directly into cancer tumors with alternating magnetic fields (AMFs) to produce effective heat. The conditions should be achieved such as (1) the SF particles concentration in the tumor should be higher than that in normal tissues and (2) the SF particles should have a high specific absorption rate (SAR)

$$\mathrm{SAR} = \frac{c\Delta T}{\Delta t}(\mathrm{SAR, in\ Watts\ per\ gram}),$$

where T is the temperature increase during the time interval (t) to give substantial intratumoral doses of heat using AMFs well-tolerated by normal tissues, and c is the specific heat capacity. The SAR is maximized by four parameters to optimize heating in an AMF: (1) dielectric losses in SF has low electrical conductivity; (2) eddy current losses in SF has high electrical conductivity; (3) frictional heating is from the physical rotation of an anisotropic SF particle; and (4) hysteresis losses in an SF. Cancer cells were damaged by the generated heat, based on external field amplitude square, frequency, size, and type of SFNPs [107,108]. The SFNPs of less than 20 nm were releasing heat by Neel relaxation mechanism while Brown relaxation mechanism in case of large NPs size. The frequency and amplitude of the applied external magnetic field would be $>0.5 \times 10^{10}$ A/ms [109], and NP sizes range from 10 to 100 nm for safe hyperthermia cancer therapy [110].

Figure 16 shows the SAR dependence on smaller NP size, whose size closer to the single domain is desirable for high SAR than the multidomain [111]. If bulk particles have multiple domains, it is limited to be used in magnetic hyperthermia treatment due to magnetization reversal taking place by the magnetic moments flipping in domains where it is antiparallel to the AMF. It also occurs by domain growth in other domains, which occurs at lower

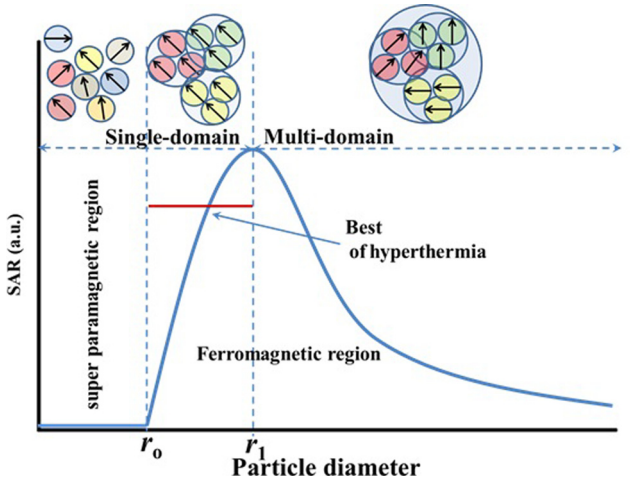

Figure 16: The dependence of SAR on the NP size. The domain magnetic structure of the SF particle would fall into the SPM region (dis-alignment) if their diameter size is smaller than the critical size r_o; in contrast, if the size of the SF particle is bigger than r_o, the SPM states transform to a single domain (full alignment); and if the size increases to twice the critical size r_o, the magnetic structure of SF transforms to the multidomain region. As a result, particles in the $r_o - 2r_o$ size range are predicted to be used in hyperthermia cancer therapy.

fields. If the applied magnetic fields can fully saturate the magnetization, then the energy losses in multidomain materials depend on coercivity. Jordan *et al.* [112] investigated at all applied magnetic fields (up to 165 Oe (13.2 kA/m) and found that the power loss in single-domain SFNPs was substantially larger than that in multidomain SFNPs. Thus, for fully saturated magnetic materials, the power loss should decrease with an increase in the domain size. As a result, to minimize the power loss, multidomain particles should be avoided.

It was also highlighted that SF has the potential to be outstanding contrast agents with respect to MRI image quality contrast, sensitivity, and specificity, as well as potential drug-loaded nanocarrier targets. SF exhibits magnetic anisotropy, which is influenced by the anisotropy of the cations, the symmetry of the interstitial sites, as well as the metal type content and cationic arrangement; some toxic cations such as Sr, La, Y, Mn, Ag, or Al should be avoided. Within the close-packed arrangement of 32 oxygen ions, most SFs contain a cubic unit cell belonging to the *Fd3m* space group, in which 24 metal ions are arranged in 8 tetrahedral and 16 octahedral positions. The substituted cations such as Ni, Cu, Co, Mn, Mg, and Zn cause O_2 displacement due to the substitution of cations at the tetrahedral sites and have to be expanded. On the other hand, the decrease in the lattice constant in SF systems can be explained by several factors: (1) the doping cation has a smaller ionic radius than the excited cation; (2) a potential rearrangement of Fe^{2+} and Fe^{3+} ions takes place inside the tetrahedral/octahedral ionic sites, leading to significant changes in magnetic characteristics; (3) Fe^{3+} is forced to the tetrahedral sites by a proportion of Fe^{2+} ions occupying the octahedral sites against their structural preferences that affect the optical, electrical, and magnetic properties of SFs [113]. In general, the magnetic behavior of SFs is highly dependent on the cation distribution between tetrahedral and octahedral sites [114]. Because the octahedral site and tetrahedral site spins align antiparallel, one can increase the magnetization in SFs by substituting cations for ferrous and ferric ions. For example, the substitution of Zn^{2+} by Fe^{2+} cations in the tetrahedral site gives $ZnFe_2O_4$, which exhibits magnetic behavior than Fe_3O_4 along with high magnetic saturation due to Zn^{2+} and Fe^{3+} cations occupying tetrahedral and octahedral sites, respectively. In general, smaller positive ions prefer to occupy the lower coordination site, *i.e.*, the tetrahedral site, due to their relative sizes. The larger positive ions tend to occupy higher-coordination sites, such as octahedral sites [115]. As the Zn fraction increases in the tetrahedral site, the magnetization increases. This approach of cation

substitution must be carefully chosen to maximize magnetization in SFs [116].

Furthermore, cationic interactions, surface anisotropy, and shape anisotropy all contribute to increasing total magnetic anisotropy in a single-domain structure [117]. An increase in temperature to about 42°C causes an increase in the tumor blood flow, which may be advantageous for simultaneous administration of chemotherapeutic drugs. This suggests that there is a temperature range in which cancer cells may be killed with little damage on normal cells, which is a key issue when utilizing hyperthermia for treating cancer and increases their anti-tumor effectiveness by loaded drugs. The development of SF has increased the interest of the scientific community in magnetic hyperthermia studies during the last years. Zhang *et al.* optimized the Curie temperature of 45.7°C and coercivity magnetization of 174 Oe for Cr^{3+}-substituted Co–Zn/Fe_2O_4 ($Zn_{0.54}Co_{0.46}Cr_{0.6}Fe_{1.4}O_4$) for use in magnetic hyperthermia [118]. Hanini *et al.* prepared cubic SF of $Zn_{0.9}Fe_{0.1}Fe_2O_4$ that exhibited a Curie temperature of 92.8°C under an applied magnetic field of 50 kOe. When $Zn_{0.9}Fe_{0.1}Fe_2O_4$ was incubated with glioma cells (U87-MGs) for 4 h at a low dose (0.05 g/L), they exhibit a significant increase of temperature (41.5°C) in a few seconds that is enough to kill malignant cells [101].

Lee *et al.* [119] loaded doxorubicin (DOX) as an anticancer drug into mesoporous silica-coated magnetite nanocrystals, and their surface was modified with PEG and fluorescence. Both MIR and fluorescence imaging verified *in vivo* passive targeting and accumulation of NPs at tumor sites. The DOX drug was successfully delivered to the tumor region in mice (the DOX accumulation compared with a control group was analyzed by terminal deoxynucleotidyl transferase-mediated nick end labeling (TUNEL) assay).

Remarkably, utilizing a hybrid design of a carbon covering of SF for cancer therapy appears to be highly promising. Carbon can solve and limit the main problems resulting in biomedical uses such as the possible toxicological consequences of long-term exposure, as well as low loading capacities and poor dispersibility under physiological conditions. It is known that carbon ions increase the biocompatibility of different biomaterials used and it reduces the immunohistochemical results in the body [120,121]. Gorgizadeh *et al.* [122] fabricated an SF coated by the carbon ion ($NiFe_2O_4$/C) nanocomposite and used it successfully as an effective agent for photoabsorbing in the photothermal therapy toward the melanoma cancer mouse model of C540 (B16/F10) cell line. Because of the excellent thermal conductivities of the carbon coating as well as electrical conductivities, the efficiency of the ($NiFe_2O_4$/C) nanocomposite conversion of light to heat is high. Furthermore, the hybrid design of the ($NiFe_2O_4$/C) nanocomposite assisted in the creation of a more targeted and definite treatment procedure, resulting in fewer side effects and lower toxicity in normal tissues.

As mentioned above, $ZnFe_2O_4$ and $CoFe_2O_4$ NPs have been widely studied for electronic applications owing to their self-interaction characteristics and their ability to respond to an external magnetic field. Combining both SF ($ZnFe_2O_4$ and $CoFe_2O_4$) components through the uniform distribution of MWCNTs show high adsorption of reactive pharmaceutical and biological species because of their large surface areas, leading to their high adsorption to the promoted adsorption of SF/MWCNT nanocomposites on the surface of the target cell.

Furthermore, rather than employing a carbon coating, as can be seen, a number of publications have shown success with alternative coatings, such as hydrogel (chitosan (CS), polyethylene, and phospholipids), which indicates a high efficiency for SF tumor cell adherence [123].

Zhang and Song developed injectable and biodegradable SF-based dual thermo- and magnetic-sensitive poly (organophosphazene) hydrogels for multiple magnetic hyperthermia therapy and MRI contrast [124]. This system is intended to serve as a multipurpose theranostics system due to the following: (1) because of the fast sol–gel transition of the hydrogel after a single injection, SF is retained within the tumor for a long time; (2) a minimally invasive multiple magnetic hyperthermia treatment at a reasonable temperature significantly improves anti-cancer therapeutic results; and (3) acting as a simultaneous long-term MRI contrast to guide and monitor the treatment procedure. Combining the hydrogel with SF loaded by drugs has several advantages, including preventing aggregation, enabling secondary drug functionalization, and providing carrier protection from the body's immune system, all of which increase circulation duration. Bisht *et al.* [125] synthesized SF nanocomposites poly(*N*-isopropyl acrylamide)-ferrite *via* supercritical CO_2-assisted synthesis. Drug loading and release profiles of 10 mL DOX drug were studied by varying the pH of the nanocarrier. The polymer nanocomposites exhibited enhanced drug release activity (20.98–76.54% release efficiency) and better biocompatibility in breast cancer cells (cell viability of 81–93%) as compared to spinal ferrite NPs.

Furthermore, the hydrogel-coated SF has functioned well in both covalent and noncovalent drug-loading processes, allowing access to a variety of drug release mechanisms such as external stimuli control or physiological condition-based adjustment within cancer areas. It selectively targets cancer cells and receptor engagement resulting in particle endocytosis; Figure 17 shows the coated spinal ferrite with polymer and active targeting groups.

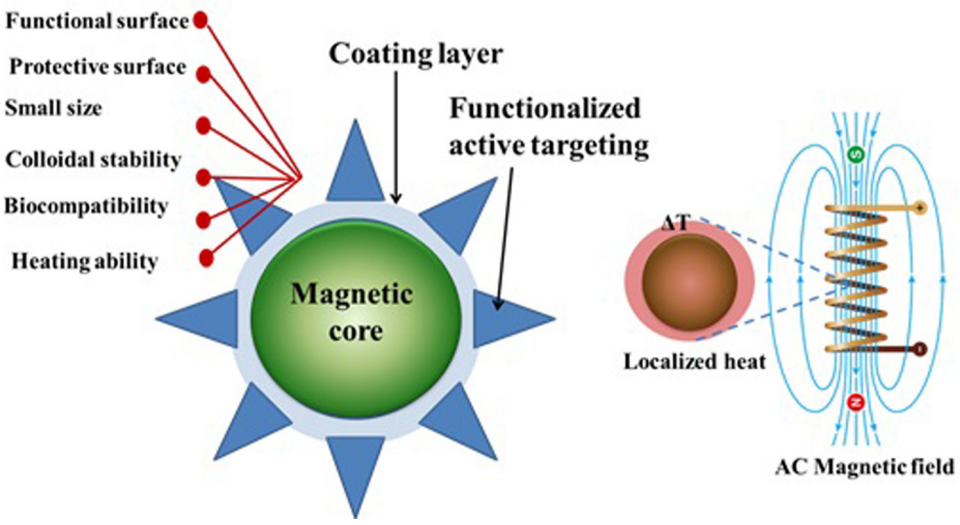

Figure 17: The SF coating with a polymer, the control of SF particle size, shape, biocompatibility, dispersion, and quality. Because of the unique multifunctional characteristics resulting from the wide diversity of functional groups within the polymer structure, it is likely to improve the hyperthermia therapy of SF. This coating layer can also protect SF surfaces against proteins, cell adsorption, and tissue penetration, extending particle circulation duration for *in vivo* hyperthermia applications.

The physicochemical properties of spinal ferrite are very sensitive to the change in their crystal form and particle size. Almost cubic SF crystal structures exhibit inherent characteristics such as ferromagnetic, antibacterial, and photodegradation activities than sphere-like SF [126]. Complex surface/interface interactions and the crystallite size effects resulting from the breaking of the symmetry of exchange bonds at the particle surface's boundary are also crucial for determining the magnetic behavior *via* the formation of spin canting at the particle surface, affecting their different magnetic performances. According to the literature, it seems that the cubic SF crystal structure has only been examined for biomedical applications. The obtained results are extremely impressive, showing great potential in some fields like hyperthermia, drug delivery, and MRI applications. For example, Wang *et al.* [127] designed hybrid nanocubes of Fe_3O_4@MoS_2 that had a superior SPM with a high surface area of 97.16 m^2/g, without aggregation results or the restacking of MoS_2 layers. It also demonstrated great magnetic sensitivity and good solution dispersibility, making it suitable for a variety of biological applications; on the hybrid design, to improve blood circulation time and medication accumulation at cancer locations, as well as to make drug loading easier. Xie *et al.* [128] designed and modified nanocubes of Fe_3O_4@MoS_2 using PEG and 2-deoxy-D-glucose (2-DG) for targeted chemo-photothermal therapy. The obtained Fe_3O_4@MoS_2/PEG/2-DG exhibited a great chemo-photothermal effect with a relaxivity coefficient of T_2 = 48.86/mM s and fast MRI signal detection of tumor sites with high contrast after injection.

The synthesis method can contribute to achieving the desirable properties for targeted drug delivery and hyperthermia applications. Recently, Almessiere *et al.* [129] have used two different techniques, citrate sol–gel combustion and sonochemical techniques, to synthesize Dy- and Y-codoped MnZn NPs. The principal aim is to compare the synthesis techniques and examine their biological applications by investigating antibacterial and anticancer activities. The different yttrium (Y) and dysprosium (Dy) ions doped Mn-Zn/Fe_2O_4 showed different magnetic behaviors attributable to the difference between the crystallite sizes of the prepared samples *via* the two synthesis methods. The prepared SF with a size less than 50 nm exhibited a broad SPM nature. The XRD results revealed that the synthesized samples *via* the sol–gel technique have a crystallite size of less than 40 nm, whereas the synthesized samples using the sonochemical method showed a crystallite size of less than 10 nm. Also, the magnetic properties at T = 10 K revealed closed hysteresis loops have nonneglected coercivity values ranging between 360 and 610 Oe for synthesized samples *via* the sol–gel method and from 320 to 695 Oe for the synthesized samples *via* ultrasonic synthesis. Further, the remanence ranged between 3.2 and 10.5 emu/g for the synthesized samples using the sol–gel method, whereas the remanence ranged between 16.2 and 26.6 emu/g in the ultrasonication route. The SEM images unveiled clusters of small cubic NPs for

the samples prepared through the sol–gel method and fine spherical NPs for the samples prepared *via* the ultrasonication method. Besides, the DyY-MnZn NPs prepared *via* the ultrasonication method produced better inhibitory action on the cancerous cells as compared to those produced *via* the sol–gel method. The morphology of cancer cells was investigated by confocal scanning microscopy, and results showed that with the treatment of DyY-MnZn, there was an evident loss of cancer cells prepared *via* the ultrasonication and sol–gel methods as DAPI staining was detected to be notably reduced in the cancer cells.

Hassanzadeh-Tabrizi *et al.* [130] produced a cobalt ferrite/hydroxyapatite (HA) nanocomposite using a novel multistep depositional technique for the design of a homogeneous core–shell blend. Controlled drug release trials revealed that the prepared nanocomposite is capable of loading of drug and controlled drug delivery up to 50 h. Furthermore, the quantity of heat produced may be controlled using varying magnetic fields or cobalt ferrite to HA ratios, making it potential for a variety of magnetic-based hyperthermia treatments. The incorporation of hydroxyapatite on the surface of cobalt ferrite NPs greatly promotes cell compatibility while reducing magnetization saturation. The findings show that a multifunctional nanocomposite of cobalt ferrite/HA with a homogeneous structure could be useful in medical applications. Figure 18 shows SEM images. The particle size of the cobalt ferrite generated ranged between 50 and 500 nm, with random and octahedron-like morphologies. After immersing the particles in KH_2PO_4 solution, their surface shape entirely changes. On the surfaces of the particles, spherical and needle-shaped HA precipitates developed. According to Wijesinghe *et al.* [131], HA crystals can have a variety of morphologies depending on the process and conditions of synthesis. They found that adding 10% HA to cobalt ferrite lowers the specific surface area. The surface area of the samples was significantly enhanced when a higher amount of HA was added to the samples compared to pure HA. The surface areas of CoFe-30HA and CoFe-50HA samples were found to be quite large. As a result, these specimens were chosen to receive the ibuprofen (IBU) medication. The release of IBU from NPs was considerable in the early stages but it progressively reduced over 72 h. The extremely early release may be due to IBU dissolving rapidly on the surface of NPs. The gradual release was induced by the physical and chemical interactions between the NP surface and IBU, which led IBU to be released from the samples' mesoporous structure. The initial release rate in this work is lower than several previously produced substances. Ansari *et al.* [132] studied the quick release of IBU from $Cu_{0.3}Zn_{0.2}Mg_{0.5}Fe_2O_4$ in the early hours (65%). Furthermore, the loading capacity in their study was just about 10%. The type of the material surface and its mesoporous structure are two elements that contribute to the variances in the release rate and loading capacity. Static and hydrogen interactions bind IBU molecules and NPs together. As a result, the surface of the produced NPs in the Hassanzadeh-Tabrizi *et al.* study [130], which comprises hydrogen groups and Ca^{2+} ions, can form active sites on the NPs' surfaces, making it more effective to connect with IBU's carboxylic acid groups. Wu *et al.* [133] demonstrated that Ca^{2+} ions might interact with the carboxylic groups of IBU molecules due to their alkalinity. Alkaline earth metals could produce basic sites, according to Khamsehashari *et al.* [134], leading to improved bonding with IBU's carboxylic groups. As a consequence of the effective factors for linking IBU molecules and cobalt ferrite/HA, more bonds are created, enabling the drug molecules to bind to samples with greater loading capacity and disperse from the material at a slower pace. When comparing the two samples, it can be observed that the CoFe-50HA sample exhibited a greater drug release. Because materials with bigger pores and higher pore volumes may contain more drug molecules, drug molecules trapped in these pores can naturally be released at a quicker pace. The retention of magnetic properties and the acquisition of optimum magnetization values are critical in drug release applications. The ferromagnetic behavior of the manufactured samples may be seen in their hysteresis loops (Figure 19). $CoFe_2O_4$, CoFe-10HA, CoFe-30HA, and CoFe-50HA have saturation magnetization values of around 59.9, 43.4, 18.3, and 11.4 emu/g, respectively. Thus, it can be observed that as HA increased, the saturation magnetization decreased. The CoFe-30HA composite exhibits a greater heating efficiency than samples with larger HA contents, particularly in high field zone, according to magnetic hyperthermia experiments. The magnetic characteristics of ferrites are affected by a variety of parameters, including particle size, shape, composition, defects, ion distributions, and even the synthesis method. For example, increasing the calcination temperature resulted in larger particles, which led to greater saturation magnetization [135]. Because the size of $CoFe_2O_4$ particles and the parameters of synthesis were kept fixed throughout the investigation, these variables had no significant impact on the magnetic properties. A decrease in the saturation magnetization of HA-coated Co ferrite NPs could be linked to the spacing of nearby NPs by a diamagnetic coating of HA, resulting in a reduction in the static interaction among them. Based on prior investigations, it was stated that a 10–30 emu/g magnetization is adequate for therapeutic purposes [136]. Furthermore, when the amplitude of the field increases,

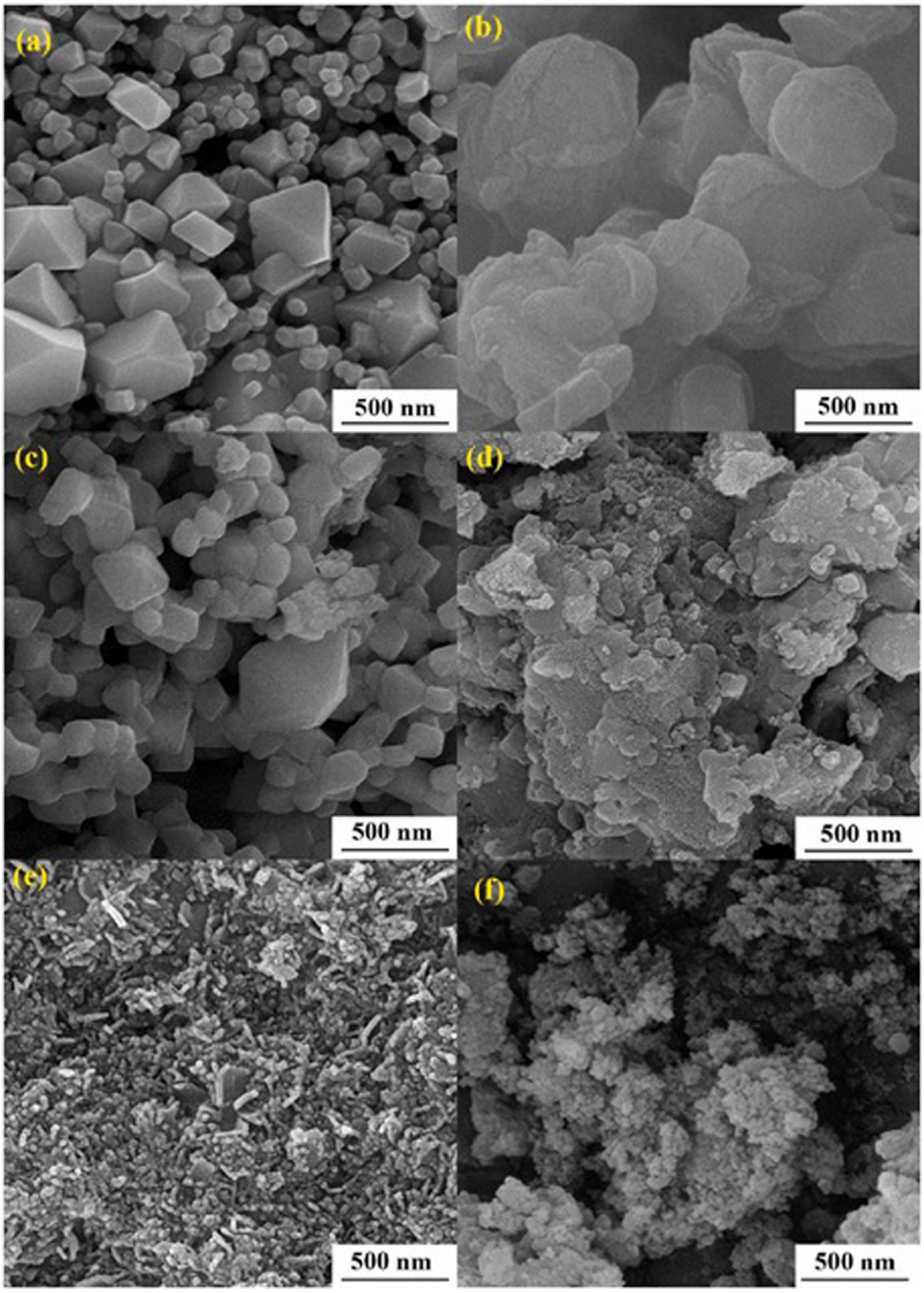

Figure 18: SEM images of cobalt ferrite NPs: (a) pure, (b) 50Ca, (c) 10HA, (d) 30HA, (e) 50HA, and (f) HA. Adapted from ref. [130] with permission from Elsevier™.

the temperature increases. By regulating the time and applied AC field, the heating response of samples can be improved.

Sangeetha *et al.* [137] developed an intelligent drug delivery system and/or a hyperthermia carrier by creating a potential magnetic nanocomposite of $CoFe_2O_4$/HA and loaded a chemotherapy medicine (5-fluorouracil, FU). To achieve it, a microwave-aided wet precipitation approach was used to successfully synthesize a cobalt ferrite/hydroxyapatite nanocomposite, which was then loaded with FU using an adsorption method. With 2.5–8.2 emu/g magnetic saturation, this nanocomposite exhibits ferromagnetic behavior. Using an AMF, they were able to produce hyperthermia in a short amount of time (43°C in 4.5 min) and accelerate the release of encapsulated FU from the composite. These multifunctional carriers show

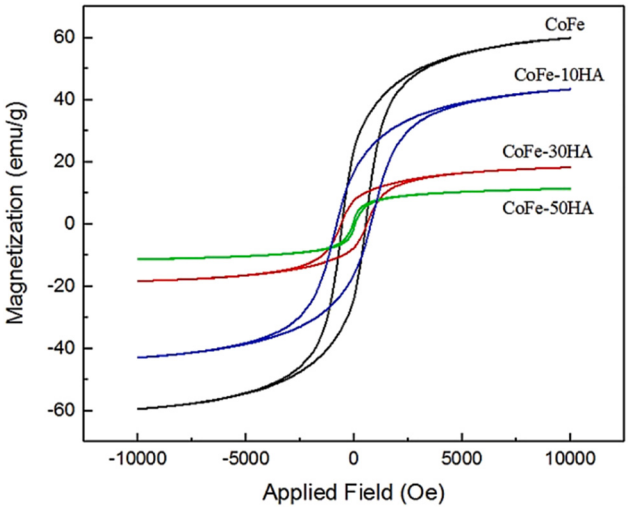

Figure 19: CoFe, CoFe-10, 30, and 50HA samples hysteresis curve. Adapted from ref. [130] with permission from Elsevier™.

significant proliferative activity against healthy fibroblast cells (L929) and impede the growth of osteosarcoma cells (MG63). As a result, this multifunctional nanoplatform could be a good option for synergistic chemo-hyperthermia therapy, allowing cancer patients to receive chemotherapy and hyperthermia at the same time. TEM analysis showed the core–shell structure of the composites in the calcined sample, and PEG addition enhanced the pore radius and specific surface area of the composites. The saturation magnetization of the composites calcined at 1,100°C was 8.075 emu/g. The produced composites could release FU for 7 days at physiological temperature and could be accelerated at hyperthermia temperature, increasing the proportion of FU released. According to the findings of this study [139], this thermo-responsive nanovehicle offers possibilities as a delivery mechanism for tumor-specific treatment at hyperthermic temperatures.

Talaei *et al.* [138] produced a magnetic mesoporous $CuFe_2O_4$@SiO_2 nanocomposite with a core–shell nanostructure by sol–gel combustion and examined it for simultaneous drug release and hyperthermia biomedical applications. Around copper ferrite, TEM images revealed the formation of thin mesoporous silica covering with a thickness of 14 nm (Figure 20). After surface modification of ferrite NPs with mesoporous SiO_2 layer, the surface area of the samples increased from 2.59 to 199.2 m^2/g. When compared to pure ferrites, the magnetic characteristics of core–shell samples were reduced. The drug IBU was used to test NPs' ability to store and release the medicine. IBU loading was high and the drug release was regulated in the $CuFe_2O_4$@SiO_2 system. Following the synthesis of a hybrid core–shell structure, the samples' storage capacity increased from 4 to 34%. The nanocomposite's mesoporous structure and increased surface area resulted in these enhancements. The rate of drug release was reduced when the calcination temperature increased but the release mechanism was unaffected. The cytotoxicity of $CuFe_2O_4$ NPs was lowered and the drug release characteristics were improved by coating them with mesoporous silica. This coating, however, limited the potential to generate hyperthermia. Although the capacity to heat the samples was reduced when $CuFe_2O_4$@SiO_2 was synthesized, it increased biocompatibility and drug storage. The results suggested $CuFe_2O_4$@SiO_2 be a promising option for medicinal applications as a hybrid system that can release medications and create heat at the same time.

Radmansouri *et al.* [139] combined titanium oxide NPs with cobalt ferrite NPs *via* microwave heating, which was subsequently electrospun into CS/cobalt ferrite/titanium oxide composite nanofibers. They tested the impact of DOX hydrochloride-loaded electrospun CS/$CoFe_2O_4$/TiO_2 nanofibers on melanoma cancer B16F10 cell lines to check whether heat and therapy could be combined. Cobalt ferrite NPs were made *via* microwave heating. Titanium oxide NPs were mixed with cobalt ferrite to control the temperature increase. The DOX loading efficiency and *in vitro* drug release of DOX from nanofibers were investigated using an AMF and without a magnetic field under physiological and acidic conditions. As seen in SEM images, the surface of nanofibers was smooth, and no drug crystals were visible on the nanofibers' surface (Figure 21). As a consequence, DOX molecules were well incorporated into electrospun fibers. The fastest

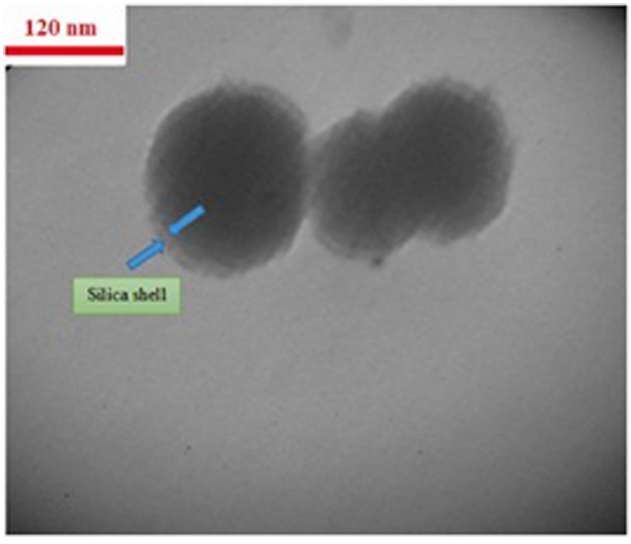

Figure 20: TEM image of the $CuFe_2O_4$@SiO_2 nanocomposite at 400°C. Adapted from ref. [138] with permission from Elsevier™.

release of DOX from the synthesized magnetic nanofibers was observed at acidic pH by changing the magnetic field. The anticancer effects of the nanofibers generated were also tested on the melanoma cancer B16F10 cell lines. According to the results, DOX-loaded electrospun CS/cobalt ferrite/titanium oxide nanofibers may be used for localized cancer treatment. According to *in vitro* cell incubation tests, simultaneous loading of DOX and cobalt ferrite/titanium oxide NPs into CS nanofibers following the application of a magnetic field enhanced the cytotoxicity of the nanofibers. The generated cobalt ferrite and cobalt ferrite/titanium oxide NPs had maximum saturation magnetization (M_s) values of 90.5 and 81.2 emu/g, respectively. The reduction in M_s of cobalt ferrite/titanium oxide NPs may be explained by the addition of titanium oxide NPs. The coercivity values (H_c) of NPs composed of cobalt ferrite and cobalt ferrite/titanium oxide NPs were 830 and 640, respectively. The fact that cobalt ferrite NPs are smaller and more homogeneous than the manufactured cobalt ferrite/titanium oxide composites may explain this behavior.

Wang *et al.* [140] created SPM cobalt ferrite/graphene oxide ($CoFe_2O_4$/GO) nanocomposites with MRI and controlled drug delivery through sonochemistry. The method is simple and effective, and GO nanosheets are uniformly coated with $CoFe_2O_4$ NPs ranging in size from 5 to 13 nm.

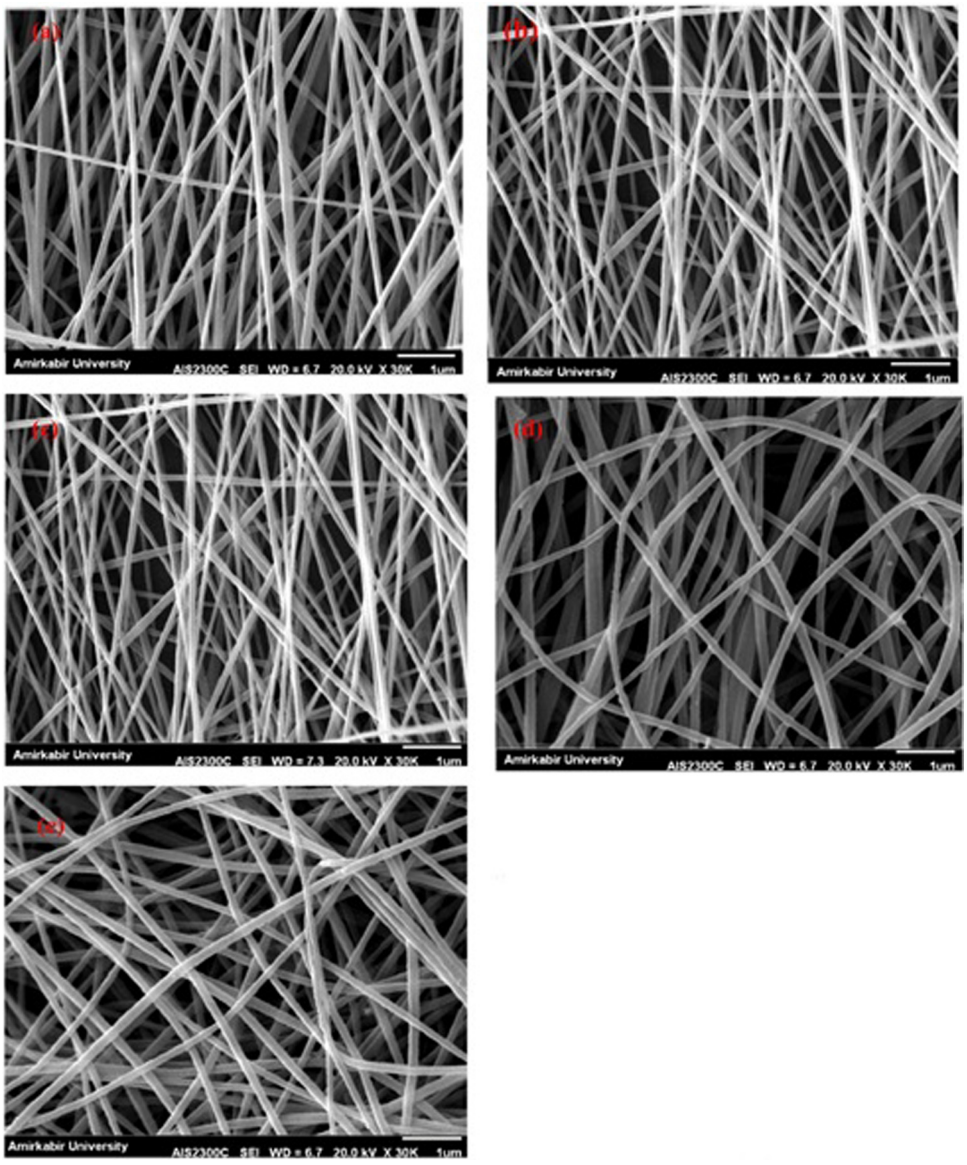

Figure 21: SEM images of (a) pure CS, (b) CS/$CoFe_2O_4$ (10 wt%), (c) CS/$CoFe_2O_4$ (20 wt%), (d) CS/$CoFe_2O_4$/TiO_2 (20 wt%), and (e) CS/$CoFe_2O_4$/TiO_2/DOX nanofibers. Adapted from ref. [139] with permission from Elsevier™.

The $CoFe_2O_4$/GO nanocomposites created have SPM properties, are hydrophilic, and have a low degree of cytotoxicity, indicating that they have a lot of potential in biomedical applications. On $CoFe_2O_4$/GO, DOX hydrochloride was loaded as an antitumor model drug. The nanocomposites were shown to be effective in transferring DOX into cancer cells and caused cell death. This nanocarrier had a drug loading capacity of 1.08 mg/mg, and the drug release behavior was delayed and pH-responsive, which is useful for preventing rapid drug release in the neutral circulatory system while promoting drug release at acidic tumor sites or inside cells. Suárez *et al.* [141] created a composite of CS and polyvinylpyrrolidone (PVP) with $CoFe_2O_4$ NPs for use in drug delivery systems and hyperthermia (see Figure 22 for a schematic depiction of the manufacturing process). They examined how the structural, magnetic, and SAR characteristics of $Co_xFe_{3-x}O_4$ (x = 0.25, 0.50, 0.75, and 1.00) as a hyperthermia heat nanomediator were influenced by CS and PVP. At a frequency of 454 kHz and a magnetic field amplitude of 5.5 mT, hyperthermia tests were conducted. At x = 1.00, CS–PVP-coated NPs had a maximum SAR of 386 W/g, compared to 270 W/g for untreated NPs. The coated NPs exhibit higher SAR values than the untreated NPs due to the presence of CS and PVP. The variable mixing of CS and PVP for heating cobalt ferrite NPs improves the biocompatibility and stability of the samples. The impact of changing the Co^{2+} concentration on the nanocomposite structure may alter magnetic characteristics, increasing hyperthermia SAR, and NPs coated with hydrophilic polymers enhance biocompatibility and SAR efficiency.

Daboin *et al.* [142] used the thermal decomposition technique to prepare magnetic mixed manganese–cobalt ferrite NPs ($Mn_{1-x}Co_xFe_2O_4$); then, they were coated with SiO_2 using the Stöber process and adorned with Au@Fe_3O_4 NPs. TEM images of the undecorated and decorated nanocomposites are shown in Figure 23a–f. These images show that the nanostructured material has a spherical shape and that Au@Fe_3O_4 NPs were successfully deposited on the silica nanocomposites' surfaces. They investigated the generated composite as magnetic fluid hyperthermia heat mediators using a hydrogel as a tissue equivalent. The SAR of the nanocomposites increased when they were decorated with Au@Fe_3O_4 in water. By integrating magnetic NPs, SiO_2, and Au@Fe_3O_4, the magnetic properties of the synthesized nanocomposite system may be fine-tuned to optimize SAR.

Mondal *et al.* [143] developed a $MnFe_2O_4$/ZnS magneto-fluorescent nanocomposite using a simple co-precipitation method. The NPs are near SPM at room temperature, with a small coercivity of 66 G, and saturation magnetization increases significantly after coating ZnS on the $MnFe_2O_4$ core surface. $MnFe_2O_4$/ZnS core–shell NPs have a magnetic saturation of 1.15 emu/g, which is higher than $MnFe_2O_4$ NPs. The Zn^{2+} ions induce cation rearrangement in the nanocomposites' interstitial regions, resulting in an increase in saturation magnetization. The heating efficiency of the $MnFe_2O_4$/ZnS core–shell nanocomposite is determined using the SAR and intrinsic loss property, which decreases with increasing sample concentration. Hatamie *et al.* [144] utilized GO/cobalt ferrite NPs to heat-treat the MCF7 breast cancer cell line. The ferrimagnetic NPs were 5 nm in diameter. The NPs were likewise uniformly distributed on the GO nanosheets. The cell survival rate was 58% after 72 h of NP treatment, suggesting that the IC_{50} had been reached. The vitality of the cells, on the other hand, was decreased by 30% following heat therapy. In addition, BALB/c mice were used in *in vivo* testing; the findings showed a reduction in tumor growth after 27 days with dosages of 0.001 and 0.002 g/mL and

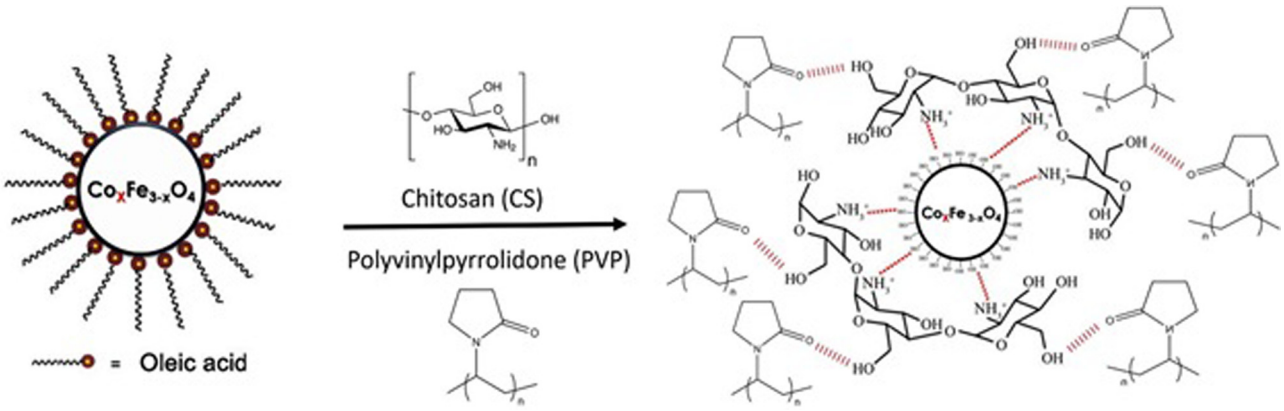

Figure 22: A schematic depiction of the synthesis mechanism of the composite of CS and PVP with $CoFe_2O_4$ NPs. Adapted from ref. [141] with permission from Elsevier™.

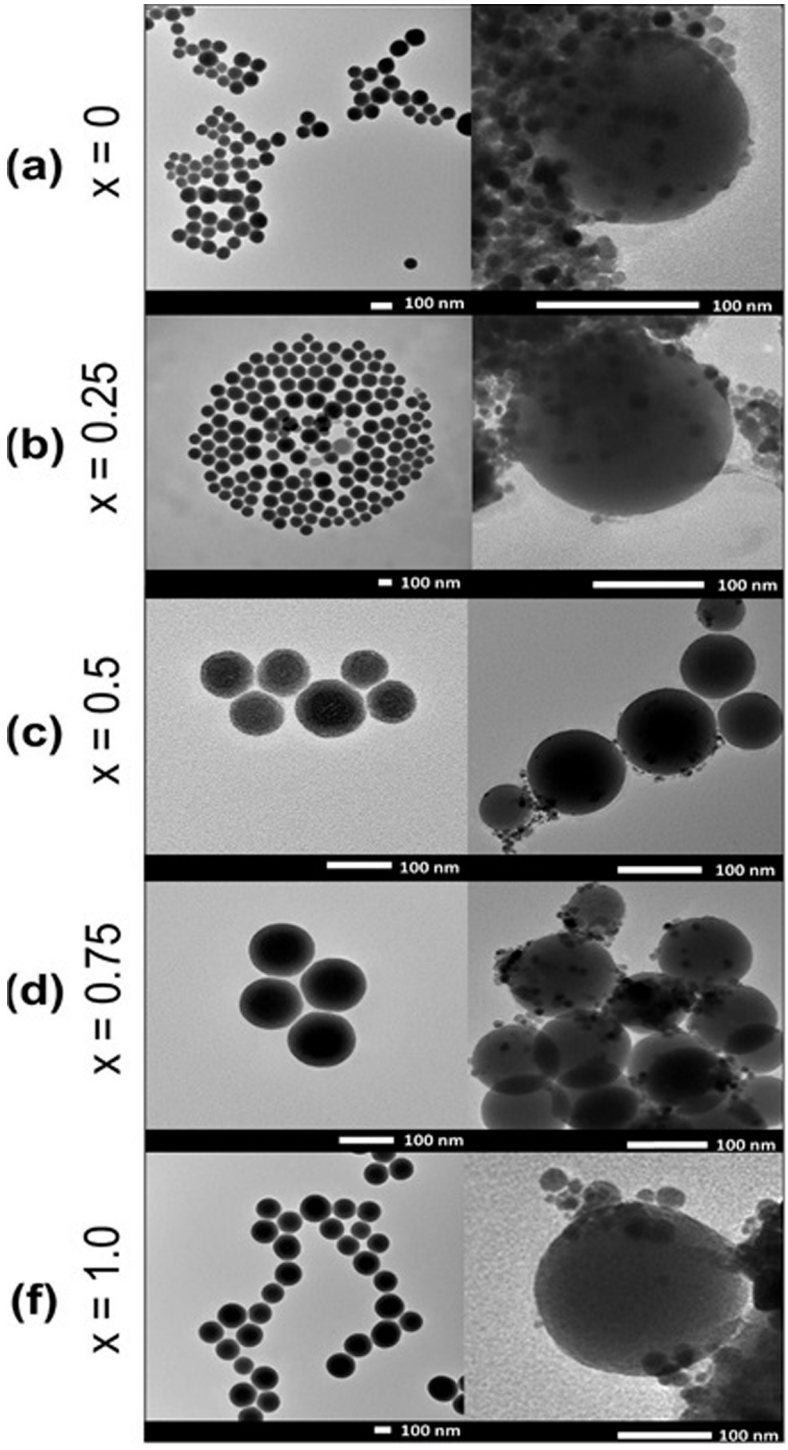

Figure 23: TEM images of the decorated (left) and undecorated (right) nanocomposites with varying Mn^{2+} contents. Adapted from ref. [142] with permission from Elsevier™.

corresponding magnetic frequencies of 400 and 250 kHz for 10 min. The MRI studies revealed the presence of NPs not only inside the tumor but also in adjacent tissues. The MRI validated dark spots as a representation of the presence of NPs and tumor disruption as a consequence of the hyperthermia procedure in contrast to the control group (see Figure 24). The molecular gene expression of the treated tumor showed a higher expression of apoptotic genes. Hematoxylin and eosin (H&E) staining, on the other hand, revealed that NP concentrations of 0.002 g/mL at

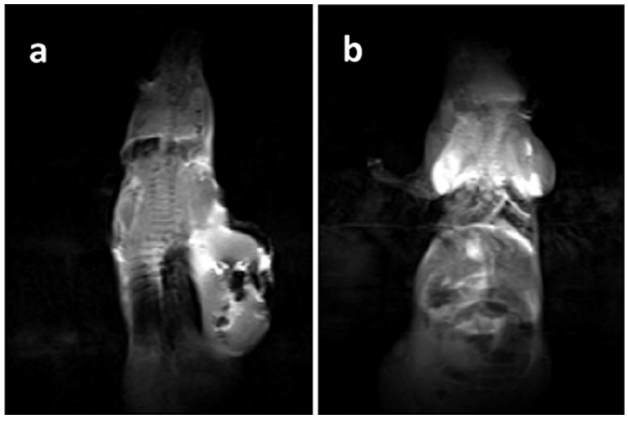

Figure 24: MRI scans of mice with (a) NPs and hyperthermia; and (b) NPs without hyperthermia treatment. Adapted from ref. [144] with permission from Elsevier™.

frequencies of 250 and 350 kHz disrupted the tumor cytoskeleton.

5 Selected doped SFNPs and their composites

Cobalt ferrite $CoFe_2O_4$ has a hyperthermic effect on cancer therapy and drug delivery [145]. Balakrishnan *et al.* [146] used the cubic-shaped cobalt ferrite NPs (Co–Fe NCs) as magnetic hyperthermia agents and as a cytotoxic agent ascribing to the distinguished cobalt ion toxicity, supporting both heat and cytotoxic impacts from a single platform (Figure 25a). The polymer-coated $CoFe_2O_4$ was injected intratumorally (i.t.). NPs were injected when the tumors were ≈80–100 mm^3 (day 0), followed by 30 min HT cycles on days 0, 1, and 2, totaling 3× HT cycles on three consecutive days (HT1, HT2, and HT3). The iron oxide cubic-shaped nanoparticles (IONCs) were injected into rats i.t. within the 3× HT (TEM; Figure 25b) or $CoFe_2O_4$ (TEM; Figure 25c); the tumor temperature (T_{Tumor}) and the skin tail temperature (T_{Skin}) were detected with an infra-red camera (Figure 25d). They found that $\Delta T = T_{Tumor} - T_{Skin}$ were about 6, 3.5, and 3.5°C for IONCs on HT1, HT2, and HT3, respectively; while, $CoFe_2O_4$ presented only ΔT of 3°C on HT1, HT2, and HT3. The detected reduction in the temperature for $CoFe_2O_4$ and $CoFe_2O_4$ in water was because the immobilized nanocubes in the tumor cells' viscous medium [147,148] caused a decrease in the release of heat from high anisotropy particles [149]. Also, they revealed that monitoring the temperature and cancer growth for 12 days post $CoFe_2O_4$ injection showed that the decrease of the growth of the tumor by Co–Fe NCs + hyperthermia, compared to Co–Fe NCs or the ions and the IONCs + hyperthermia, respectively, was nonsignificant (Figure 25f). Further, they compared the obtained IONCs + HT results with those of the previously revealed *in vivo* study [150]. Kolosnjaj-Tabi *et al.* [150] found that 18 nm IONCs-based hyperthermia monotherapy did not significantly decrease tumor growth [150]; while Mai *et al.* revealed that the combination therapy, IONCs hyperthermia + Doxo intravenous injection, enhanced the ions possessing cubic shape-based hyperthermia efficiency [151].

Figure 26a shows that the Co–Fe NC chains and prolonged cobalt toxicity were present, as confirmed by long-term *in vivo* study, resulting in decreased tumor growth and longer survival. It was focused only on Co–Fe NCs with or without hyperthermia efficiency. Also, Balakrishnan *et al.* [146] monitored the tumor size by digital photographs and showed that the tumor size was significantly reduced in the Co–Fe NCs + HT group than that in the Co–Fe NCs group compared to the control animals group on day 15 (Figure 26b). They revealed that the tumor was completely eradicated on day 30 after injecting Co–Fe NCs + HT i.t. without recurrence up to a post-treatment period of 200 days (Figure 26c). Furthermore, the survival rate was significantly higher in the Co–Fe NCs + hyperthermia group (about 200 days) than in the control group (22 days) and Co–Fe NCs group (30 days) (Figure 26d). As revealed in Figure 26e and f, the long-chain formation was confirmed by transmission electron microscopic images at day 30 for tumor tissues, indicating that strong interactions persisted for a long time. It was also shown that Co–Fe NCs were presented within the tumor at day 30, as indicated by histological Prussian blue staining (Figure 26g and h). The Co–Fe NCs + hyperthermia group showed a whirling movement of nanocubes from the tumor injected point to its peripheral surface, post exposed to an AMF (Figure 26h) [150]. The HT increased the chain length of injected Co–Fe NCs, resulting in mechanical damage to the cancer cells during the whirling movement of Co–Fe NCs. Marangon *et al.* [152] concluded that one of the important reasons for the tumor drug resistance was the tumor's outer collagenous peripheral layer. Even the damage or necrosis was induced centrally in the tumor post-treatment; the outer layer was rich in angiogenesis, and viable cells resulted in the uncontrolled growth of cancer cells. Balakrishnan group [146] presented that $CoFe_2O_4$ NCs were injected i.t. in rats to avoid nonspecific cobalt toxicity. Chu *et al.* [153] revealed that the i.t. injection in the case of cancer patients was accepted. The outer layer of the Co–Fe NCs + HT group was rich in collagen (darker pink) (Figure 26h) and cells (pink) in the outer layer had more toxicity at the peripheral region, which led to the destruction of stroma; while in the $CoFe_2O_4$ NCs alone group, cancer cells were still viable (Figure 26g). Finally, they found

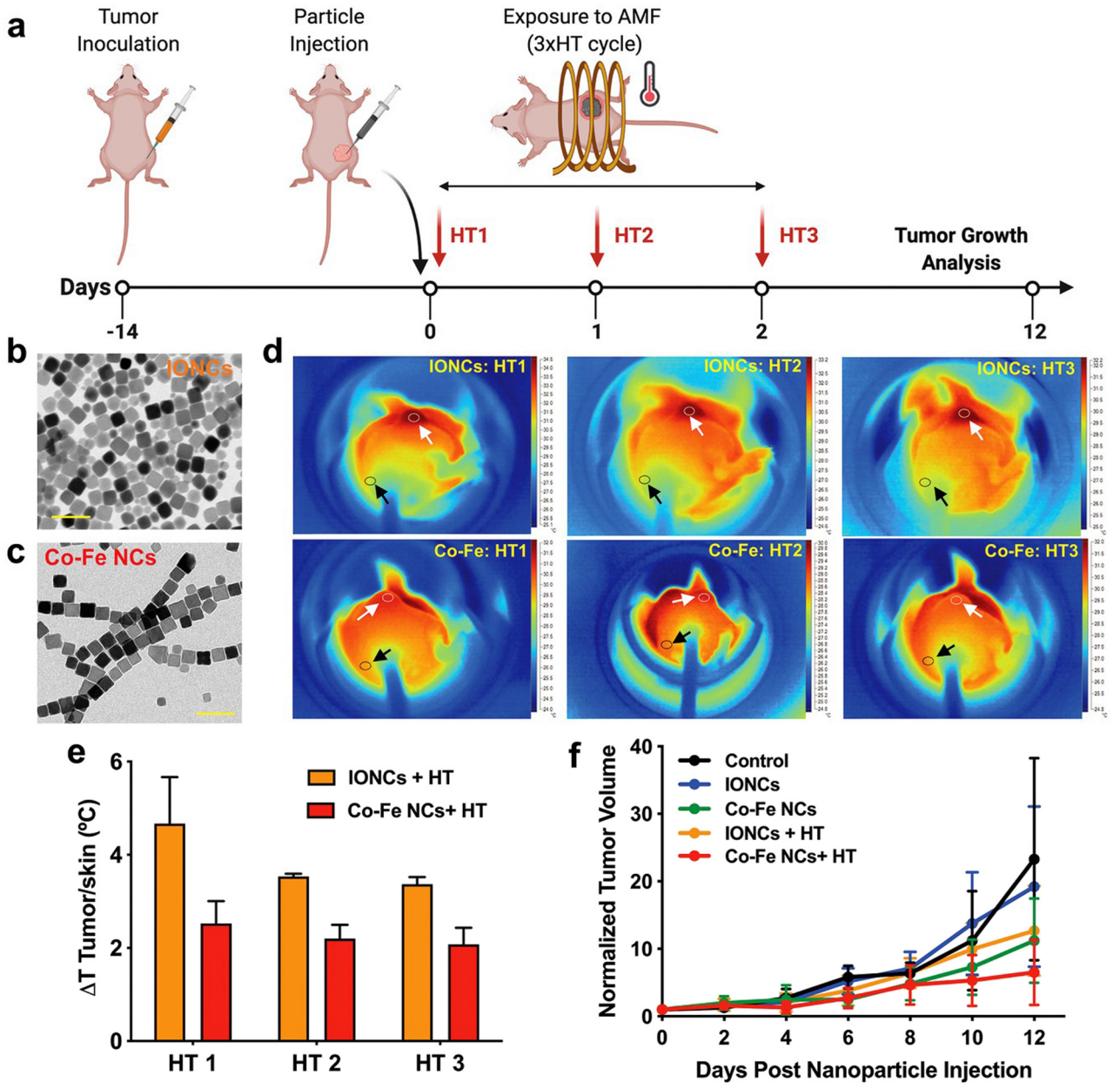

Figure 25: The efficiency of the ions possessing cubic shape-based hyperthermia and Co–Fe NCs during *in vivo* study. (a) Plan of the treatment. Particle injection is symbolized by a black arrow (0.7 mg Co–Fe NCs or 0.7 mg IONCs) and the days of HT therapy (3 × hyperthermia) are symbolized by red arrows, using AMF conditions. (b and c) TEM images of the ions possessing the cubic shape of particles (18 nm) (b) and sizes of poly(maleic anhydride-*alt*-1-octadecene-coated $CoFe_2O_4$ was (17 nm) (c) *In vivo* studies. Scale bar: 50 nm. (d) Mouse IR images post the ions possessing cubic shape and $CoFe_2O_4$ injection during hyperthermia therapy (HT1, HT2, and HT3). Cancer temperature is represented by white arrows, while skin temperature is shown by black arrows, to estimate ΔT values. (e) ΔT graph ($\Delta T = T_{Tumor} - T_{Skin}$) plotted for HT1 at day 1, HT2 at day 2, and HT3 at day 3 for (orange bars) the IONCs (*in vivo*) or (red bars) Co–Fe NCs. (f) Tumor or cancer growth curve represented the marginal decrease in cancer growth for Co–Fe NCs and exposed to 3× hyperthermia (Co–Fe NCs + hyperthermia) compared to Control, the ions possessing cubic shape alone; Co–Fe NCs alone, and the ions possessing cubic shape + hyperthermia; $N = 6$. Adapted from ref. [146] with permission from John Wiley and Sons.

that $CoFe_2O_4$ NCs + HT destroyed the outer tumor membrane completely, which led to the prevention of the recurrence or relapse of the tumor (Figure 26c) [146].

It is known that conservative drug delivery suffered from unstable metabolic tissue distribution and was non-targeted to cancer cells, which leads to a decrease in

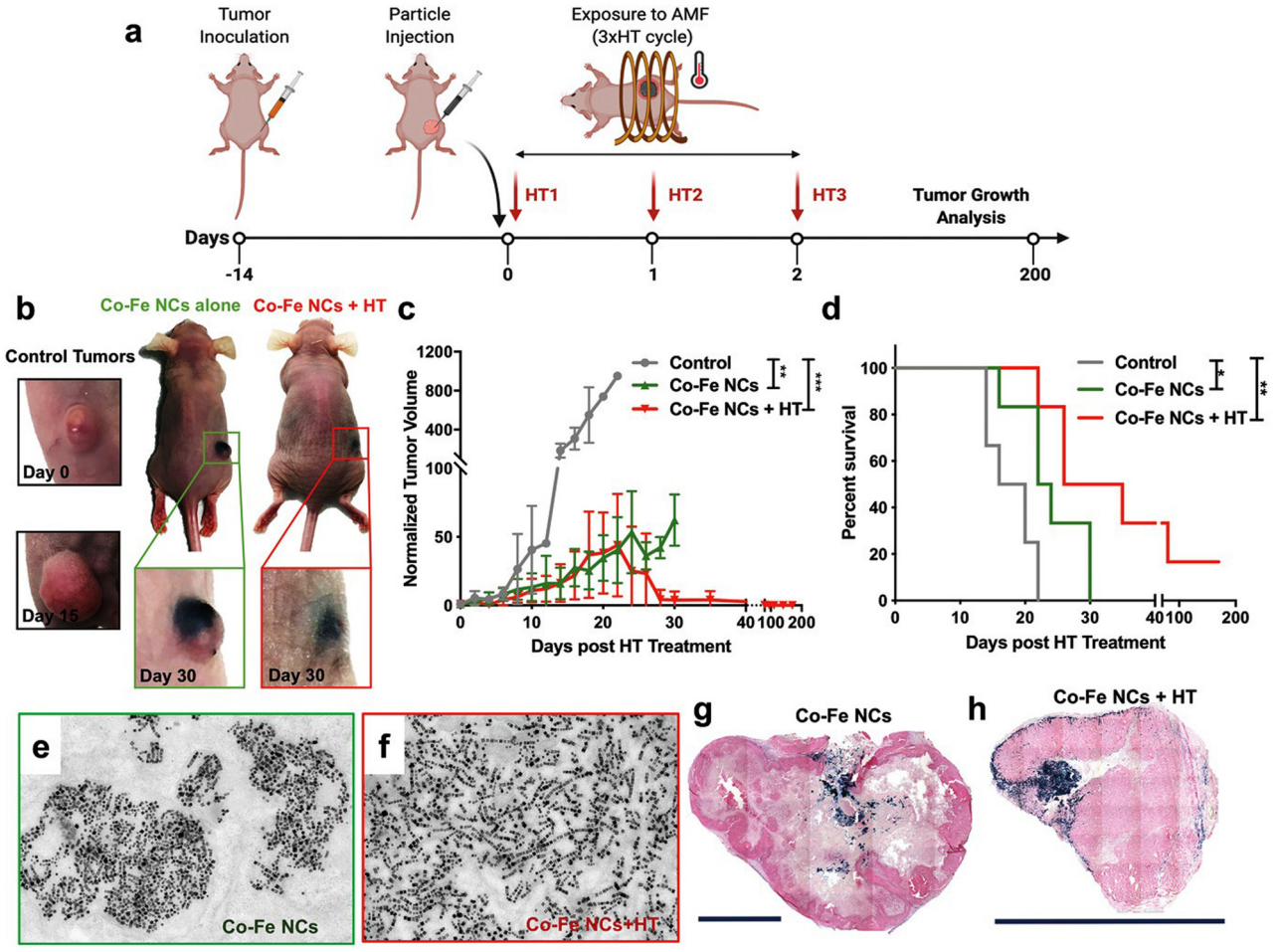

Figure 26: The efficacy of Co–Fe NCs during *in vivo* HT examination. (a) Diagram of plan therapy. (b) Images of a control animal (at 0 and 15 days) and Co–Fe NCs injected alone, and Co–Fe NCs injected + hyperthermia display the decrease and whole eradication of cancer 30 days after treatment, respectively. The treated cancer is represented by an enlarged image in boxes. (c) The complete eradication of cancer represented in tumor or cancer growth curve and no relapse up to 200 days in case of Co–Fe NCs + hyperthermia (*in vivo*). (d) A Kaplan–Meier survival graph indicating Co–Fe NCs + hyperthermia enhanced the survival rate up to 200 days after therapy, while in other groups for only one month. (e and f) TEM images proved that cancer cells have a chain shape even at one month after therapy for both Co–Fe NCs alone (e) and Co–Fe NCs + hyperthermia (f). (g and h) Light microscopy images of cancer slices of Co–Fe NCs alone (g) and Co–Fe NCs + hyperthermia (h) display the incidence of NPs and absence of stroma. Blue color representsNPs due to Prussian blue staining; dark-pink stained the collagen and light-pink stained the cells in the case of Fast Red staining. Scale bars in (g) and (h) are 0.5 cm. Adapted from ref. [146], with permission from John Wiley and Sons.

cancer therapy efficiency and increases whole-body toxicity [154]. On the other hand, cytotoxic drugs were efficiently delivered by encapsulating within polymer-SFNPs composite [155,156]. Ponce *et al.* [157] revealed that antibody-based drugs are bound to specific targets in cancer tissues. However, once the molecular targeted drugs were administered, their target did not change; while the magnetic drug delivery system was guided by a magnet by magnetic field exposure [157,158]. Namiki *et al.* [159] reported that cytotoxic anticancer drugs were combined with SPM particles [159,160] by micelle emulsification or ionic bond [161]. Gupta and Gupta [162] found that a targeted magnetic drug delivery system was widely used in tissue repair, enhancing contrast for magnetic resonance (MR) imaging, hyperthermic therapy, and cytotoxic anticancer therapy [116].

Especially in hyperthermia therapy, Fe_3O_4 and γ-Fe_2O_3 were preferred to Fe_3O_4 or γ-Fe_2O_3 NPs due to slower magnetic moment relaxation of $CoFe_2O_4$ than that with similar size [163,164]. The hyperthermic efficiency of $CoFe_2O_4$ NPs was improved by adding a trace amount of Zn^{2+} (5–15%) relative to cobalt (Co), while further addition of Zn^{2+}, more than 15% relative to Co, resulted in a reverse effect [165]. Likewise, the anticancer activity of $CoFe_2O_4$ NPs against

human colon cancer has been enhanced by trace Ce–Nd addition [166].

Besides, the cations of rare earth elements (REs) doped $CoFe_2O_4$ were found to be suitable for tumor hyperthermia therapy, specifically NPs of $Co_{0.9}Gd_{0.1}Fe_2O_4$ due to their high ability to lose energy [71]. Almessiere *et al.* [166] reported the anticancer properties of Nd^{3+} and Ce^{3+}-substituted cubic $CoFe_2O_4$ against human colon cancer cells (HCT-116) *via* MTT ((3-(4,5-dimethylthiazol-2-yl)-2,5-diphenyltetrazolium bromide) assay. After 48 h of treatment with Nd^{3+} and Ce^{3+}, the substituted $CoFe_2O_4$ samples displayed apoptosis of HCT-116 cells. These results showed that Ce–Nd-substituted nano Co-ferrite had anticancer efficiency against colon cancer.

Zhang *et al.* [167] used leucine-coated cobalt ferrite ($CoFe_2O_4$) NPs in drug delivery with a DOX loading capacity of 0.32 mg/mg; the loaded DOX displayed a progressive and sustained release. The MTT assay was used to determine the cytotoxicity on HeLa cells, and the results showed that the Leu-coated $CoFe_2O_4$ NPs demonstrated comparatively minimum cytotoxicity compared with that of $CoFe_2O_4$ NPs, and the DOX-loaded Leu-coated $CoFe_2O_4$ NPs showed an observable cell death for HeLa cells. Iqbal *et al.* [168] have reported that cobalt ferrite doped with zinc ($Zn_{0.5}Co_{0.5}Fe_2O_4$) NPs produced by a novel, simple sol–gel method, resulted in good magnetic amorphous NPs. Neutral red assay (NRA) was used to test the anticancer activity on HepG2 cell lines. The results revealed that 250 μg/mL $Zn_{0.5}Co_{0.5}Fe_2O_4$ incubated with HepG2 cell lines at 80 J/cm^2 laser fluence resulted in the cell viability loss of about 60–65%. The incubation time increased with increasing the absorbance for $Zn_{0.5}Co_{0.5}Fe_2O_4$ NPs (250 μg/mL), which was examined at incubation times 3, 24, and 49 h; the absorbance reached 0.40, 0.51, and 0.65 a.u., respectively. Different studies reported that ferrites have an anticancer cytotoxic effect against malignant cell models in the absence of light/laser [169,170]. Also, they revealed that the cell viability loss significantly differed pre and post laser irradiation, even after post cells exposure to 400 μg of $Zn_{0.5}Co_{0.5}Fe_2O_4$ NPs. The cell inhibition was significantly higher (44%) at a laser fluence of 80 J/cm^2 than in dark cell inhibition (18%).

McBain *et al.* [171] reported that $CoFe_2O_4$ NPs were promising as drug delivery nanocarriers. Cai *et al.* [172] reported three potential properties: high effective drug loading; surface area; and varied multifunctional nanocomposites due to feasibility and magnetically targeted controlled through an external magnetic field. The DOX delivery and release were controlled by magnetically driven dandelion pollen-like $CoFe_2O_4$ nanostructures. They also revealed a loading capacity of 88.6% of the nanostructure, a loading content of 118 mg of DOX/g of $CoFe_2O_4$ microspheres, and drug release of ~55% under an AMF field at 8 h [173].

Liu *et al.* [174] reported magnetic affinity and designed mesoporous silica nanotube worm-like with settled $CoFe_2O_4$ NPs over the surface that triggered the nanotubes magnetically in biological fluids. They also studied the release-uptake process by using 6-carboxyfluorescein as a drug delivery model *in vitro* using HeLa cells. The cargo was released within 1 h into HeLa cells, after AMF (0.5 mT, 100 Hz) of the nanotubes.

Iatridi *et al.* [175] prepared a mixture of $MnFe_2O_4$ and $CoFe_2O_4$ coated with poly(sodium methacrylate)-*co*-(dodecylmethacrylate-*co*-2,4-diphenyl)-6-(4-vinyl-phenyl quinoline)-*g*-poly(*N*,*N*-dimethylacrylamide-*co*-*N*-isopropylacrylamide) (P(MANa-*co*-DMA-*co*-SDPQ))-*g*-(*P*-(DMAM-*co*-NIPAM)). It was applied in hyperthermia cancer therapy. Also, Iatridi's group evaluated the hyperthermic activity of colloidal NPs by exposure to a field of kHz and 250 Oe, which was heated to 44°C within 10 min. It was found that NPs were suitable for luminescence and MR imaging and pH and temperature-controlled drug release along with hyperthermia cancer therapy.

Yang *et al.* [176] revealed that the $CoFe_2O_4$ core and polydopamine and zeolitic imidazolate framework shell ($CoFe_2O_4$@PDA@ZIF-8) were used to encapsulate CPT in the ZIF-8 shell and DOX in the $CoFe_2O_4$ core where the photothermal NP activity was stimulated by both ZIF-8 and polydopamine. Also, they found that the loading capacities of NPs were 98 and 46% for DOX and CPT, respectively, which were released at pH 5 during 7 h by 75 and 45%, respectively, post 5 min laser irradiation. It was shown that the nanocarrier was heated to 65°C after 10 min exposure to 808 nm laser. Therefore, $CoFe_2O_4$ NPs have shown potential results in hyperthermia, diagnosis, and cancer therapy [177].

Magnetite Fe_3O_4 is one of the oldest and yet one of the most commonly used SFNPs with a unique inverse spinel structure [178]. Fe_3O_4 NPs were used as therapeutic hyperthermia cancer agents and magnetic-guided drug delivery [178,179] agents. Fe_3O_4 NPs reached the highest and the lowest hyperthermia by doped Mn^{2+} and Zn^{2+}, respectively [180,181]. Two types of anticancer drugs, curcumin (Cur) loaded and synthesized SF nanocomposites (SFNCs), were synthesized by using Fe_3O_4 NPs as the core; one of them (Fe_3O_4/OCMCS/Cur) was Cur, burdened, and encapsulated with O-carboxy methylchitosan (OCMCS), and another one, (Fe_3O_4/OCMCS/Cur/Fol) was folate attached to Fe_3O_4/OCMCS/Cur [182].

The bio-distribution and the effectiveness of SFNCs were investigated by injecting at a dose of 20 μg/kg SFNCs into mice bearing solid tumor Sarcoma-180. The results have shown that Fe_3O_4/OCMCS/Cur/Fol was distributed uniformly after 5 h than Fe_3O_4/OCMCS/Cur. It was proved that SFNC was a good curcumin loader in, as well as, cancer-targeted drug delivery; SNFC also showed a synergic action of hyperthermia and chemotherapeutic [183]. It was revealed that CS-based magnetic hybrid NCs with folate-conjugated tetrapeptide composite (CS, CdTe quantum dots QDs (a fluorescent dye), and SPM Fe_3O_4, camptothecin CPT cytotoxic drug, folate and tetrapeptides) [184].

Manganese ferrite ($MnFe_2O_4$) is used for drug delivery and as an enhancer for hyperthermia to increase anticancer efficiency [185]. Five SFNPs were synthesized with a combination of core–shell components or exchanging the order of coating for power loss as follows $CoFe_2O_4$@Fe_3O_4 < $CoFe_2O_4$@$MnFe_2O_4$ < Fe_3O_4@$CoFe_2O_4$ < $MnFe_2O_4$@$CoFe_2O_4$ < ($Zn_{0.4}Co_{0.6}$) Fe_2O_4@$Zn_{0.4}Mn_{0.6}Fe_2O_4$. Lee *et al.* [185] revealed that the heat efficacy of hyperthermia cancer therapy was enhanced by coupling exchange between a soft shell and a magnetically hard core.

The supermagnetic DOX poly(lactic-*co*-glycolic acid) (PLGA)@CS-stabilized (CS)@$Mn_{0.9}Zn_{0.1}Fe_2O_4$ NPs was synthesized with low M_s = 13.2 emu/g as compared to $Mn_{0.9}Zn_{0.1}Fe_2O_4$NPs (M_s = 56.1) that led to efficient magnetic response during the drug release, which was adjusted by the pH of cancer cells. The DOX-PLGA@CS@$Mn_{0.9}Zn_{0.1}Fe_2O_4$NPs revealed drug loading, delivery, and hyperthermic cancer therapeutic effect [186].

Wang *et al.* [187] synthesized $MnFe_2O_4$@GO NC *via* the sonochemical method within high DOX loading capacity due to π–π interactions and hydrogen bonding between DOX and GO. Hence, the $MnFe_2O_4$@GO delivered targeted drug delivery for DOX to cancer cells, and DOX was released due to the acidic tumor microenvironment. Slimani *et al.* [188] found that HCT-116 growth was significantly inhibited by lanthanide/dysprosium (Ce^{3+}/Dy^{3+}) co-activated co-doped manganese-zinc nanospinel ferrites (CDMZNSFs) (with IC50 values ranging from 0.74 to 2.35 mg/mL for 48 h), whereas the healthy HEK-293 cell growth was not damaged.

Hekmat and Saboury [189] revealed that the antiproliferative and anticancer effects of $Co_{0.3}Mn_{0.2}Zn_{0.5}Fe_2O_4$ NPs were determined by MTT assay after the T47D cell line was treated with 6–300 nM $Co_{0.3}Mn_{0.2}Zn_{0.5}Fe_2O_4$ NPs 48 h. Also, Hekmat and Saboury found that the IC50 of $Co_{0.3}Mn_{0.2}Zn_{0.5}Fe_2O_4$ NPs on the T47D cell line was equal to 70 nM. It was found that $Co_{0.3}Mn_{0.2}Zn_{0.5}Fe_2O_4$ NPs were a potential anticancer–antiproliferative agent. Further, Hekmat and Saboury studied the morphological of cancer cells by treating T47D (1×10^5 cells per well) with 70 nM $Co_{0.3}Mn_{0.2}Zn_{0.5}Fe_2O_4$ NPs and 1 mg/mL DAPI solution. It is known that DPAI binds to DNA resulting in increased fluorescence by 20-fold based on the displacement of H_2O from the minor groove of DNA and DAPI. Furthermore, Hekmat and Saboury showed that the living cells showed regular blue, while the dead cells that were treated with $Co_{0.3}Mn_{0.2}Zn_{0.5}Fe_2O_4$ NPs (70 nM) were bright blue doted nuclei, which indicated DNA fragmentation of nuclei and confirmed the previous MTT results [190].

Hekmat *et al.* found out that flow cytometry was a sensitive and fast apoptotic assay, and could easily differentiate between apoptotic and necrotic cells [98]. Hekmat and Saboury [189] studied the apoptosis after exposure of T47D (1×10^6 cells/well) at 70 nM $Co_{0.3}Mn_{0.2}Zn_{0.5}Fe_2O_4$ NPs (24 h) by Annexin V and then evaluated by flow cytometry. It was revealed that the NPs reduced the viable cells and increased the apoptotic cells.

Nickel ferrite $NiFe_2O_4$ NPs were found to be a potent differentiated hyperthermia agent for cancer therapy [191]. The new nanoformulation β-cyclodextrin-dextran layered on NF NPs ($Ni_{1.04}Fe_{1.96}O_4$) was synthesized in about 6 nm. It was found that camptothecin CPT was loaded by 88% in the polymer-coated NPs. Moreover, the nanocarrier sustained the CPT release profile; on the other hand, a decrease in pH by 1.4 leads to faster release of CPT. The CPT-loaded β-cyclodextrin-dextran coated on magnetic nickel ferrite nanocomposite displays cell growth inhibition of HeLa human cervical, breast MDA-MB-231, and lung A549 cancer cell lines with cytotoxicity IC50 values of 1.49, 1.35, and 1.41 μg/mL, respectively. It was found that the anticancer efficacy of CPT-loaded CD-Dx MNP nanoformulation was greater than 5-fluorouracil and *cis*-platin against different cancer cell lines [191].

Alahmari *et al.* [192] synthesized $Ni_{0.5}Co_{0.5-x}Cd_x$-$Fe_{1.78}Nd_{0.02}O_4$ ($x \leq 0.25$) nanofibers (NFs). They evaluated the cytotoxic anticancer effect of NFs by MTT assay on HEK-293 and HCT-116 cells [193,194]. The cells were treated with a range of dosages from 2 to 25 μg/mL for 48 h. They found that NFs profound a significant cell growth inhibition in HCT-116 cancer cells but not in HEK-293. Finally, they concluded that NFs were highly specific and targeted to colon cancer cells.

Tombuloglu *et al.* [195] revealed that synthesized nanocomposites showed promising results for drug delivery and cancer therapy. They synthesized $Co_{0.5}Ni_{0.5}Nb_xFe_{2-x}O_4$ by the hydrothermal combination of Co, Ni, Nb, and Fe_2O_4. They examined the effect of the prepared nanocomposite by incubating different concentrations (0.3, 1.5, 3.8, 6.1, and 12.2 mg/mL) at 48 h with HCT-116 and HEK-293 using MTT

assay and stained with DAPI (microscopic). The prepared nanocomposites led to a dose-dependent decrease in the proliferation and viability of cancer cells. The 0.3 mg/mL dose of the nanocomposite resulted in 98.2, 95.2, 93.2, 92.2, 91.2, and 90.2% cell viability *versus* Nb(x) of 0.00, 0.02, 0.04, 0.06, 0.08, and 0.1, respectively; while 1.52 mg/mL MNP led to decreased 68.0, 59.9, 59.1, 56.9, 57.6, and 56.5% cell viability. The 3.85 mg/mL dose of the nanocomposite repressed cell viability to 66.2, 59.1 58.5, 55.9, 57.9, and 55.9%, respectively. Increasing the nanocomposites concentration to 6.1 and 12.2 mg/mL led to decrease in cell viability (65.3, 58.1, 57.7, 54.7, 55.7, and 54.7%;and 64.3, 57.9, 57.0, 54.0, 54.0, and 54.0%), respectively. It was found that the use of $Co_{0.5}Ni_{0.5}Nb_xFe_{2-x}O_4$ did not cause cytotoxicity on HEK-293 cells [195].

Zinc ferrite ($ZnFe_2O_4$) has been used as an essential radiosensitizer in human prostate tumor radiotherapy (RT) [164]. It was reported that 100 μg/mL $ZnFe_2O_4$ enhanced the γ-irradiation efficiency 17 times greater than only γ-irradiation *via* 53% cancer cell growth inhibition. Gamma irradiation induces a dose-dependent alteration of structural integrity [196–200]. Also, gamma irradiation offers advantages in economy and convenience over autoclaving and has been used in sterilization and preparation of different materials [201–205]. The SPM NPs synthesized should possess high Ms and small particle size to be suitable and safe for cancer patients during hyperthermia [101,102,108] and RT [33]. The enhancement of hyperthermia cancer therapy by manganese-doped zinc SFNP ($Zn_{0.4}Mn_{0.6}$) Fe_2O_4 was due to their high values of M_s (175 emu/g) and specific loss power [206]. Almessiere *et al.* [129] synthesized DyY-MnZn NSFs by ultrasonic irradiation and citrate sol–gel combustion methods; a chain of $Mn_{0.5}Zn_{0.5}Fe_{2-2x}(Dy_xY_x)O_4$ ($0.0 \leq x \leq 0.05$) was formed. They found out that the pure phase of SF was produced by ultrasonic irradiation, while a mixture of hematite and SFs was produced by the citrate sol–gel method. It was also shown that both the mixture or pure DyY-MnZn NSFs inhibited cell growth of the colon cancer cell line (HCT-116), but did not inhibit the healthy cell line growth (HEK-293). The ultrasonicated DyY-MnZn NSFs were better than the sol–gel DyY-MnZn NSFs in inhibition of HCT-116 cell growth.

Al-Qubaisi *et al.* [207] studied the cytotoxicity of NiZn ferrite NPs against HT29 (human colon cancer), MCF7 (Michigan Cancer Foundation7; breast cancer), and HepG2 (liver cancer) cells by MTT assay. The NiZn ferrite NPs were used in different concentrations (15.6–1,000 μg/mL; 72 h) and the cancer cell growth inhibition showed a dose-dependent behavior. The DNA fragmentation and caspase-3 and -9 activities were assayed to confirm the apoptotic effect of NiZn ferrite NPs on different cancer cell lines. The cytotoxic effects of HT29 or MCF7 cells were less sensitive than that of HepG2 to NiZn ferrite NPs (72 h). Also, Al-Qubaisi *et al.* reported considerable morphological variations in MCF7, HT29 and HepG2 cells after incubation with NiZn ferrite NPs (72 h). More apparent morphological changes (membrane blebbing, cytoplasmic shrinking, cells dispersion, and cell shrinking) were found in HepG2 than the other cell lines. Besides, Al-Qubaisi *et al.* revealed that NiZn ferrite NPs selectively killed HepG2 cells *via* induction of apoptosis and suppression of proliferation. The apoptotic effect of NiZn ferrite NPs in cancer cells was due to to the significant activation of caspase-3 and caspase-9, which was responsible for the induction of DNA fragmentation in HT29, MCF7, and HepG2 cell lines.

Lartigue *et al.* [208] presented that cells treated with NiZn ferrite NPs induced apoptosis and were associated with morphological changes. The magnetic NiZn ferrite NPs were speedily dispersed in epithelial tissues that were firmly bound to albumin. Mitamura *et al.* [209] revealed that the potential candidate in apoptosis was the activated endogenous nuclease enzymes, which led to DNA fragmentation and was mediated by caspase-3 as a nuclease activator. Al-Qubaisi *et al.* [207] found that NiZn ferrite NPs induced apoptosis in cancer cells with the highest effective dose of ~100 μg/mL in HepG2 cells and 1,000 μg/mL for HT29 and MCF7 cells after 12 h. Ahamed *et al.* [210] reported that nickel ferrite NPs induced apoptosis in the human alveolar adenocarcinoma A549 cell line at 100 μg/mL. Hathaway *et al.* [211] found that the magnetic NPs had two essential characteristics as an effective anticancer drug, cancer specificity, and minimum cytotoxicity to normal cells. In conclusion, Ni–Zn ferrite had potential apoptotic anticancer activity against cancer cells.

Sarala *et al.* [212] revealed that $ZnFe_2O_4$ NPs were synthesized with *Lawsonia inermis* leaf extract as a surfactant by the green method. The MTT method was used to detect mitochondria's cell activity and that reflected the viable cells [213]. The ferrite NPs induced cytotoxicity by the generation of ROS. ROS such as superoxide anions, hydroxyl radicals, hydrogen peroxide, and alkoxy radicals denatured biological macromolecules (DNA, carbohydrates, proteins, lipids, *etc.*). MTT assay was used to determine the anticancer effect of $ZnFe_2O_4$ NPs; MCF-7 cells were incubated with 25, 50, 100, 250, and 300 μg per well $ZnFe_2O_4$ NPs for 24 h. The cell viability decreased by 60, 53, 44, 32, and 24%, respectively.

The cytotoxicity mechanism of $ZnFe_2O_4$ NPs based on ROS generation due to intracellular Zn^{2+} resulted in

cellular redox machinery failure [214]. ROS enhanced mitochondrial respiration and apoptosis in mitochondria, cellular redox disequilibrium, and lipid peroxidation in the cell membranes [215]. The direct interaction of $ZnFe_2O_4$ NPs with cell walls led to the damage and denaturation of the membrane. ROS generated on the surface of the $ZnFe_2O_4$ NPs and particle disbanding and free Zn^{2+} ions release resulted in the ROS production within the cells [212].

Magnesium ferrite $MgFe_2O_4$ NPs were selected due to their easy breakdown in the human body and their application in biomedical fields, such as biocompatibility, magnetic hyperthermia therapy, as a contrasting agent in MRI, and drug delivery [216–218]. Selvam *et al.* [219] revealed the cytotoxicity on the healthy human embryonic kidney cell line (HEK293) for poly(vinyl alcohol) cross-linked β-cyclodextrin polymer coating of magnesium ferrite NPs (PVA-CD-MNPs) and camptothecin-loaded PVA-CD-MNP nanocomposite (PVA-CDMNPs@ CPT), where IC_{50} values were found to be 18.96 and 5.104 μg/mL, respectively. The anticancer efficacy was studied on colorectal cancer HCT-15 cell lines, and the IC50 values were 28.89 and 66.17 μg/mL for PVA-CD-MNPs@CPT and the PVA-CD-MNPs, respectively. The HEK 293 cells are more sensitive to PVA-CDMNPs@ CPT. Together with the host polymer, the magnetic NPs combined with an excellent antineoplastic nanocomposite when loaded with the topoisomerase inhibitor (camptothecin), a promising drug delivery vehicle for cancer therapy. The nanocomposite vehicle accommodated any drug of suitable size that fits into the cyclodextrin cavity. It does not rely upon the open-on covalent linking of the drug to the polymer through complex methods of synthesis and the requirement to cleave the drug-polymer bond at the target site for drug release. Therefore, the nanoformulation vehicle can be loaded and released by any anticancer drug.

RT was considered to be one of the effective cancer therapy methods [220]. Furthermore, the efficacy of the RT therapeutic effect can be enhanced by NPs [216]. The anticancer therapeutic effect of magnesium ferrite NPs $MgFe_2O_4$ on the human breast cancer cell line MCF-7 [216–218] was investigated. Meidanchi and Motamed [221] revealed that $MgFe_2O_4$ was successfully synthesized in a single-step reaction hydrothermally with an average particle size of 10.5 nm and sample crystallite size of 9 nm. The SPM $MgFe_2O_4$ behavior was revealed at room temperature. Additionally, the $MgFe_2O_4$ as X-ray irradiation radiosensitizers was applied in MCF-7 RT. It was found that (a) the concentration of $MgFe_2O_4$ up to 10 μg/mL had no significant cytotoxicity on MCF-7 and cytotoxicity was evident only at 100 μg/mL; and (b) significant cell damage was found in the presence of 10 μg/mL $MgFe_2O_4$ concentration under 2 and 4 Gy X-ray irradiation. Therefore, no significant cytotoxicity and significant cell damage were observed at 10 μg/mL $MgFe_2O_4$, indicating that $MgFe_2O_4$ could be used as a radiosensitizer for cancer cell therapy in comparison with RT alone. $MgFe_2O_4$ was considered as a radiosensitizer due to the production of Auger low-energy electrons due to its photoelectric effect under X-ray irradiation.

Copper ferrite $CuFe_2O_4$ NPs and their composites are also used in cancer therapy. Jermy *et al.* [3] investigated the anticancer cytotoxic effect of CS enclosed $CuFe_2O_4$/HYPS. Cell inhibition was detected by MTT assay. They studied CS over spherical hydrophilic silica (HYPS) NPs at two concentrations (0.06 and 0.6) wt% and varied pH values (5, 6, and 6.5). Also, they used the impregnation method for the synthesis of four nanocomposites of SF/silica. It was found out that their magnetization order was $CoFe_2O_4$/HYPS (14.15 emu/g) > $NiFe_2O_4$/HYPS (7.73 emu/g) ~ $CuFe_2O_4$/HYPS (7.65 emu/g) > $MnFe_2O_4$/HYPS (1.49 emu/g).

The SPM effect was observed in $MnFe_2O_4$/HYPS, whereas the ferromagnetic effect was observed in $CoFe_2O_4$/HYPS. Both Cu Fe_2O_4/HYPS and Ni Fe_2O_4/HYPS presented similar paramagnetic effects. Jermy *et al.* revealed a physicochemical method (method I) for 6–12 nm $CuFe_2O_4$, CS, and *cis*-Pt over HYPS. It was verified that CS was essential for the restricted release of *cis*platin (*cis*-Pt) over $CuFe_2O_4$/HYPS by pH adjustment of CS (method I). In the same context, they proved that nanoformulation of *cis*-Pt/$CuFe_2O_4$/HYPS/CS (method I) had an insignificant cell viability effect. However, the CS/$CuFe_2O_4$/HYPS/*cis*-Pt nanocomposite synthesized *via* the impregnation method (method II) by CS prewrapping and preloading *cis*-pt(0.15 mmol/g *cis*-pt) . Also, they showed that 64% *cis*-pt was released during 72 h from the nanocomposite and had a significant cytotoxic effect. Jermy *et al.* studied the cell viability of CS/$CuFe_2O_4$/HYPS/*cis*-Pt on the healthy human embryonic kidney (HEK293) and MCF-7 cells. Besides, they found that $CuFe_2O_4$/HYPS was noncytotoxic, and *cis*-Pt, *cis*-Pt/$CuFe_2O_4$/HYPS, and CS/$CuFe_2O_4$/HYPS/*cis*-Pt significantly induced cell inhibition in both HEK293 and MCF7 dose-dependently. The MCF7 cell viability at the lowest concentration was as follows: *cis*-Pt, 58.17%; *cis*-Pt/$CuFe_2O_4$/HYPS, 63.36%; and CS/$CuFe_2O_4$/HYPS/*cis*-Pt, 70.73%. However HEK293 cell viability was 73.47% for *cis*-Pt, 80.24% for *cis*-Pt/$CuFe_2O_4$/HYPS, and 95.07% for CS/$CuFe_2O_4$/HYPS/*cis*-Pt. Finally, Jermy *et al.* showed that CS/$CuFe_2O_4$/HYPS/*cis*-Pt method II was the best nanoformulation due to the biocompatibility advantage of CS, avoiding the premature *cis*-pt release during the pH adsorption of CS (Figure 27) and effectively targeted tumor cells

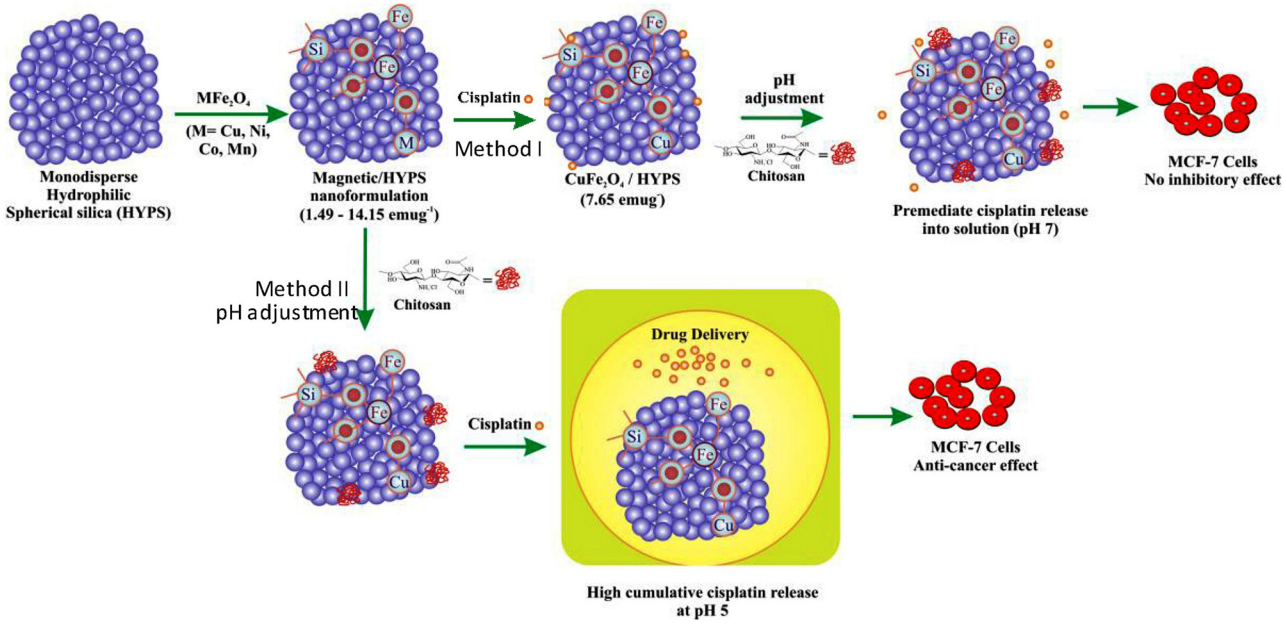

Figure 27: The CS/CuFe2O4/HYPS/*cis*-Pt nanocomposite optimized route. Adapted from ref. [3] with permission from Elsevier™.

with a similar pure *cis*-pt efficiency; thus making it a novel magnetically targeted drug delivery system.

Meidanchi [222] used the hydrothermal process in the synthesis of $Mg_{(1-x)}Cu_xFe_2O_4$ SPMNPs ($0.2 \leq x \leq 0.8$). Meidanchi studied the anticancer effect (MTT assay) of $Mg_{1-x}Cu_xFe_2O_4$ SPMNPs at various concentrations (0.1, 1, 10, and 100 µg/mL) on the MCF-7 cell line before and after 2 Gy X-ray RT. Also, Meidanchi showed that X-ray irradiation at a high concentration of Cu and $Mg_{(1-x)}Cu_xFe_2O_4$ SPMNPs resulted in significant inhibition of the growth of MCF-7 cells. However, nonsignificant cell growth inhibition of $Mg_{(1-x)}Cu_xFe_2O_4$ SPMNPs was observed at lower concentrations (0.1–10 µg/mL). Further, Meidanchi concluded that $Mg_{(1-x)}Cu_xFe_2O_4$ SPMNPs (x = 0.2 (10 µg/mL) and x = 0.6 (1 µg/mL)) was considered as a nano-radiosensitizer due to synergistic therapeutic effect without cytotoxicity on the MCF-7 cells.

6 Challenges and perspectives

Diverse properties of SFNPs, such as the shape, size, charge of the surface, and surface adjustment, should be identified when composites-incorporated SFNPs were formed to reduce the elimination of SFNPs from circulation and maximize their influence on the targeted tissues. The size of the composites-incorporatedSFNPs is significant for controlling the rate of their internalization through target cells and magnetic properties. The suitable size range was reported to be in the range of 10-100 nm to allow them to pass through tiny capillaries and restrict SFNPs' elimination from circulation. The decrease in the size is of importance due to the tendency to aggregate. The second significant factor was the surface charge or zeta potential of SFNPs incorporated with composites. The best zeta potential was found between 10 and 30 mV or between –10 and –30 mV to obtain a stable suspension of SFNPs with minimum aggregation. The surface charge of the SFNPs was influenced by surface modification. The incorporation of composites on the SFNP surface led to a decrease in their magnetization, resulting in weak magnetic targeting. So, thickness and type of material incorporated significantly impact variations in the magnetic characteristics of SFNPs. Consequently, the beneficial characteristics of magnetic composites for drug delivery would be traded off with the increase in the particle size and the decreased magnetic properties. In contrast to hyperthermic applications where heat damage was initiated *via* exposing diseased tissues to high temperatures for a period of time, controlled heating (4–10°C) in short periods of time is in demand in drug delivery purposes *via* the heat-responsive polymer-incorporated SFNPs. This is a challenging problem because if the polymer is subjected to any excessive heating, its structure can be degraded, and hence, its reversible phase transition may be destroyed. Overall, complex synthesis methods are usually needed

for the successful configuration and purpose of nanomaterials [82,83,205,223–225], and remarkable unclear aspects concerning their magnetic response are still lingering.

7 Bibliometric mapping analysis

Search methodology for bibliometric mapping: (anticancer SF OR drug delivery SF or cancer therapy SF) OR TOPIC: (anticancer Manganese ferrite) OR TOPIC: (anticancer Nickel ferrite) OR TOPIC: (anticancer Zinc ferrite) OR TOPIC: (anticancer Magnesium ferrite) OR TOPIC: (anticancer Copper ferrite) OR TOPIC: (anticancer Lithium ferrite) OR TOPIC: ("anticancer NPs") OR TOPIC: (drug delivery Manganese ferrite) OR TOPIC: (drug delivery Nickel ferrite) OR TOPIC: (drug delivery Zinc ferrite) AND TOPIC: (drug delivery Magnesium ferrite) AND TOPIC: (drug delivery Copper ferrite) AND TOPIC: (drug delivery Lithium ferrite) OR TOPIC: (hyperthermia SF)

Timespan: All years. Indexes: SCI-EXPANDED, SSCI, A&HCI, CPCI-S, CPCI-SSH, ESCI.

The bibliometric mapping analysis is shown in with the network visualization and density visualization, respectively. The bibliometric mapping analysis showed 402 results using the search methodology mentioned above from the Web of Science (WOS). There is a strong relationship in the literature between hyperthermia and iron oxide NPs and different types of SF NPs, as shown in Figure 28. Many investigation studies in the literature on parameters are linked to the hyperthermia phenomenon such as the temperature, particle size, cation distribution, and facile synthesis methods. The hyperthermia phenomenon also showed large co-occurrence with anticancer NPs and drug delivery for magnetic materials and SF. On the other hand, Figure 28 shows a significant gap in the literature regarding *in vivo*, photothermal therapy, heating efficiency, toxicity, theranostics, and controlled release. Figure 29 shows prominent keywords in this field as shown from the density visualization map such as magnetic properties, hyperthermia, NP size, and drug delivery.

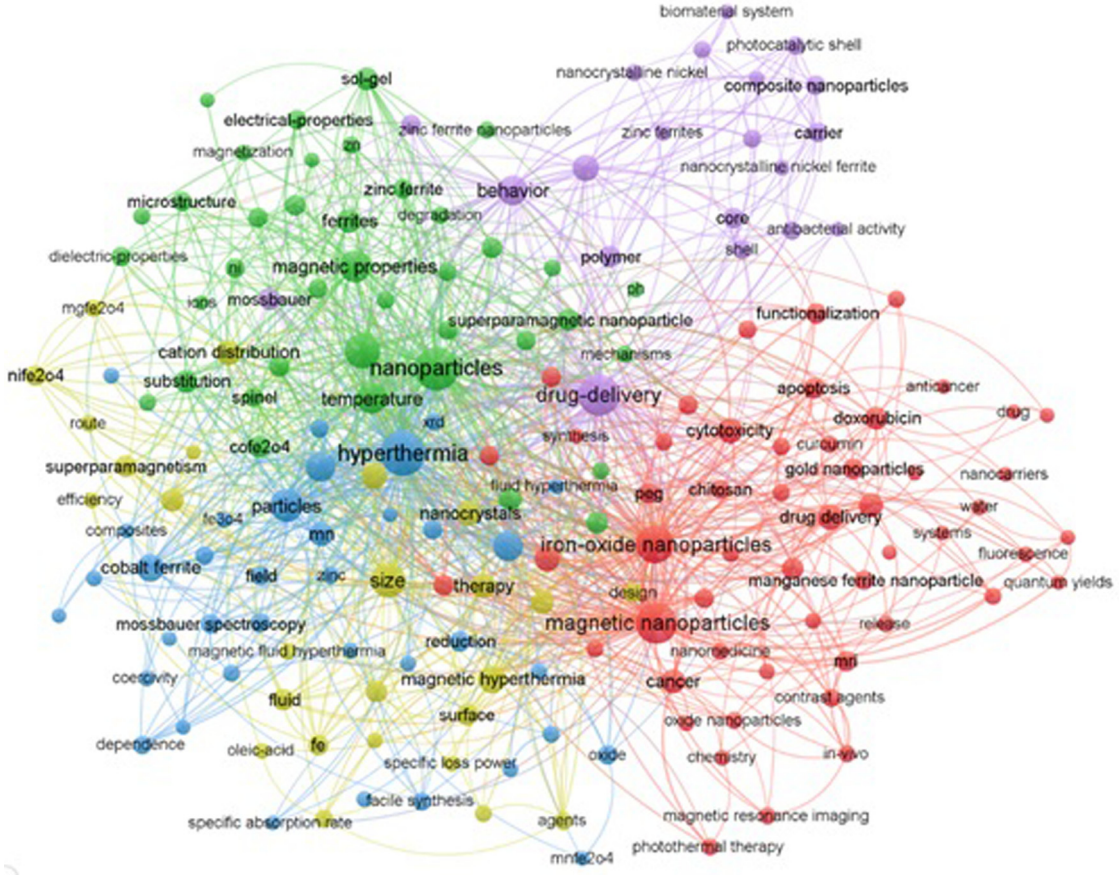

Figure 28: The bibliometric network mapping of SF NPs as anticancer and drug delivery research field in all years in WOS.

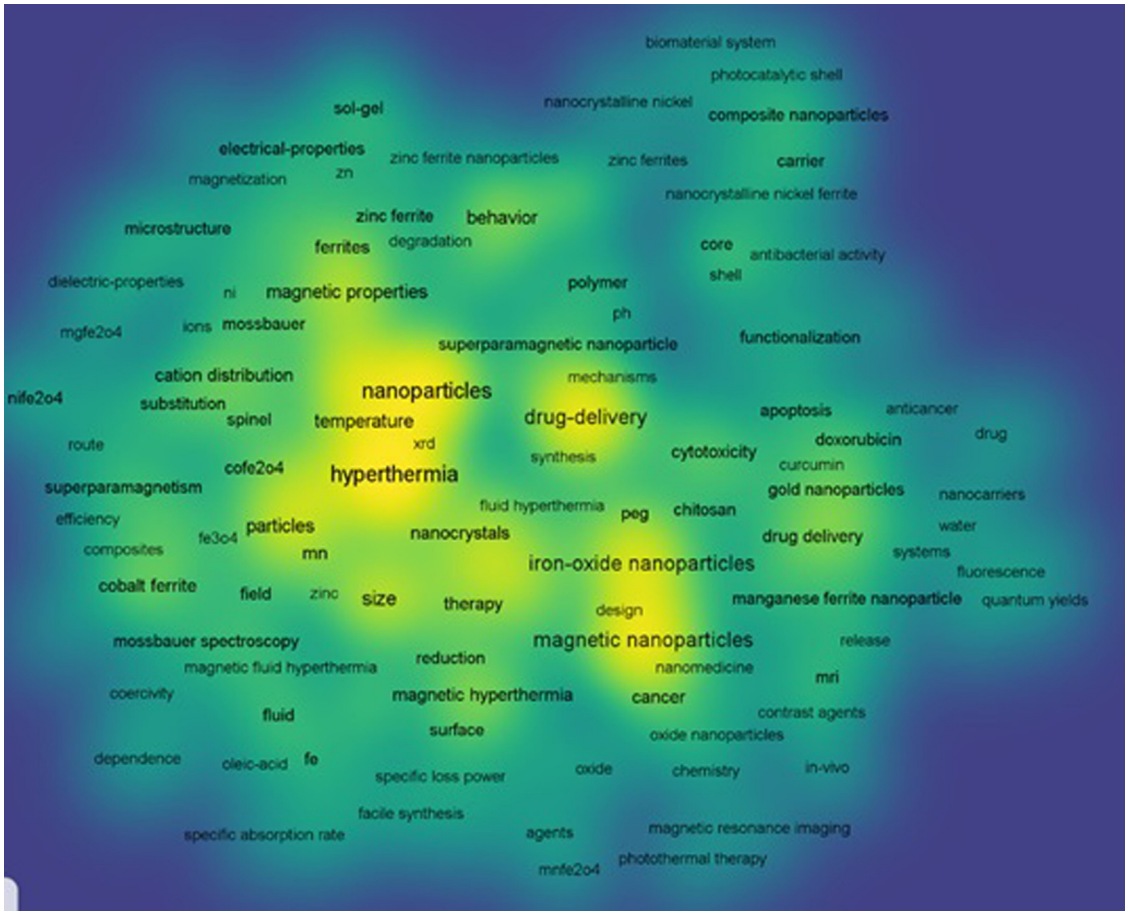

Figure 29: The bibliometric density visualization mapping of SF NPs as anticancer and drug delivery research field in all years in WOS.

8 Conclusion

One of the essential applications of SF NP SFNPs is cancer therapy, hyperthermia, drug targeted delivery, and release. In this review, the synthesis methods used to prepare SFNPs are presented in detail. Also, the structural and magnetic properties of SFNPs are discussed. Further, the relation between the surface morphology and different properties of SFNPs is revealed. The unique physicochemical characteristics of SF include low toxicity and high biocompatibility for use in various biomedical applications, including drug delivery and magnetic hyperthermia treatment. The frequency and amplitude of the applied external magnetic field, and NP sizes are the main factors for safe hyperthermia cancer therapy. The anticancer efficiency of SFNPs depends upon their synthesis and cytotoxicity methodology, which was evaluated by MTT assay on normal cell lines and different cancer cell lines. The results showed acceptable cell viability on normal cell lines and cytotoxicity and cancer cell growth inhibition. Generally, the surface of SFNPs coated with nontoxic chemicals enhanced cell viability and biocompatibility with normal cells. The hyperthermia effect of SFNPs is considered a targeted differential therapy due to cancer cells being more sensitive to the hyperthermia effect than normal cells. Cancer cells were damaged by the heat generated based on the external field amplitude square, frequency, size, and type of SFNPs. It is known that the conservative drug delivery suffered from unstable metabolic tissue distribution and was nontargeted to cancer cells, which leads to a decrease in cancer therapy efficiency and increased whole-body toxicity. On the other hand, cytotoxic drugs were efficiently delivered by encapsulating within polymer-SFNPs composite.

Funding information: The authors state no funding involved.

Author contributions: All authors have accepted responsibility for the entire content of this manuscript and approved its submission.

Conflict of interest: The authors state no conflict of interest.

References

[1] Feng Q, Tong R. Anticancer nanoparticulate polymer-drug conjugate. Bioeng Transl Med. 2016;1(3):277–96.

[2] Bray F, Ferlay J, Soerjomataram I, Siegel RL, Torre LA, Jemal A. Global cancer statistics 2018: GLOBOCAN estimates of incidence and mortality worldwide for 36 cancers in 185 countries. CA: a Cancer J Clinicians. 2018;68(6):394–424.

[3] Jermy R, Ravinayagam V, Alamoudi W, Almohazey D, Elanthikkal S, Dafalla H, et al. Tuning pH sensitive chitosan and *cis*platin over spinel ferrite/silica nanocomposite for anticancer activity in MCF-7 cell line. J Drug Delivery Sci Technol. 2020;57:101711.

[4] Pon-On W, Tithito T, Maneeprakorn W, Phenrat T, Tang IM. Investigation of magnetic silica with thermoresponsive chitosan coating for drug controlled release and magnetic hyperthermia application. Mater Sci Eng C. 2019;97:23–30.

[5] Angelova A, Garamus VM, Angelov B, Tian Z, Li Y, Zou A. Advances in structural design of lipid-based nanoparticle carriers for delivery of macromolecular drugs, phytochemicals and anti-tumor agents. Adv Colloid Interface Sci. 2017;249:331–45.

[6] Singh TA, Das J, Sil PC. Zinc oxide nanoparticles: a comprehensive review on its synthesis, anticancer and drug delivery applications as well as health risks. Adv Colloid Interface Sci. 2020;286:102317.

[7] Mohapatra S, Rout SR, Maiti S, Maiti TK, Panda AB. Monodisperse mesoporous cobalt ferrite nanoparticles: synthesis and application in targeted delivery of antitumor drugs. J Mater Chem. 2011;21(25):9185–93.

[8] Algarou NA, Slimani Y, Almessiere MA, Rehman S, Younas M, Unal B, et al. Developing the magnetic, dielectric and anticandidal characteristics of $SrFe_{12}O_{19}$/$(Mg_{0.5}Cd_{0.5}Dy_{0.03}Fe_{1.97}O_4)_x$ hard/soft ferrite nanocomposites. J Taiwan Inst Chem Eng. 2020;113:344–62.

[9] Amiri M, Salavati-Niasari M, Akbari A. Magnetic nanocarriers: evolution of spinel ferrites for medical applications. Adv Colloid Interface Sci. 2019;265:29–44.

[10] Wu W, Wu Z, Yu T, Jiang C, Kim W-S. Recent progress on magnetic iron oxide nanoparticles: synthesis, surface functional strategies and biomedical applications. Sci Technol Adv Mater. 2015;16(2):23501.

[11] Obaidat IM, Issa B, Haik Y. Magnetic properties of magnetic nanoparticles for efficient hyperthermia. Nanomaterials. 2015;5(1):63–89.

[12] Meidanchi A, Akhavan O, Khoei S, Shokri AA, Hajikarimi Z, Khansari N. $ZnFe_2O_4$ nanoparticles as radiosensitizers in radiotherapy of human prostate cancer cells. Mater Sci Eng C. 2015;46:394–9.

[13] Spirou SV, Basini M, Lascialfari A, Sangregorio C, Innocenti C. Magnetic hyperthermia and radiation therapy: radiobiological principles and current practice. Nanomaterials (Basel, Switzerland). 2018;8(6):401.

[14] Sohn C-H, Park SP, Choi SH, Park S-H, Kim S, Xu L, et al. MRI molecular imaging using GLUT1 antibody-Fe_3O_4 nanoparticles in the hemangioma animal model for differentiating infantile hemangioma from vascular malformation. Nanomed Nanotechnol Biol Med. 2015;11(1):127–35.

[15] Yang M, Gao L, Liu K, Luo C, Wang Y, Yu L, et al. Characterization of $Fe_3O_4/SiO_2/Gd_2O(CO_3)_2$ core/shell/shell nanoparticles as T_1 and T_2 dual mode MRI contrast agent. Talanta. 2015;131:661–5.

[16] Lee H, Shin T-H, Cheon J, Weissleder R. Recent developments in magnetic diagnostic systems. Chem Rev. 2015;115(19):10690–724.

[17] Plouffe BD, Murthy SK, Lewis LH. Fundamentals and application of magnetic particles in cell isolation and enrichment: a review. Rep Prog Phys Phys Soc (Gt Br). 2015;78(1):16601.

[18] Ling D, Lee N, Hyeon T. Chemical synthesis and assembly of uniformly sized iron oxide nanoparticles for medical applications. Acc Chem Res. 2015;48(5):1276–85.

[19] Issa B, Obaidat IM, Albiss BA, Haik Y. Magnetic nanoparticles: surface effects and properties related to biomedicine applications. Int J Mol Sci. 2013;14(11):21266–305.

[20] Cao W, Wu R, Cao G, He Z. A comprehensive review of computer-aided diagnosis of pulmonary nodules based on computed tomography scans. IEEE Access. 2020;8:154007–23.

[21] Ma Y, Liu X. Kinetics and thermodynamics of Mg–Al disorder in $MgAl_2O_4$-spinel: a review. Molecules. 2019;24(9):1704.

[22] Ashour A, Hemeda O, Heiba Z, Al-Zahrani S. Electrical and thermal behavior of PS/ferrite composite. J Magn Magn Mater. 2014;369:260–7.

[23] Srivastava R, Yadav BC. Ferrite materials: introduction, synthesis techniques, and applications as sensors. Int J Green Nanotechnol. 2012;4(2):141–54.

[24] Arshak K, Ajina A, Egan D. Development of screen-printed polymer thick film planner transformer using Mn–Zn ferrite as core material. Microelectron J. 2001;32(2):113–6.

[25] Tsay C, Liu K, Lin T, Lin I. Microwave sintering of NiCuZn ferrites and multilayer chip inductors. J Magn Magn Mater. 2000;209(1–3):189–92.

[26] Nakamura T, Miyamoto T, Yamada Y. Complex permeability spectra of polycrystalline Li–Zn ferrite and application to EM-wave absorber. J Magn Magn Mater. 2003;256(1–3):340–7.

[27] Harasawa T, Suzuki R, Shimizu O, Olcer S, Eleftheriou E. Barium-ferrite particulate media for high-recording-density tape storage systems. IEEE Trans Magn. 2010;46(6):1894–7.

[28] Abdel Maksoud MIA, Sami NM, Hassan HS, Bekhit M, Ashour AH. Novel adsorbent based on carbon-modified zirconia/spinel ferrite nanostructures: evaluation for the removal of cobalt and europium radionuclides from aqueous solutions. J Colloid Interface Sci. 2021;607:111–124.

[29] Abdel Maksoud MIA, El-Sayyad GS, El-Bastawisy HS, Fathy RM. Antibacterial and antibiofilm activities of silver-decorated zinc ferrite nanoparticles synthesized by a gamma irradiation-coupled sol–gel method against some pathogenic bacteria from medical operating room surfaces. RSC Adv. 2021;11(45):28361–74.

[30] Abdel Maksoud MIA, El-Sayyad GS, El-Khawaga AM, Abd Elkodous M, Abokhadra A, Elsayed MA, et al. MANanostructured Mg substituted Mn–Zn ferrites: a magnetic recyclable catalyst for outstanding photocatalytic and antimicrobial potentials. J Hazard Mater. 2020;399:123000.

[31] Hassan HS, Abdel Maksoud MIA, Attia LA. Assessment of zinc ferrite nanocrystals for removal of 134Cs and 152 + 154Eu radionuclides from nitric acid solution. J Mater Sci: Mater Electron. 2020;31(2):1616–33.

[32] Verma A, Alam M, Chatterjee R, Goel T, Mendiratta R. Development of a new soft ferrite core for power applications. J Magn Magn Mater. 2006;300(2):500–5.
[33] Kefeni KK, Msagati TAM, Nkambule TTI, Mamba BB. Spinel ferrite nanoparticles and nanocomposites for biomedical applications and their toxicity. Mater Sci Eng C. 2020;107:110314.
[34] Masthoff IC, Kraken M, Mauch D, Menzel D, Munevar JA, Baggio Saitovitch E, et al. Study of the growth process of magnetic nanoparticles obtained via the non-aqueous sol–gel method. J Mater Sci. 2014;49(14):4705–14.
[35] Ashour AH, El-Batal AI, Maksoud MIAA, El-Sayyad GS, Labib S, Abdeltwab E, et al. Antimicrobial activity of metal-substituted cobalt ferrite nanoparticles synthesized by sol–gel technique. Particuology. 2018;40:141–51.
[36] Maksoud MIAA, El-Sayyad GS, Ashour AH, El-Batal AI, Elsayed MA, Gobara M, et al. Antibacterial, antibiofilm, and photocatalytic activities of metals-substituted spinel cobalt ferrite nanoparticles. Microb Pathogenesis. 2019;127:144–58.
[37] Abdel Maksoud MIA, El-Sayyad GS, Ashour AH, El-Batal AI, Abd-Elmonem MS, Hendawy HAM, et al. Synthesis and characterization of metals-substituted cobalt ferrite [Mx Co (1–x) Fe_2O_4; (M = Zn, Cu and Mn; x = 0 and 0.5)] nanoparticles as antimicrobial agents and sensors for Anagrelide determination in biological samples. Mater Sci Eng C. 2018;92:644–56.
[38] Maksoud MIAA, El-ghandour A, El-Sayyad GS, Awed AS, Fahim RA, Atta MM, et al. Tunable structures of copper substituted cobalt nanoferrites with prospective electrical and magnetic applications. J Mater Sci Mater Electron. 2019;30(5):4908–19.
[39] Abdel Maksoud MIA, El-ghandour A, El-Sayyad GS, Awed AS, Ashour AH, El-Batal AI, et al. Incorporation of Mn^{2+} into cobalt ferrite via sol–gel method: insights on induced changes in the structural, thermal, dielectric, and magnetic properties. J Sol–Gel Sci Technol. 2019;90(3):631–42.
[40] Kefeni KK, Msagati TM, Mamba BB. Synthesis and characterization of magnetic nanoparticles and study their removal capacity of metals from acid mine drainage. Chem Eng J. 2015;276:222–31.
[41] Thakur S, Rai R, Sharma S. Structural characterization and magnetic study of $NiFe_xO_4$ synthesized by co-precipitation method. Mater Lett. 2015;139:368–72.
[42] Zi Z, Sun Y, Zhu X, Yang Z, Dai J, Song W. Synthesis and magnetic properties of $CoFe_2O_4$ ferrite nanoparticles. J Magn Magn Mater. 2009;321(9):1251–5.
[43] Xing Y, Jin Y-Y, Si J-C, Peng M-L, Wang X-F, Chen C, et al. Controllable synthesis and characterization of Fe_3O_4/Au composite nanoparticles. J Magn Magn Mater. 2015;380:150–6.
[44] Nabiyouni G, Julaee M, Ghanbari D, Aliabadi PC, Safaie N. Room temperature synthesis and magnetic property studies of Fe_3O_4 nanoparticles prepared by a simple precipitation method. J Ind Eng Chem. 2015;21:599–603.
[45] Sharifi I, Shokrollahi H, Amiri S. Ferrite-based magnetic nanofluids used in hyperthermia applications. J Magn Magn Mater. 2012;324(6):903–15.
[46] Wang J, White WB, Adair JH. Optical properties of hydrothermally synthesized hematite particulate pigments. J Am Ceram Soc. 2005;88(12):3449–54.
[47] Zhang J, Song J-M, Niu H-L, Mao C-J, Zhang S-Y, Shen Y-H. $ZnFe_2O_4$ nanoparticles: Synthesis, characterization, and enhanced gas sensing property for acetone. Sens Actuators B Chem. 2015;221:55–62.
[48] Asogekar PA, Verenkar VMS. Structural and magnetic properties of nanosized $CoxZn(1–x)Fe_2O_4$ (x = 0.0, 0.5, 1.0) synthesized via autocatalytic thermal decomposition of hydrazinated cobalt zinc ferrous succinate. Ceram Int. 2019;45(17, Part A):21793–803.
[49] Zakiyah LB, Saion E, Al-Hada NM, Gharibshahi E, Salem A, Soltani N, et al. Up-scalable synthesis of size-controlled copper ferrite nanocrystals by thermal treatment method. Mater Sci Semiconductor Process. 2015;40:564–9.
[50] Sartori K, Choueikani F, Gloter A, Begin-Colin S, Taverna D, Pichon BP. Room temperature blocked magnetic nanoparticles based on ferrite promoted by a three-step thermal decomposition process. J Am Chem Soc. 2019;141(25):9783–7.
[51] Flores-Arias Y, Vázquez-Victorio G, Ortega-Zempoalteca R, Acevedo-Salas U, Ammar S, Valenzuela R. Magnetic phase transitions in ferrite nanoparticles characterized by electron spin resonance. J Appl Phys. 2015;117(17):17A503.
[52] Gaudisson T, Beji Z, Herbst F, Nowak S, Ammar S, Valenzuela R. Ultrafine grained high density manganese zinc ferrite produced using polyol process assisted by spark plasma sintering. J Magn Magn Mater. 2015;387:90–5.
[53] Tian Y, Yu B, Li X, Li K. Facile solvothermal synthesis of monodisperse Fe_3O_4 nanocrystals with precise size control of one nanometre as potential MRI contrast agents. J Mater Chem. 2011;21(8):2476–81.
[54] Ameer S, Gul IH, Mujahid M. Ultra low permittivity/loss $CoFe_2O_4$ and $CoFe_2O_4$–rGO nanohybrids by novel 1-hexanol assisted solvothermal process. J Alloy Compd. 2015;642:78–82.
[55] Shen CQ, Ji HN, Wu J, Zhu N, Niu JQ, Li HD, et al. editors. Synthesis and characterization of MnZn ferrite nanoparticles for biomedical applications. In 2018 IEEE International Conference on Applied Superconductivity and Electromagnetic Devices (ASEMD). Tianjin, China: IEEE; 2018.
[56] Rao P, Godbole RV, Phase DM, Chikate RC, Bhagwat S. Ferrite thin films: synthesis, characterization and gas sensing properties towards LPG. Mater Chem Phys. 2015;149–150:333–8.
[57] Singh Yadav R, Kuřitka I, Vilcakova J, Jamatia T, Machovsky M, Skoda D, et al. Impact of sonochemical synthesis condition on the structural and physical properties of $MnFe_2O_4$ spinel ferrite nanoparticles. Ultrason Sonochem. 2020;61:104839.
[58] Almessiere MA, Slimani Y, Guner S, Sertkol M, Demir Korkmaz A, Shirsath SE, et al. Sonochemical synthesis and physical properties of $Co_{0.3}Ni_{0.5}Mn_{0.2}EuxFe_{2-x}O_4$ nano-spinel ferrites. Ultrason Sonochem. 2019;58:104654.
[59] Jalili NA, Muscarello M, Gaharwar AK. Nanoengineered thermoresponsive magnetic hydrogels for biomedical applications. Bioeng Transl Med. 2016;1(3):297–305.

[60] Sung B, Kim M-H, Abelmann L. Magnetic microgels and nanogels: physical mechanisms and biomedical applications. Bioeng Transl Med. 2021;6(1):e10190.
[61] Kefeni KK, Msagati TAM, Mamba BB. Ferrite nanoparticles: synthesis, characterisation and applications in electronic device. Mater Sci Eng B. 2017;215:37–55.
[62] Reda SM. Synthesis of ZnO and Fe_2O_3 nanoparticles by sol–gel method and their application in dye-sensitized solar cells. Mater Sci Semiconductor Process. 2010;13(5):417–25.
[63] Alshahrani B, ElSaeedy HI, fares S, Korna AH, Yakout HA, Maksoud MIAA, et al. The effect of Ce^{3+} doping on structural, optical, ferromagnetic resonance, and magnetic properties of $ZnFe_2O_4$ nanoparticles. Sci: Mater Electron. 2020;32(1):780–97.
[64] Maksoud MA, El-Sayyad GS, Abokhadra A, Soliman L, El-Bahnasawy H, Ashour A. Influence of Mg^{2+} substitution on structural, optical, magnetic, and antimicrobial properties of Mn–Zn ferrite nanoparticles. J Mater Sci Mater Electron. 2020;31(3):2598–616.
[65] Osman AI, Skillen NC, Robertson PKJ, Rooney DW, Morgan K. Exploring the photocatalytic hydrogen production potential of titania doped with alumina derived from foil waste. Int J Hydrog Energy. 2020;45(59):34494–502.
[66] Osman AI, Abu-Dahrieh JK, McLaren M, Laffir F, Nockemann P, Rooney D. A facile green synthetic route for the preparation of highly active gamma-Al_2O_3 from aluminum foil waste. Sci Rep. 2017;7(1):3593.
[67] Osman AI, Abu-Dahrieh JK. Kinetic Investigation of η-Al_2O_3 catalyst for dimethyl ether production. Catal Lett. 2018;148(4):1236–45.
[68] Osman AI, Meudal J, Laffir F, Thompson J, Rooney D. Enhanced catalytic activity of Ni on η-Al_2O_3 and ZSM-5 on addition of ceria zirconia for the partial oxidation of methane. Appl Catal B Environ. 2017;212:68–79.
[69] Rahimi R, Maleki A, Maleki S, Morsali A, Rahimi MJ. Synthesis and characterization of magnetic dichromate hybrid nanomaterials with triphenylphosphine surface modified iron oxide nanoparticles (Fe_3O_4@SiO2@PPh3@Cr_2O_{72-}). Solid State Sci. 2014;28:9–13.
[70] El Ghandoor H, Zidan H, Khalil MM, Ismail M. Synthesis and some physical properties of magnetite (Fe_3O_4) nanoparticles. Int J Electrochem Sci. 2012;7(6):5734–45.
[71] Amiri S, Shokrollahi H. Magnetic and structural properties of RE doped Co-ferrite (REåNd, Eu, and Gd) nano-particles synthesized by co-precipitation. J Magn Magn Mater. 2013;345:18–23.
[72] Li H, Qin L, Feng Y, Hu L, Zhou C. Preparation and characterization of highly water-soluble magnetic Fe_3O_4 nanoparticles via surface double-layered self-assembly method of sodium alpha-olefin sulfonate. J Magn Magn Mater. 2015;384:213–8.
[73] Gul S, Yousuf MA, Anwar A, Warsi MF, Agboola PO, Shakir I, et al. Al-substituted zinc spinel ferrite nanoparticles: preparation and evaluation of structural, electrical, magnetic and photocatalytic properties. Ceram Int. 2020;46(9):14195–205.
[74] Zhang H, Zhu G. One-step hydrothermal synthesis of magnetic Fe_3O_4 nanoparticles immobilized on polyamide fabric. Appl Surf Sci. 2012;258(11):4952–9.
[75] Ding Z, Wang W, Zhang Y, Li F, Liu JP. Synthesis, characterization and adsorption capability for Congo red of $CoFe_2O_4$ ferrite nanoparticles. J Alloy Compd. 2015;640:362–70.
[76] Yang Y, Liu X, Yang Y, Xiao W, Li Z, Xue D, et al. Synthesis of nonstoichiometric zinc ferrite nanoparticles with extraordinary room temperature magnetism and their diverse applications. J Mater Chem C. 2013;1(16):2875–85.
[77] Sharifi I, Zamanian A, Behnamghader A. Synthesis and characterization of $Fe_{0.6}Zn_{0.4}Fe_2O_4$ ferrite magnetic nanoclusters using simple thermal decomposition method. J Magn Magn Mater. 2016;412:107–13.
[78] Leonel LV, Barbosa JBS, Miquita DR, Oliveira FP, Fernandez-Outon LE, Oliveira EF, et al. Facile polyol synthesis of ultrasmall water-soluble cobalt ferrite nanoparticles. Solid State Sci. 2018;86:45–52.
[79] Hanini A, Massoudi ME, Gavard J, Kacem K, Ammar S, Souilem O. Nanotoxicological study of polyol-made cobalt-zinc ferrite nanoparticles in rabbit. Environ Toxicol Pharmacol. 2016;45:321–7.
[80] Gaudisson T, Artus M, Acevedo U, Herbst F, Nowak S, Valenzuela R, et al. On the microstructural and magnetic properties of fine-grained $CoFe_2O_4$ ceramics produced by combining polyol process and spark plasma sintering. J Magn Magn Mater. 2014;370:87–95.
[81] Aparna ML, Grace AN, Sathyanarayanan P, Sahu NK. A comparative study on the supercapacitive behaviour of solvothermally prepared metal ferrite (MFe_2O_4, M= Fe, Co, Ni, Mn, Cu, Zn) nanoassemblies. J Alloy Compd. 2018;745:385–95.
[82] Ghobashy MM. *In-situ* core-shell polymerization of magnetic polymer nanocomposite (PAAc/Fe_3O_4) particles via gamma radiation. Nanocomposites. 2017;3(1):42–6.
[83] Ghobashy MM. Combined ultrasonic and gamma-irradiation to prepare TiO_2@ PET-*g*-PAAc fabric composite for self-cleaning application. Ultrason Sonochem. 2017;37:529–35.
[84] Bang JH, Suslick KS. Applications of ultrasound to the synthesis of nanostructured materials. Adv Mater. 2010;22(10):1039–59.
[85] Almessiere MA, Slimani Y, Unal B, Zubar TI, Sadaqat A, Trukhanov AV, et al. Microstructure, dielectric and microwave features of $[Ni_{0.4}Cu_{0.2}Zn_{0.4}](Fe_{2-x}Tb_x)O_4$($x \leq 0.1$) nanospinel ferrites. J Mater Res Technol. 2020;9(5):10608–23.
[86] Minin R, Itin V, Zhuravlev V, Svetlichnyi V, editors. Synthesis of cubic ferrite $CoFe_2O_4$ by spray pyrolysis. In Journal of Physics: Conference Series. IOP Publishing; 2018. p. 042011
[87] Abdel Maksoud MIA, Elgarahy AM, Farrell C, Al-Muhtaseb AH, Rooney DW, Osman AI. Insight on water remediation application using magnetic nanomaterials and biosorbents. Coord Chem Rev. 2020;403:213096.
[88] Shah MS, Ali K, Ali I, Mahmood A, Ramay SM, Farid MT. Structural and magnetic properties of praseodymium substituted barium-based spinel ferrites. Mater Res Bull. 2018;98:77–82.
[89] Yadav RS, Kuřitka I, Havlica J, Hnatko M, Alexander C, Masilko J, et al. Structural, magnetic, elastic, dielectric and electrical properties of hot-press sintered $Co_{1-x}Zn_xFe_2O_4$ (x = 0.0, 0.5) spinel ferrite nanoparticles. J Magn Magn Mater. 2018;447:48–57.

[90] Abdel Maksoud MIA, El-Ghandour A, El-Sayyad GS, Fahim RA, El-Hanbaly AH, Bekhit M, et al. Unveiling the effect of Zn^{2+} substitution in enrichment of structural, magnetic, and dielectric properties of Cobalt Ferrite. J Inorg Organomet Polym Mater. 2020;30(9):3709–21.

[91] Reyes-Rodríguez PY, Cortés-Hernández DA, Escobedo-Bocardo JC, Almanza-Robles JM, Sánchez-Fuentes HJ, Jasso-Terán A, et al. Structural and magnetic properties of Mg–Zn ferrites ($Mg_{1-x}Zn_xFe_2O_4$) prepared by sol–gel method. J Magn Magn Mater. 2017;427:268–71.

[92] Ghodake U, Kambale RC, Suryavanshi S. Effect of Mn^{2+} substitution on structural, electrical transport and dielectric properties of Mg–Zn ferrites. Ceram Int. 2017;43(1):1129–34.

[93] McCusker LB, Von Dreele RB, Cox DE, Louer D, Scardi P. Rietveld refinement guidelines. J Appl Crystal. 1999;32(1):36–50.

[94] Gao Y, Wang Z, Pei J, Zhang H. Structural, elastic, thermal and soft magnetic properties of Ni–Zn–Li ferrites. J Alloy Compd. 2019;774:1233–42.

[95] Ashour A, El-Batal AI, Maksoud MA, El-Sayyad GS, Labib S, Abdeltwab E, et al. Antimicrobial activity of metal-substituted cobalt ferrite nanoparticles synthesized by sol–gel technique. Particuology. 2018;40:141–51.

[96] Massoudi J, Smari M, Nouri K, Dhahri E, Khirouni K, Bertaina S, et al. Magnetic and spectroscopic properties of Ni–Zn–Al ferrite spinel: from the nanoscale to microscale. RSC Adv. 2020;10(57):34556–80.

[97] Ghosh MP, Mukherjee S. Tuning the microstructural, magnetic and optical properties of Cr substituted nanocrystalline copper-nickel ferrites. J Magn Magn Mater. 2020;498:166185.

[98] Poudel TP, Rai BK, Yoon S, Guragain D, Neupane D, Mishra SR. The effect of gadolinium substitution in inverse spinel nickel ferrite: structural, magnetic, and Mössbauer study. J Alloy Compd. 2019;802:609–19.

[99] Jadhav VV, Shirsat SD, Tumberphale UB, Mane RS. Chapter 3 – Properties of ferrites. In Spinel ferrite nanostructures for energy storage devices. Oxford, Oxfordshire, United Kingdom: Elsevier; 2020. p. 35–50.

[100] Sharifianjazi F, Moradi M, Parvin N, Nemati A, Jafari Rad A, Sheysi N, et al. Magnetic $CoFe_2O_4$ nanoparticles doped with metal ions: a review. Ceram Int. 2020;46(11, Part B):18391–412.

[101] Hanini A, Lartigue L, Gavard J, Kacem K, Wilhelm C, Gazeau F, et al. Zinc substituted ferrite nanoparticles with $Zn_{0.9}Fe_{2.1}O_4$ formula used as heating agents for *in vitro* hyperthermia assay on glioma cells. J Magn Magn Mater. 2016;416:315–20.

[102] Zargar T, Kermanpur A. Effects of hydrothermal process parameters on the physical, magnetic and thermal properties of $Zn_{0.3}Fe_{2.7}O_4$ nanoparticles for magnetic hyperthermia applications. Ceram Int. 2017;43(7):5794–804.

[103] Krishnan KM. Biomedical nanomagnetics: a spin through possibilities in imaging, diagnostics, and therapy. IEEE Trans Magn. 2010;46(7):2523–58.

[104] Kumar CSSR, Mohammad F. Magnetic nanomaterials for hyperthermia-based therapy and controlled drug delivery. Adv Drug Delivery Rev. 2011;63(9):789–808.

[105] Tran N, Webster TJ. Magnetic nanoparticles: biomedical applications and challenges. J Mater Chem. 2010;20(40):8760–7.

[106] Di Corato R, Béalle G, Kolosnjaj-Tabi J, Espinosa A, Clement O, Silva AKA, et al. Combining magnetic hyperthermia and photodynamic therapy for tumor ablation with photoresponsive magnetic liposomes. ACS Nano. 2015;9(3):2904–16.

[107] Psimadas D, Baldi G, Ravagli C, Comes Franchini M, Locatelli E, Innocenti C, et al. Comparison of the magnetic, radiolabeling, hyperthermic and biodistribution properties of hybrid nanoparticles bearing $CoFe_2O_4$and Fe_3O_4 metal cores. Nanotechnology. 2013;25(2):25101.

[108] Hasirci C, Karaagac O, Köçkar H. Superparamagnetic zinc ferrite: a correlation between high magnetizations and nanoparticle sizes as a function of reaction time via hydrothermal process. J Magn Magn Mater. 2019;474:282–6.

[109] Guardia P, Di Corato R, Lartigue L, Wilhelm C, Espinosa A, Garcia-Hernandez M, et al. Water-soluble iron oxide nanocubes with high values of specific absorption rate for cancer cell hyperthermia treatment. ACS Nano. 2012;6(4):3080–91.

[110] Sasikala ARK, Unnithan AR, Yun Y-H, Park CH, Kim CS. An implantable smart magnetic nanofiber device for endoscopic hyperthermia treatment and tumor-triggered controlled drug release. Acta Biomater. 2016;31:122–33.

[111] Giustini AJ, Petryk AA, Cassim SM, Tate JA, Baker I, Hoopes PJ. Magnetic nanoparticle hyperthermia in cancer treatment. Nano Life. 2010;1(1–2):17–32.

[112] Jordan A, Wust P, Scholz R, Faeling H, Krause J, Felix R. Scientific and clinical applications of magnetic carriers. In: Häfeli W, Schütt J, editors. Springer, Boston, MA: Springer Nature; 1997

[113] Manikandan A, Vijaya JJ, Kennedy LJ, Bououdina M. Structural, optical and magnetic properties of $Zn_{1-x}Cu_xFe_2O_4$ nanoparticles prepared by microwave combustion method. J Mol Structure. 2013;1035:332–40.

[114] Singh SB, Srinivas C, Tirupanyam BV, Prajapat CL, Singh MR, Meena SS, et al. Structural, thermal and magnetic studies of $Mg_xZn_{1-x}Fe_2O_4$ nanoferrites: study of exchange interactions on magnetic anisotropy. Ceram Int. 2016;42(16):19179–86.

[115] Sagayaraj R, Aravazhi S, Praveen P, Chandrasekaran G. Structural, morphological and magnetic characters of PVP coated $ZnFe_2O_4$ nanoparticles. J Mater Sci Mater Electron. 2018;29(3):2151–8.

[116] Pawar RA, Patange SM, Shitre AR, Gore SK, Jadhav SS, Shirsath SE. Crystal chemistry and single-phase synthesis of Gd3+ substituted Co–Zn ferrite nanoparticles for enhanced magnetic properties. RSC Adv. 2018;8(44):25258–67.

[117] Da Silva FG, Depeyrot J, Campos AF, Aquino R, Fiorani D, Peddis D. Structural and magnetic properties of spinel ferrite nanoparticles. J Nanosci Nanotechnol. 2019;19(8):4888–902.

[118] Zhang W, Zuo X, Niu Y, Wu C, Wang S, Guan S, et al. Novel nanoparticles with Cr^{3+} substituted ferrite for self-regulating temperature hyperthermia. Nanoscale. 2017;9(37):13929–37.

[119] Lee JE, Lee N, Kim H, Kim J, Choi SH, Kim JH, et al. Uniform mesoporous dye-doped silica nanoparticles decorated with multiple magnetite nanocrystals for simultaneous enhanced magnetic resonance imaging, fluorescence imaging, and drug delivery. J Am Chem Soc. 2010;132(2):552–7.

[120] Zhou X, Chen X, Mao TC, Li X, Shi XH, Fan DL, et al. Carbon ion implantation: a good method to enhance the biocompatibility of silicone rubber. Plastic Reconstruct Surg. 2016;137(4):690e–9e.
[121] Ghobashy MM, El-Sawy NM, Kodous AS. Nanocomposite of cosubstituted carbonated hydroxyapatite fabricated inside poly(sodium hyaluronate-acrylamide) hydrogel template prepared by gamma radiation for osteoblast cell regeneration. Radiat Phys Chem. 2021;183:109408.
[122] Gorgizadeh M, Azarpira N, Sattarahmady N. *In vitro* and *in vivo* tumor annihilation by near-infrared photothermal effect of a $NiFe_2O_4$/C nanocomposite. Colloids Surf B: Biointerfaces. 2018;170:393–400.
[123] Vilas-Boas V, Carvalho F, Espiña B. Magnetic hyperthermia for cancer treatment: main parameters affecting the outcome of *in vitro* and *in vivo* studies. Molecules. 2020;25(12):2874.
[124] Zhang Z-Q, Song S-C. Thermosensitive/superparamagnetic iron oxide nanoparticle-loaded nanocapsule hydrogels for multiple cancer hyperthermia. Biomaterials. 2016;106:13–23.
[125] Bisht G, Zaidi MGH, Rayamajhi S. Supercritical carbon dioxide–assisted synthesis of stimuli-responsive magnetic poly (*N*-isopropylacrylamide)–ferrite biocompatible nanocomposites for targeted and controlled drug delivery. Int J Polymeric Mater Polymeric Biomater. 2017;66(14):708–16.
[126] Li Q, Kartikowati CW, Horie S, Ogi T, Iwaki T, Okuyama K. Correlation between particle size/domain structure and magnetic properties of highly crystalline Fe_3O_4 nanoparticles. Sci Rep. 2017;7(1):1–7.
[127] Wang G, Zhou F, Du T, Lu Z, Ma Y, Mu J, et al. Controlled assembly of $MnFe_2O_4$ nanoparticles on MoS_2 nanosheets by a facile sonochemical method. J Magn Magn Mater. 2019;476:453–8.
[128] Xie W, Gao Q, Wang D, Guo Z, Gao F, Wang X, et al. Doxorubicin-loaded Fe_3O_4@MoS_2-PEG-2DG nanocubes as a theranostic platform for magnetic resonance imaging-guided chemo-photothermal therapy of breast cancer. Nano Res. 2018;11(5):2470–87.
[129] Almessiere MA, Slimani Y, Rehman S, Khan FA, Polat EG, Sadaqat A, et al. Synthesis of Dy-Y co-substituted manganese-zinc spinel nanoferrites induced anti-bacterial and anti-cancer activities: Comparison between sonochemical and sol–gel auto-combustion methods. Mater Sci Eng C. 2020;116:111186.
[130] Hassanzadeh-Tabrizi S, Norbakhsh H, Pournajaf R, Tayebi M. Synthesis of mesoporous cobalt ferrite/hydroxyapatite core-shell nanocomposite for magnetic hyperthermia and drug release applications. Ceram Int. 2021;47(13):18167–76.
[131] Wijesinghe W, Mantilaka M, Premalal E, Herath H, Mahalingam S, Edirisinghe M, et al. Facile synthesis of both needle-like and spherical hydroxyapatite nanoparticles: effect of synthetic temperature and calcination on morphology, crystallite size and crystallinity. Mater Sci Eng: C. 2014;42:83–90.
[132] Ansari M, Bigham A, Hassanzadeh-Tabrizi S, Ahangar HA. Synthesis and characterization of $Cu_{0.3}Zn_{0.5}Mg_{0.2}Fe_2O_4$ nanoparticles as a magnetic drug delivery system. J Magn Magn Mater. 2017;439:67–75.
[133] Wu J, Zhu YJ, Cao SW, Chen F. Hierachically nanostructured mesoporous spheres of calcium silicate hydrate: surfactant-free sonochemical synthesis and drug-delivery system with ultrahigh drug-loading capacity. Adv Mater. 2010;22(6):749–53.
[134] Khamsehashari N, Hassanzadeh-Tabrizi S, Bigham A. Effects of strontium adding on the drug delivery behavior of silica nanoparticles synthesized by P123-assisted sol–gel method. Mater Chem Phys. 2018;205:283–91.
[135] Gharibshahian M, Mirzaee O, Nourbakhsh M. Evaluation of superparamagnetic and biocompatible properties of mesoporous silica coated cobalt ferrite nanoparticles synthesized via microwave modified Pechini method. J Magn Magn Mater. 2017;425:48–56.
[136] Aval NA, Islamian JP, Hatamian M, Arabfirouzjaei M, Javadpour J, Rashidi M-R. Doxorubicin loaded large-pore mesoporous hydroxyapatite coated superparamagnetic Fe_3O_4 nanoparticles for cancer treatment. Int J Pharm. 2016;509(1–2):159–67.
[137] Sangeetha K, Ashok M, Girija E. Development of multifunctional cobalt ferrite/hydroxyapatite nanocomposites by microwave assisted wet precipitation method: a promising platform for synergistic chemo-hyperthermia therapy. Ceram Int. 2019;45(10):12860–9.
[138] Talaei M, Hassanzadeh-Tabrizi S, Saffar-Teluri A. Synthesis of mesoporous $CuFe_2O_4$@ SiO_2 core–shell nanocomposite for simultaneous drug release and hyperthermia applications. Ceram Int. 2021;47:30287–97.
[139] Radmansouri M, Bahmani E, Sarikhani E, Rahmani K, Sharifianjazi F, Irani M. Doxorubicin hydrochloride-loaded electrospun chitosan/cobalt ferrite/titanium oxide nanofibers for hyperthermic tumor cell treatment and controlled drug release. Int J Biol Macromol. 2018;116:378–84.
[140] Wang G, Ma Y, Wei Z, Qi M. Development of multifunctional cobalt ferrite/graphene oxide nanocomposites for magnetic resonance imaging and controlled drug delivery. Chem Eng J. 2016;289:150–60.
[141] Suárez J, Daboin V, González G, Briceño S. Chitosan-polyvinylpyrrolidone $Co_xFe_{3-x}O_4$($0.25 \leq x \leq 1$) nanoparticles for hyperthermia applications. Int J Biol Macromol. 2020;164:3403–10.
[142] Daboin V, Briceño S, Suárez J, Carrizales-Silva L, Alcalá O, Silva P, et al. Magnetic SiO_2-$Mn_{1-x}Co_xFe_2O_4$ nanocomposites decorated with Au@Fe_3O_4 nanoparticles for hyperthermia. J Magn Magn Mater. 2019;479:91–8.
[143] Mondal D, Borgohain C, Paul N, Borah J. Improved heating efficiency of bifunctional $MnFe_2O_4$/ZnS nanocomposite for magnetic hyperthermia application. Phys B Condens Matter. 2019;567:122–8.
[144] Hatamie S, Balasi ZM, Ahadian MM, Mortezazadeh T, Shams F, Hosseinzadeh S. Hyperthermia of breast cancer tumor using graphene oxide-cobalt ferrite magnetic nanoparticles in mice. J Drug Delivery Sci Technol. 2021;65:102680.
[145] Lin Q, Xu J, Yang F, Lin J, Yang H, He Y. Magnetic and Mössbauer spectroscopy studies of zinc-substituted cobalt ferrites prepared by the sol–gel method. Materials (Basel, Switzerland). 2018;11(10):1799.
[146] Balakrishnan PB, Silvestri N, Fernandez-Cabada T, Marinaro F, Fernandes S, Fiorito S, et al. Exploiting unique alignment of cobalt Ferrite nanoparticles, mild hyperthermia, and controlled intrinsic cobalt toxicity for cancer therapy. Adv Mater. 2020;32(45):2003712.

[147] Di Corato R, Espinosa A, Lartigue L, Tharaud M, Chat S, Pellegrino T, et al. Magnetic hyperthermia efficiency in the cellular environment for different nanoparticle designs. Biomaterials. 2014;35(24):6400–11.
[148] Zyuzin MV, Cassani M, Barthel MJ, Gavilan H, Silvestri N, Escudero A, et al. Confining iron oxide nanocubes inside submicrometric cavities as a key strategy to preserve magnetic heat losses in an intracellular environment. ACS Appl Mater Interfaces. 2019;11(45):41957–71.
[149] Cabrera D, Lak A, Yoshida T, Materia ME, Ortega D, Ludwig F, et al. Unraveling viscosity effects on the hysteresis losses of magnetic nanocubes. Nanoscale. 2017;9(16):5094–101.
[150] Kolosnjaj-Tabi J, Di Corato R, Lartigue L, Marangon I, Guardia P, Silva AKA, et al. Heat-generating iron oxide nanocubes: subtle "Destructurators" of the tumoral microenvironment. ACS Nano. 2014;8(5):4268–83.
[151] Mai BT, Balakrishnan PB, Barthel MJ, Piccardi F, Niculaes D, Marinaro F, et al. Thermoresponsive iron oxide nanocubes for an effective clinical translation of magnetic hyperthermia and heat-mediated chemotherapy. ACS Appl Mater Interfaces. 2019;11(6):5727–39.
[152] Marangon I, Silva AAK, Guilbert T, Kolosnjaj-Tabi J, Marchiol C, Natkhunarajah S, et al. Tumor stiffening, a key determinant of tumor progression, is reversed by nanomaterial-induced photothermal therapy. Theranostics. 2017;7(2):329–43.
[153] Chu X-Y, Huang W, Wang Y-L, Meng L-W, Chen L-Q, Jin M-J, et al. Improving antitumor outcomes for palliative intratumoral injection therapy through lecithin- chitosan nanoparticles loading paclitaxel- cholesterol complex. Int J Nanomed. 2019;14:689–705.
[154] Lee N, Yoo D, Ling D, Cho MH, Hyeon T, Cheon J. Iron oxide based nanoparticles for multimodal imaging and magnetoresponsive therapy. Chem Rev. 2015;115(19):10637–89.
[155] Chen Y, Nan J, Lu Y, Wang C, Chu F, Gu Z. Hybrid Fe_3O_4-poly (acrylic acid) nanogels for theranostic cancer treatment. J Biomed Nanotechnol. 2015;11(5):771–9.
[156] Yang Y, Li Y, Sun Q-y. Archaeal and bacterial communities in acid mine drainage from metal-rich abandoned tailing ponds, Tongling, China. Trans Nonferrous Met Soc China. 2014;24(10):3332–42.
[157] Ponce AM, Viglianti BL, Yu D, Yarmolenko PS, Michelich CR, Woo J, et al. Magnetic resonance imaging of temperature-sensitive liposome release: drug dose painting and antitumor effects. J Natl Cancer Inst. 2007;99(1):53–63.
[158] Jain RK, Stylianopoulos T. Delivering nanomedicine to solid tumors. Nat Rev Clin Oncol. 2010;7(11):653–64.
[159] Namiki Y, Namiki T, Yoshida H, Ishii Y, Tsubota A, Koido S, et al. A novel magnetic crystal–lipid nanostructure for magnetically guided *in vivo* gene delivery. Nat Nanotechnol. 2009;4(9):598–606.
[160] Alexiou C, Arnold W, Klein RJ, Parak FG, Hulin P, Bergemann C, et al. Locoregional cancer treatment with magnetic drug targeting. Cancer Res. 2000;60(23):6641.
[161] Torchilin VP. Recent advances with liposomes as pharmaceutical carriers. Nat Rev Drug Discovery. 2005;4(2):145–60.
[162] Gupta AK, Gupta M. Synthesis and surface engineering of iron oxide nanoparticles for biomedical applications. Biomaterials. 2005;26(18):3995–4021.
[163] Balakrishnan S, Bonder MJ, Hadjipanayis GC. Particle size effect on phase and magnetic properties of polymer-coated magnetic nanoparticles. J Magn Magn Mater. 2009;321(2):117–22.
[164] Karimi Z, Karimi L, Shokrollahi H. Nano-magnetic particles used in biomedicine: Core and coating materials. Mater Sci Eng C. 2013;33(5):2465–75.
[165] Albino M, Fantechi E, Innocenti C, López-Ortega A, Bonanni V, Campo G, et al. Role of Zn^{2+} substitution on the magnetic, hyperthermic, and relaxometric properties of cobalt ferrite nanoparticles. J Phys Chem C. 2019;123(10):6148–57.
[166] Almessiere MA, Slimani Y, Sertkol M, Khan FA, Nawaz M, Tombuloglu H, et al. Ce–Nd Co-substituted nanospinel cobalt ferrites: an investigation of their structural, magnetic, optical, and apoptotic properties. Ceram Int. 2019;45(13):16147–56.
[167] Zhang H, Wang J, Zeng Y, Wang G, Han S, Yang Z, et al. Leucine-coated cobalt ferrite nanoparticles: Synthesis, characterization and potential biomedical applications for drug delivery. Phys Lett A. 2020;384(24):126600.
[168] Iqbal S, Fakhar-e-Alam M, Atif M, Amin N, Alimgeer KS, Ali A, et al. Structural, morphological, antimicrobial, and *in vitro* photodynamic therapeutic assessments of novel Zn+2-substituted cobalt ferrite nanoparticles. Results Phys. 2019;15:102529.
[169] Ahamed M, Akhtar MJ, Alhadlaq HA, Alshamsan A. Copper ferrite nanoparticle-induced cytotoxicity and oxidative stress in human breast cancer MCF-7 cells. Colloids Surf B Biointerfaces. 2016;142:46–54.
[170] Atif M, Fakhar-e-Alam M, AlSalhi MS. Role of sensitivity of zinc oxide nanorods (ZnO-NRs) based photosensitizers in hepatocellular site of biological tissue. Laser Phys. 2011;21(11):1950–61.
[171] McBain SC, Yiu HH, Dobson J. Magnetic nanoparticles for gene and drug delivery. Int J Nanomed. 2008;3(2):169–80.
[172] Cai B, Zhao M, Ma Y, Ye Z, Huang J. Bioinspired formation of 3D hierarchical $CoFe_2O_4$ porous microspheres for magnetic-controlled drug release. ACS Appl Mater Interfaces. 2015;7(2):1327–33.
[173] Srinivasan SY, Paknikar KM, Bodas D, Gajbhiye V. Applications of cobalt ferrite nanoparticles in biomedical nanotechnology. Nanomedicine. 2018;13(10):1221–38.
[174] Liu M, Pan L, Piao H, Sun H, Huang X, Peng C, et al. Magnetically actuated wormlike nanomotors for controlled cargo release. ACS Appl Mater Interfaces. 2015;7(47):26017–21.
[175] Iatridi Z, Vamvakidis K, Tsougos I, Vassiou K, Dendrinou-Samara C, Bokias G. Multifunctional polymeric platform of magnetic ferrite colloidal superparticles for luminescence, imaging, and hyperthermia applications. ACS Appl Mater Interfaces. 2016;8(51):35059–70.
[176] Yang J-C, Chen Y, Li Y-H, Yin X-B. Magnetic resonance imaging-guided multi-drug chemotherapy and photothermal synergistic therapy with pH and NIR-stimulation release. ACS Appl Mater Interfaces. 2017;9(27):22278–88.
[177] Fantechi E, Innocenti C, Zanardelli M, Fittipaldi M, Falvo E, Carbo M, et al. A smart platform for hyperthermia application in cancer treatment: cobalt-doped ferrite nanoparticles

mineralized in human ferritin cages. ACS Nano. 2014;8(5):4705–19.
[178] Ebrahimi Fard A, Zarepour A, Zarrabi A, Shanei A, Salehi H. Synergistic effect of the combination of triethylene-glycol modified Fe_3O_4 nanoparticles and ultrasound wave on MCF-7 cells. J Magn Magn Mater. 2015;394:44–9.
[179] Vallabani NVS, Singh S. Recent advances and future prospects of iron oxide nanoparticles in biomedicine and diagnostics. 3 Biotech. 2018;8(6):279.
[180] Saha P, Rakshit R, Mandal K. Enhanced magnetic properties of Zn doped Fe_3O_4 nano hollow spheres for better bio-medical applications. J Magn Magn Mater. 2019;475:130–6.
[181] de Mello LB, Varanda LC, Sigoli FA, Mazali IO. Co-precipitation synthesis of (Zn-Mn)-co-doped magnetite nanoparticles and their application in magnetic hyperthermia. J Alloy Compd. 2019;779:698–705.
[182] Thu Huong LT, Nam NH, Doan DH, My Nhung HT, Quang BT, Nam PH, et al. Folate attached, curcumin loaded Fe_3O_4 nanoparticles: a novel multifunctional drug delivery system for cancer treatment. Mater Chem Phys. 2016;172:98–104.
[183] Tietze R, Zaloga J, Unterweger H, Lyer S, Friedrich RP, Janko C, et al. Magnetic nanoparticle-based drug delivery for cancer therapy. Biochem Biophys Res Commun. 2015;468(3):463–70.
[184] Shen J-M, Guan X-M, Liu X-Y, Lan J-F, Cheng T, Zhang H-X. Luminescent/magnetic hybrid nanoparticles with folate-conjugated peptide composites for tumor-targeted drug delivery. Bioconjugate Chem. 2012;23(5):1010–21.
[185] Lee JH, Jang JT, Choi JS, Moon SH, Noh SH, Kim JW, et al. Exchange-coupled magnetic nanoparticles for efficient heat induction. Nat Nanotechnol. 2011;6(7):418–22.
[186] Montha W, Maneeprakorn W, Buatong N, Tang IM, Pon-On W. Synthesis of doxorubicin-PLGA loaded chitosan stabilized (Mn, Zn)Fe_2O_4 nanoparticles: biological activity and pH-responsive drug release. Mater Sci Eng C. 2016;59:235–40.
[187] Wang G, Ma Y, Zhang L, Mu J, Zhang Z, Zhang X, et al. Facile synthesis of manganese ferrite/graphene oxide nanocomposites for controlled targeted drug delivery. J Magn Magn Mater. 2016;401:647–50.
[188] Almessiere MA, Slimani Y, Rehman S, Khan FA, Güngüneş ÇD, Güner S, et al. Magnetic properties, anticancer and antibacterial effectiveness of sonochemically produced Ce^{3+}/Dy^{3+} co-activated Mn–Zn nanospinel ferrites. Arab J Chem. 2020;13(10):7403–17.
[189] Hekmat A, Saboury AA. Structural effects of the synthetic-cobalt–manganese-zinc ferrite nanoparticles ($Co_{0.3}Mn_{0.2}Zn_{0.5}Fe_2O_4$ NPs) on DNA and its antiproliferative effect on T47Dcells. BioNanoScience. 2019;9(4):821–32.
[190] Jin KL, Park JY, Noh EJ, Hoe KL, Lee JH, Kim JH, et al. The effect of combined treatment with *cis*platin and histone deacetylase inhibitors on HeLa cells. J Gynecol Oncol. 2010;21(4):262–8.
[191] Ramasamy S, Enoch IVMV, Rex Jeya Rajkumar S. Polymeric cyclodextrin-dextran spooled nickel ferrite nanoparticles: expanded anticancer efficacy of loaded camptothecin. Mater Lett. 2020;261:127114.
[192] Alahmari F, Rehman S, Almessiere M, Khan FA, Slimani Y, Baykal A. Synthesis of $Ni_{0.5}Co_{0.5-x}Cd_xFe_{1.78}Nd_{0.02}O_4$ ($x \leq 0.25$) nanofibers by using electrospinning technique induce anti-cancer and anti-bacterial activities. J Biomol Struct Dyn. 2021;39(16):1–8.
[193] Khan FA, Akhtar S, Almohazey D, Alomari M, Almofty SA, Eliassari A. Fluorescent magnetic submicronic polymer (FMSP) nanoparticles induce cell death in human colorectal carcinoma cells. Artif Cells Nanomed Biotechnol. 2018;46(Sup 3):S247–53.
[194] Khan FA, Akhtar S, Almohazey D, Alomari M, Almofty SA, Badr I, et al. Targeted delivery of poly (methyl methacrylate) particles in colon cancer cells selectively attenuates cancer cell proliferation. Artif Cell Nanomed Biotechnol. 2019;47(1):1533–42.
[195] Tombuloglu H, Khan FA, Almessiere MA, Aldakheel S, Baykal A. Synthesis of niobium substituted cobalt-nickel nano-ferrite ($Co_{0.5}Ni_{0.5}Nb_xFe_{2-x}O_4$ ($x \leq 0.1$) by hydrothermal approach show strong anti-colon cancer activities. J Biomol Struct Dyn. 2021;39(6):1–9.
[196] Ghobashy MM, El-Sattar NEAA. Radiation synthesis of rapidly self-healing hydrogel derived from poly (acrylic acid) with good mechanical strength. Macromol Chem Phys. 2020;221(19):2000218.
[197] Ghobashy MM, Alshangiti DM, Alkhursani SA, Al-Gahtany SA, Shokr FS, Madani M. Improvement of *in vitro* dissolution of the poor water-soluble amlodipine drug by solid dispersion with irradiated polyvinylpyrrolidone. ACS Omega. 2020;5(34):21476–87.
[198] Elhady MA, Ghobashy MM, Mahmoud MA. Effect of gamma irradiation on the adhesive property and antibacterial activity of blend polymer (abietic acid-EVA). Polym Polym Compos. 2020;29:138–47.
[199] Alshangiti DM, Ghobashy MM, Alkhursani SA, Shokr FS, Al-Gahtany SA, Madani MM. Semi-permeable membrane fabricated from organoclay/PS/EVA irradiated by ɣ-rays for water purification from dyes. J Mater Res Technol. 2019;8(6):6134–45.
[200] Ghobashy MM, Alkhursani SA, Madani M. Radiation-induced nucleation and pH-controlled nanostructure shape of polyaniline dispersed in DMF. Polym Bull. 2018;75(12):5477–92.
[201] Ghobashy MM, Elhady MA. pH-sensitive wax emulsion copolymerization with acrylamide hydrogel using gamma irradiation for dye removal. Radiat Phys Chem. 2017;134:47–55.
[202] Ghobashy MM, El-Sawy NM, Kodous AS. Nanocomposite of cosubstituted carbonated hydroxyapatite fabricated inside poly (sodium hyaluronate-acrylamide) hydrogel template prepared by gamma radiation for osteoblast cell regeneration. Radiat Phys Chem. 2021;183:109408.
[203] Ghobashy MM, El-Damhougy BK, El-Wahab HA, Madani M, Amin MA, Naser AEM, et al. Controlling radiation degradation of a CMC solution to optimize the swelling of acrylic acid hydrogel as water and fertilizer carriers. Polym Adv Technol. 2021;32(2):514–24.
[204] Younis SA, Ghobashy MM, Bassioni G, Gupta AK. Tailored functionalized polymer nanoparticles using gamma radiation for selected adsorption of barium and strontium in oilfield wastewater. Arab J Chem. 2020;13(2):3762–74.
[205] Mohamady Ghobashy M, Sayed WAA, El-Helaly A. Impact of silver nanoparticles synthesized by irradiated polyvinylpyrrolidone on spodoptera littoralis nucleopolyhedrosis virus activity. J Polym Environ. 2021;29:3364–74.

[206] Jang JT, Nah H, Lee JH, Moon SH, Kim MG, Cheon J. Critical enhancements of MRI contrast and hyperthermic effects by dopant-controlled magnetic nanoparticles. Angew Chem Int Ed Engl. 2009;48(7):1234–8.
[207] Al-Qubaisi MS, Rasedee A, Flaifel MH, Ahmad SH, Hussein-Al-Ali S, Hussein MZ, et al. Cytotoxicity of nickel zinc ferrite nanoparticles on cancer cells of epithelial origin. Int J Nanomed. 2013;8:2497–508.
[208] Lartigue L, Wilhelm C, Servais J, Factor C, Dencausse A, Bacri J-C, et al. Nanomagnetic sensing of blood plasma protein interactions with iron oxide nanoparticles: impact on macrophage uptake. ACS Nano. 2012;6(3):2665–78.
[209] Mitamura S, Ikawa H, Mizuno N, Kaziro Y, Itoh H. Cytosolic nuclease activated by caspase-3 and inhibited by DFF-45. Biochem Biophys Res Commun. 1998;243(2):480–4.
[210] Ahamed M, Akhtar MJ, Siddiqui MA, Ahmad J, Musarrat J, Al-Khedhairy AA, et al. Oxidative stress mediated apoptosis induced by nickel ferrite nanoparticles in cultured A549 cells. Toxicology. 2011;283(2–3):101–8.
[211] Hathaway HJ, Butler KS, Adolphi NL, Lovato DM, Belfon R, Fegan D, et al. Detection of breast cancer cells using targeted magnetic nanoparticles and ultra-sensitive magnetic field sensors. Breast Cancer Res. 2011;13(5):R108.
[212] Sarala E, Madhukara Naik M, Vinuth M, Rami Reddy YV, Sujatha HR. Green synthesis of Lawsonia inermis-mediated zinc ferrite nanoparticles for magnetic studies and anticancer activity against breast cancer (MCF-7) cell lines. J Mater Sci Mater Electron. 2020;31(11):8589–96.
[213] Karthik K, Dhanuskodi S, Gobinath C, Prabukumar S, Sivaramakrishnan S. Fabrication of MgO nanostructures and its efficient photocatalytic, antibacterial and anticancer performance. J Photochem Photobiol B Biol. 2019;190:8–20.
[214] Kanagesan S, Hashim M, Aziz AB, Ismail S, Tamilselvan I, Alitheen SNB, et al. Evaluation of antioxidant and cytotoxicity activities of copper ferrite ($CuFe_2O_4$) and zinc ferrite ($ZnFe_2O_4$) nanoparticles synthesized by sol–gel self-combustion method. Appl Sci. 2016;6(9):184.
[215] Karthik K, Shashank M, Revathi V, Tatarchuk T. Facile microwave-assisted green synthesis of NiO nanoparticles from Andrographis paniculata leaf extract and evaluation of their photocatalytic and anticancer activities. Mol Cryst Liq Cryst. 2018;673(1):70–80.
[216] Foroughi F, Hassanzadeh-Tabrizi SA, Bigham A. In situ microemulsion synthesis of hydroxyapatite-$MgFe_2O_4$ nanocomposite as a magnetic drug delivery system. Mater Sci Eng C. 2016;68:774–9.
[217] John Ł, Janeta M, Szafert S. Designing of macroporous magnetic bioscaffold based on functionalized methacrylate network covered by hydroxyapatites and doped with nano-$MgFe_2O_4$ for potential cancer hyperthermia therapy. Mater Sci Eng C. 2017;78:901–11.
[218] Manohar A, Krishnamoorthi C. Photocatalytic study and superparamagnetic nature of Zn-doped $MgFe_2O_4$ colloidal size nanocrystals prepared by solvothermal reflux method. J Photochem Photobiol B Biol. 2017;173:456–65.
[219] Selvam R, Ramasamy S, Mohiyuddin S, Enoch IVMV, Gopinath P, Filimonov D. Molecular encapsulator–appended poly(vinyl alcohol) shroud on ferrite nanoparticles. Augmented cancer–drug loading and anticancer property. Mater Sci Eng C. 2018;93:125–33.
[220] Her S, Jaffray DA, Allen C. Gold nanoparticles for applications in cancer radiotherapy: Mechanisms and recent advancements. Adv Drug Deliv Rev. 2017;109:84–101.
[221] Meidanchi A, Motamed A. Preparation, characterization and *in vitro* evaluation of magnesium ferrite superparamagnetic nanoparticles as a novel radiosensitizer of breast cancer cells. Ceram Int. 2020;46(11, Part A):17577–83.
[222] Meidanchi A. $Mg(1–x)Cu_xFe_2O_4$ superparamagnetic nanoparticles as nano-radiosensitizer agents in radiotherapy of MCF-7 human breast cancer cells. Nanotechnology. 2020;31(32):325706.
[223] Ghobashy MM, Mohamed TM. Radiation preparation of conducting nanocomposite membrane based on (copper/polyacrylic acid/poly vinyl alcohol) for rapid colorimetric sensor of mercury and silver ions. J Inorg Organomet Polym Mater. 2018;28(6):2297–305.
[224] Abdel-Fattah AA, Soliman YS, Ghobashy MM. Synthesis and characterization of conjugated and nanostructured poly (propargyl alcohol) polymers. J Polym Res. 2018;25(4):1–13.
[225] Ghobashy MM, Abd Elkodous M, Shabaka SH, Younis SA, Alshangiti DM, Madani M, et al. An overview of methods for production and detection of silver nanoparticles, with emphasis on their fate and toxicological effects on human, soil, and aquatic environment. Nanotechnol Rev. 2021;10(1):954–77.